学位論文

Effects of Electron-Electron Interaction on Dirac Fermions in Solids

（固体中のディラック電子系における電子間相互作用の効果）

平成25年12月博士（理学）申請

東京大学大学院理学系研究科

物理学専攻

金尾 太郎

Abstract

In this thesis, two phenomena on electron-electron interaction in massless Dirac fermions and one related topic are theoretically investigated: the Kondo effect, charge fluctuations in the vicinity of a charge-ordered phase, and a localized state induced by a defect. The first has been experimentally observed in graphene, which is a representative of the Dirac fermion systems in solids. The second and third are related to experimentally observed anomalous behaviors in an organic conductor α-(BEDT-TTF)$_2$I$_3$ under pressure, where the massless Dirac fermions also exist at the Fermi energy. Both the first and third are caused by defects in the Dirac fermion systems.

In the first part, we propose a theory for the Kondo effect due to point defects in graphene. We develop an effective model for this Kondo effect, where the conduction electron states and the localized magnetic moment are formed by the π electrons extending over the sample and the dangling sp^2 orbitals around the defect, respectively. Finite hybridization between them is possible owning to a lattice distortion at the defect perpendicular to the graphene plane. By analyzing this model with the numerical renormalization group (NRG) method, it is shown that the experimentally observed gate-voltage dependence of the Kondo temperature can be understood in this framework. Then, a localized state of π electrons induced by the defect is taken into account. It is shown that this state assists the Kondo screening when the density of defects is finite. The behavior of this localized state in a magnetic field is studied by using a tight-binding model with Peierls phase. It is found that the orbital motion of the π electrons in the magnetic field modulates the localized state and causes the Kondo effect which is sensitive to the magnetic field.

In the second part, we investigate the localized state induced by a single defect in α-(BEDT-TTF)$_2$I$_3$ using a tight-binding model for this material. By diagonalizing the Hamiltonian with a single defect, it is demonstrated that the localized state is induced at the energy of Dirac points when the defect is at a certain sublattice (A or A', which correspond to A or B in graphene). This is also confirmed by using the Green's function method. This localized state enhances the local density of states in a finite region around the defect, and it shows an anisotropy. By using the Green's function method, the wave function of the localized state is evaluated in the $\boldsymbol{k}$ space. It is clarified that this state

consists of both the electron and hole states near the Dirac points, and shows anisotropy around it due to the tilting of the Dirac cones. The anisotropy of the localized state in the real space is understood from this tilting of the Dirac cones in the $\boldsymbol{k}$ space. The sublattice components of the localized state are also calculated in the $\boldsymbol{k}$ space. When the defect is located at the sublattice A, the largest contribution to the induced localized state is the sublattice A' component, and vice versa, which is similar to the case of graphene. Since this localized state consists of Dirac fermions, it can be used as an experimental tool for obtaining the information of the Dirac fermions such as the tilting of the Dirac cones, the position of the Dirac points in the Brillouin zone, and the sublattice components of the Dirac fermions. Possibility of its detection in scanning tunneling microscopy (STM) and NMR experiments is discussed.

In the third part, we investigate the effects of charge fluctuations in the vicinity of the charge-ordered phase in α-(BEDT-TTF)$_2$I$_3$, especially near the quantum critical point. First, from a minimal model which describes both the Dirac fermions and their charge ordering transition, a Landau-Ginzburg-Wilson functional is derived. This functional describes behaviors of the charge fluctuations in the Dirac fermion phase. Here, the Fermi energy is fixed at the energy of the Dirac points. We find that the charge fluctuations in Dirac fermions obey a characteristic dispersion which contains variables q and ω_l in a symmetric manner. Analyzing this functional with the perturbative renormalization group (PRG) method and the self-consistent renormalization (SCR) theory, which can take into account the coupling between several fluctuation modes, we show that the effects of the mode-mode coupling tend to be less effective in Dirac fermions compared with the case of conventional magnetic fluctuations in metals. Second, we investigate the effects of charge fluctuations on physical quantities by using the SCR theory. We show that the interaction between the electrons and the charge fluctuations causes peaks in the electron self-energy as a function of temperature and energy ω when the mode-mode coupling is strong. These peaks lead to an increase of the electron damping with decreasing temperature near the quantum critical point, which will cause an increase of resistivity as is observed in experiments. This characteristic behavior of the self-energy also causes a suppression of the density of states. Its relevance to the experimentally observed suppression of the spin susceptibility is discussed. The specific heat of the charge fluctuations is also calculated, and it is shown that the obtained temperature dependence in the case of a strong mode-mode coupling is compatible with experimental result.

Contents

Abstract **1**

1 Introduction **5**
- 1.1 Dirac Fermions in Solids 5
  - 1.1.1 Graphene 6
  - 1.1.2 Dirac Fermions in Organic Conductor α-(BEDT-TTF)$_2$I$_3$ 8
  - 1.1.3 Differences between Graphene and α-(BEDT-TTF)$_2$I$_3$ 10
- 1.2 Electron-Electron Interaction in Dirac Fermions 12
- 1.3 Outline of This Thesis 13

2 Kondo Effect in Graphene with Defects **15**
- 2.1 Introduction 16
  - 2.1.1 Kondo Effect in Ordinary Metals 16
  - 2.1.2 Kondo Effect in Graphene 17
  - 2.1.3 Magnetism in Graphene with Defects 20
  - 2.1.4 Localized State of π Electrons at the Defect 22
  - 2.1.5 Purposes of This Study 22
- 2.2 Localized Moment and its Hybridization with Conduction Electrons . . . 24
  - 2.2.1 Cluster Model for the Defect 24
  - 2.2.2 One-Dimensional Representation of the Conduction Electron States 29
- 2.3 Numerical Renormalization Group Method 30
- 2.4 Low-Energy States and the Kondo Temperature 33
- 2.5 Role of the Localized State of π Electrons at the Defect 38
- 2.6 Effects of Magnetic Field 39
- 2.7 Summary and Discussions 41
- Appendix of Chapter 2 Effect of Zeeman Field 43

3 Localized State in α-(BEDT-TTF)$_2$I$_3$ Induced by Single Defect **45**
- 3.1 Introduction 45
- 3.2 Tight-Binding Model with a Single Defect 48

3.3 Diagonalization of Hamiltonian with a Single Defect 50
3.4 Green's Function in the Presence of Single Defect 54
3.5 Discussions 60
3.6 Summary 61

4 Effects of Charge Fluctuations on Dirac Fermions in α-(BEDT-TTF)$_2$I$_3$ 63
4.1 Introduction 64
    4.1.1 Charge Ordering in α-(BEDT-TTF)$_2$I$_3$ 64
    4.1.2 Anomalous Properties of Dirac Fermion Phase 66
    4.1.3 Charge Fluctuations in the vicinity of Charge Ordering 66
4.2 Landau-Ginzburg-Wilson Functional for Dirac Fermions near Charge Ordering 68
    4.2.1 Minimal Model for Dirac Fermions near Charge Ordering 68
    4.2.2 Derivation of Landau-Ginzburg-Wilson Functional 68
4.3 Analysis of the Landau-Ginzburg-Wilson Functional 72
    4.3.1 Perturbative Renormalization Group Analysis 72
    4.3.2 Self-Consistent Renormalization Theory 74
4.4 Effects of Charge Fluctuations on Physical Quantities 76
    4.4.1 Solution of the Self-Consistent Equation 76
    4.4.2 Damping Rate of Electrons 78
    4.4.3 Specific Heat 81
    4.4.4 Self-Energy and Density of States 83
4.5 Summary and Discussions 87

5 Summary and Outlook 89
5.1 Summary 89
5.2 Outlook 91

Acknowledgements 93

References 95

Chapter 1

Introduction

In this chapter, Dirac fermions in solids and effects of electron-electron interaction on the Dirac fermions are reviewed. After introducing Dirac fermions in solids in general, those in graphene and in an organic conductor α-(BEDT-TTF)$_2$I$_3$ are described. Differences between them are discussed. Then, recent progresses of studies on electron-electron interaction in Dirac fermions in solids, especially in graphene, are briefly reviewed. At the end of this chapter, the outline of this thesis is summarized.

1.1 Dirac Fermions in Solids

In a solid, which is a regular array of atoms, every electronic state can be labeled by a wave vector $\boldsymbol{k}$ owning to the translational symmetry [1]. In the one-electron model, where effects of correlation between the electrons due to the Coulomb interaction are ignored, the electronic energy levels are divided into bands $\epsilon_{\boldsymbol{k}n}$, where n is a band index. In accordance with the Pauli principle, the ground state of the electron system is obtained by filling the energy levels by electrons from the lowest to the Fermi energy ϵ_F, which is determined by the number of electrons in the solid. The band structure $\epsilon_{\boldsymbol{k}n}$ in the vicinity of ϵ_F (or within the range of temperature T measured from ϵ_F) determines many of the properties of solids and the classification between insulators, semiconductors, and metals.

When $\epsilon_{\boldsymbol{k}n}$ near ϵ_F has a form

$$\epsilon_{\boldsymbol{k}\pm} = \pm\sqrt{E_0^2 + v^2 \left|\boldsymbol{k} - \boldsymbol{k}_0\right|^2}, \tag{1.1}$$

in the vicinity of $\boldsymbol{k} = \boldsymbol{k}_0$, then the system is called "Dirac fermions (or electrons) in solid", because this energy dispersion is the same as that of relativistic quantum theory of electrons by Dirac [2]. The point $\boldsymbol{k} = \boldsymbol{k}_0$ is called the Dirac point. Although the original Dirac electrons are isotropic in $\boldsymbol{k}$ space, several anisotropic cases realized in solids are also called Dirac fermions. Dirac fermions in solids have been discussed in

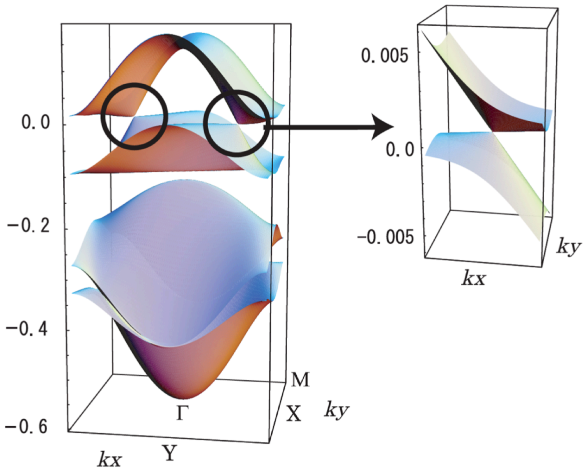

Figure 1.1: Band dispersion of α-(BEDT-TTF)$_2$I$_3$ near the Fermi energy, calculated based on the semi-empirical tight-binding model [5]. The Fermi energy is taken to be zero. [Reprinted figure with permission from S. Katayama, A. Kobayashi, and Y. Suzumura, J. Phys. Soc. Jpn. **75** (2006) 054705. Copyright (2006) by the Physical Society of Japan.]

graphene [3], bismuth [4], an organic conductor α-(BEDT-TTF)$_2$I$_3$ [5], iron-pnictide superconductors [6, 7], and topological insulators [8]. They are established as Dirac fermions both by experimental and theoretical studies. Also, there are some proposed candidates of Dirac fermion systems, such as an inverse perovskite material Ca$_3$PbO [9].

The main focus of this thesis is graphene and α-(BEDT-TTF)$_2$I$_3$. Although the real electron has a finite rest mass $E_0 = m$, the situation $E_0 = 0$, which is called massless Dirac fermion or Weyl fermion, is realized in these materials. The band dispersion of α-(BEDT-TTF)$_2$I$_3$ near the Fermi energy is shown in Fig. 1.1 [5], where the Fermi energy is taken to be zero. In this material, the Fermi energy coincides with the Dirac points. This Dirac dispersion has anisotropy, which is called a tilted Dirac cone.

1.1.1 Graphene

Graphene is a single layer of carbon atoms aligned in the honeycomb lattice [10, 11]. Its band structure had been studied theoretically from 1940s, and the existence of Dirac fermions had been predicted [3]. After the report of its isolation together with the characteristic transport properties in 2004 [12] and the subsequent observations of the quantum Hall effect [13, 14], graphene has been studied extensively both from the basic scientific interests and from its expected industrial applications.

An isolated carbon atom has four electrons in $2s$ and $2p$ orbitals. In graphene, three electrons among them are contained in the sp^2 orbitals which are made of $2s$, $2p_x$, and

$2p_y$ orbitals. These sp^2 orbitals form robust bonds between carbon atoms. The resulting σ band is located several eV below the Fermi energy [15, 16]. The remaining one electron is contained in the $2p_z$ orbital and forms the π band, which is located near the Fermi energy.

The π band is well reproduced by the tight-binding model with the nearest-neighbor transfer integral between $2p_z$ orbitals [10]. This model is simple, but it contains essential features of Dirac fermion systems in two dimensions and plays important roles in this thesis. Here, we describe the properties of this model.

Since the honeycomb lattice consists of two triangular sublattices denoted by the sublattice A and B, the tight-binding Hamiltonian is expressed in terms of two corresponding fermionic operators $a_{i\sigma}$ and $b_{j\sigma}$:

$$H = -t \sum_{<ij>,\sigma=\uparrow\downarrow} \left(a^\dagger_{i\sigma} b_{j\sigma} + b^\dagger_{j\sigma} a_{i\sigma} \right) - \mu N, \tag{1.2}$$

where $t(>0)$, μ, and N are the nearest-neighbor transfer integral, the chemical potential, and the total number of electrons on the $2p_z$ orbitals, respectively. The position of an electron and its spin are denoted by i, j and $\sigma = \uparrow\downarrow$. In the $\boldsymbol{k}$ representation, the Hamiltonian is expressed in the 2×2 matrix for each $\boldsymbol{k}$ and σ. Then, the Hamiltonian is diagonalized as

$$\begin{aligned} H &= \sum_{\boldsymbol{k}\sigma} \left(a^\dagger_{\boldsymbol{k}\sigma}\ b^\dagger_{\boldsymbol{k}\sigma} \right) \begin{pmatrix} -\mu & \phi_{\boldsymbol{k}} \\ \phi^*_{\boldsymbol{k}} & -\mu \end{pmatrix} \begin{pmatrix} a_{\boldsymbol{k}\sigma} \\ b_{\boldsymbol{k}\sigma} \end{pmatrix} && (1.3) \\ &= \sum_{\boldsymbol{k}\sigma, n=\pm} \left(n \left| \phi_{\boldsymbol{k}} \right| - \mu \right) c^\dagger_{\boldsymbol{k}\sigma n} c_{\boldsymbol{k}\sigma n}, && (1.4) \end{aligned}$$

where $\phi_{\boldsymbol{k}} = -t \sum_{\boldsymbol{\delta}} \mathrm{e}^{\mathrm{i}\boldsymbol{k}\cdot\boldsymbol{\delta}}$, and $\boldsymbol{\delta}$ is the vector connecting the nearest-neighbor carbon sites. The dispersion $\epsilon_{\boldsymbol{k}\pm} = \pm \left| \phi_{\boldsymbol{k}} \right|$ becomes zero at two particular points in $\boldsymbol{k}$ space called $\boldsymbol{K}$ and $\boldsymbol{K}'$ point. Around these points, the dispersions are linear in $\boldsymbol{k}$, i.e. $\epsilon_{\boldsymbol{K}+\boldsymbol{k}\pm} = \pm vk$ in the lowest order of k, with v being the Fermi velocity. This means that Dirac fermions are realized in graphene, and the two points $\boldsymbol{K}$ and $\boldsymbol{K}'$ are the Dirac points.

The fermionic operators in the band representation $c_{\boldsymbol{k}\sigma n}$ are related to those in the sublattice representation as

$$\begin{pmatrix} a_{\boldsymbol{k}\sigma} \\ b_{\boldsymbol{k}\sigma} \end{pmatrix} = \frac{1}{\sqrt{2}} \begin{pmatrix} 1 & 1 \\ \mathrm{e}^{-\mathrm{i}\arg\phi_{\boldsymbol{k}}} & -\mathrm{e}^{-\mathrm{i}\arg\phi_{\boldsymbol{k}}} \end{pmatrix} \begin{pmatrix} c_{\boldsymbol{k}\sigma +} \\ c_{\boldsymbol{k}\sigma -} \end{pmatrix}. \tag{1.5}$$

This matrix corresponds to the wave function of the state. A characteristic feature of this wave function is that it has phase factors and it varies strongly in the vicinity of the zero of $\phi_{\boldsymbol{k}}$, i.e. the Dirac point. These phase factors cause absence of backward scattering [17], and are related to antilocalization [18]. Antilocalization means that a system should be

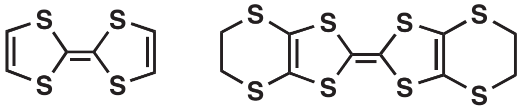

(a) TTF (b) BEDT-TTF

Figure 1.2: Molecular structures of TTF and BEDT-TTF [21].

metallic in the ground state, and its resistivity decreases as temperature goes down. Such behaviors have been observed experimentally under certain conditions [18].

In grapehene, the chemical potential μ can be tuned by applying a gate voltage in a certain range. The corresponding range of the density of electrons is as wide as from -10^{13} cm^{-2} (holes) to 10^{13} cm^{-2} (electrons) [18]. The gate voltage where the carrier density is smallest is called a charge neutrality point. When the gate voltage is at the charge neutrality point, the chemical potential coincide with the energy of the Dirac points.

1.1.2 Dirac Fermions in Organic Conductor α-(BEDT-TTF)$_2$I$_3$

Here, the history of studies on organic conductors (BEDT-TTF)$_2$X and that on α-(BEDT-TTF)$_2$I$_3$ are briefly reviewed.

Organic solids are usually insulators [19, 20, 21, 22]. This is because the electronic states of constituent organic molecules usually have closed-shell structures and there is large energy separation between the highest occupied molecular orbital (HOMO) and the lowest unoccupied one (LUMO). When the molecules cohere, this electronic structure of individual molecules results in filled bands and a large energy gap above the Fermi energy. In order to make them conductive, charge transfer from organic molecules is necessary, which is realized by the combination of electronic donors and accepters.

Suitable organic molecules for such charge transfer are molecules with π electrons, which are easily charged and stable in the charged states. Based on this idea, several organic conductors were synthesized in 1970s, such as TTF·TCNQ where TTF (tetrathiafulvalene) and TCNQ (tetracyanoquinodimethane) are a donor and an accepter, respectively [23]. The molecular structure of TTF is shown in Fig. 1.2(a). One of the characteristic feature of these early-days organic conductors is its quasi-one dimensional electronic states. This is because molecules with π electrons are usually planer, and they stack in columns in solid. On these organic conductors, physics of one-dimensional system was investigated. However, they show instabilities into insulating states intrinsic to one-dimensional systems and the increase of dimensionality was needed to realize good conductors.

A two-dimensional organic conductor was found in the family of (BEDT-TTF)$_2$X in

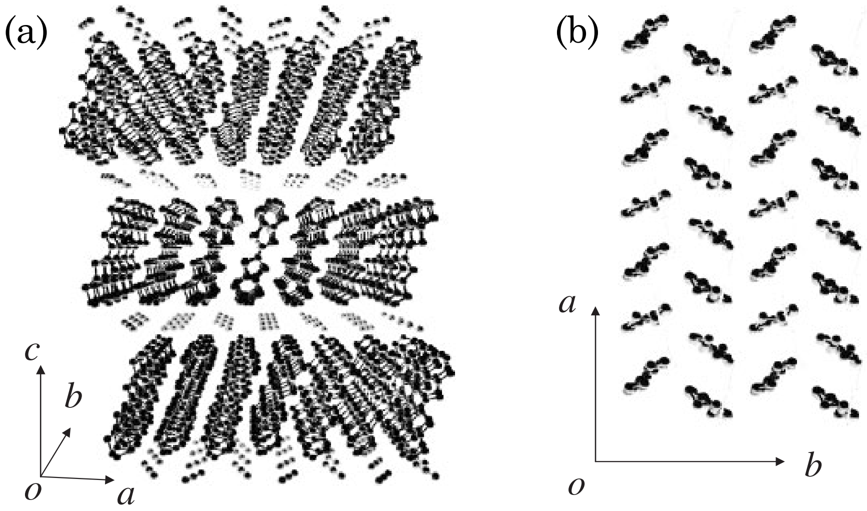

Figure 1.3: Crystal structure of α-(BEDT-TTF)$_2$I$_3$ [36]. (a) Viewed from b-axis. (b) Arrangement of BEDT-TTF molecules in the conducting layer. The axis a is parallel to the direction of the stacking column of ET molecules. [Reprinted figure with permission from N. Tajima *et al.*, J. Phys. Soc. Jpn. **75** (2006) 051010. Copyright (2006) by the Physical Society of Japan.]

1982 [24]. BEDT-TTF (bis(ethylenedithio)tetrathiafulvalene, or simply ET) is an electric donor and X is an accepter. The ET molecule was first synthesized in 1978 [25], and has the structure where two outer ethylenedithio-ring are attached to TTF molecule as shown in Fig. 1.2(b). In the solid of (ET)$_2$X, the ET molecules and the X form layers respectively (Fig. 1.3). One electron per two ET molecules is transferred into an X, resulting in a 3/4-filled electron system in the ET layers and an insulating X layers due to the closed-shell electronic structure of X$^-$.

Owning to the outer rings, the ET molecule takes slightly nonplanar conformations in solids [19, 22]. This reduces the overlap of the π orbitals within a column, while the overlaps between columns become appreciable. This leads to a two-dimensional electronic structure rather than one-dimensional one. The nonplanar conformations of ET molecule cause a variety of arrangements in solid, which are classified as α, β, θ and so on. Conductors based on the ET molecule have been studied extensively, and it has been revealed that they exhibit a variety of interesting phenomena such as superconductivity, magnetism, and charge ordering.

α-(ET)$_2$I$_3$ was first synthesized in 1984 [26]. The crystal structure is shown in Fig. 1.3. The accepter is I$_3$ molecule. It was reported that the solid behaves like a two-dimensional metal in the temperature range between 135 and 300 K, while below 135 K a metal-insulator transition occurs. This metal-insulator transition was revealed to be a charge ordering transition in 2000s [27, 28]. The studies of this charge ordering are reviewed in

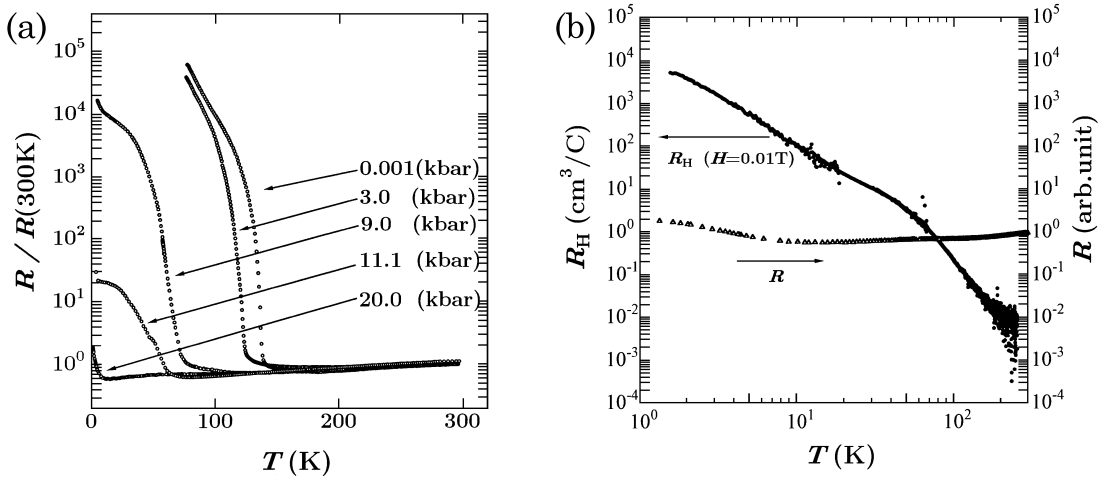

Figure 1.4: Transport properties of α-(BEDT-TTF)$_2$I$_3$ under pressure [32]. (a) Temperature dependence of the resistivity under several pressures. (b) Temperature dependence of the Hall coefficient and the resistivity. [Reprinted figure with permission from N. Tajima *et al.*, J. Phys. Soc. Jpn. **69** (2000) 543. Copyright (2000) by the Physical Society of Japan.]

chapter 4. This metal-insulator transition is suppressed by hydrostatic pressures, and in high pressures, almost temperature independent resistivity was found [29, 30] as shown in Fig. 1.4(a). Transport properties of this high pressure metallic phase were examined in magnetic field, and it was discovered that the Hall coefficient strongly depends on the temperature, and the mobility of carriers at low temperature is extremely high [31, 32] [Fig. 1.4(b)]. This behavior had been considered as a consequence of band structure of a semimetal or a narrow gap semiconductor.

In 2006, the band structure was investigated by using tight-binding model which is obtained from the X-ray diffraction experiment [33], and the existence of Dirac fermions was revealed [5], which is shown in Fig. 1.1. The energy of the Dirac points coincides with the Fermi energy owning to the filling 3/4. This result was also supported by density functional theory calculations [34, 35]. After this discovery, the high pressure phase of this solid has been actively investigated. In addition to the transport measurements [36], magnetic [37, 38, 39] and thermal [40, 41, 42] measurements have been reported. By these experiments, the Dirac fermions in α-(ET)$_2$I$_3$ have been established.

1.1.3 Differences between Graphene and α-(BEDT-TTF)$_2$I$_3$

Here, the major differences between graphene and α-(ET)$_2$I$_3$ are enumerated.

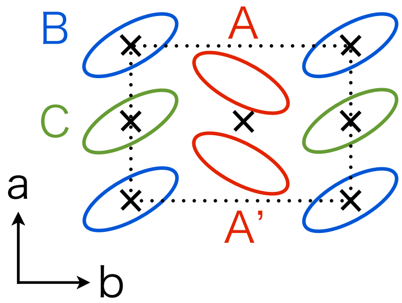

Figure 1.5: Arrangement of ET molecules in a conducting plane of α-(BEDT-TTF)$_2$I$_3$ [43]. The dotted rectangle represents a unit cell. There are four ET molecules in the unit cell, which are denoted by A, A', B, and C. In the Dirac fermion phase, A and A' are crystallographically equivalent. The X's represent inversion centers. They are located in the middle of A and A', on B, and C.

1. **Lattice structure**
   While graphene has a highly symmetrical honeycomb structure, α-(ET)$_2$I$_3$ has a structure with lower symmetry. Figure 1.5 shows the molecular arrangement of α-(ET)$_2$I$_3$ within a unit cell [43]. There are four ET molecules called A, A', B, and C. Without the charge ordering, the A and A' are equivalent: there is a inversion center between them and they are related by the inversion symmetry. The B and C are also on inversion centers respectively. The A and A' form a stacking column, and the B and C form another. Within the tight-binding model, it is known that the Dirac dispersion is gapped if the inversion symmetry is broken by putting some on-site potential on the A or A'. This behavior is similar to that of graphene, where the Dirac dispersion is gapped when the symmetry between sublattices A and B is broken. This implies that the molecular site A and A' in α-(ET)$_2$I$_3$ play the similar role in forming the Dirac dispersion to the sublattice A and B in graphene.

2. **Position of the Dirac points in the Brillouin zone**
   As is anticipated from its highly symmetrical lattice structure, the Dirac points in graphene are located at high symmetry points in the Brillouin zone. On the other hand, the Dirac points in α-(ET)$_2$I$_3$ are located at general points [5]. In both cases, there are two Dirac points in the Brillouin zone, and they are related to each other by the space inversion, which reflects the inversion symmetry of their lattices.

3. **Shape of the Dirac cones**
   While the Dirac cones in graphene are isotropic, those in α-(ET)$_2$I$_3$ are tilted [5]. Experimentally, this tilting has been detected by NMR through site-selective mea-

surements [39]. However, it has not been measured directly.

4. **Surface or bulk**
   Graphene is fabricated on a surface of a substrate, while α-(ET)$_2$I$_3$ is a layered bulk material. A surface is controllable electrically, and in graphene, the density of electrons is controlled readily by applying a gate voltage, which is difficult in the bulk α-(ET)$_2$I$_3$ [44]. On the surface, however, effects of randomness is inevitable such as surface roughness of the substrate and absorbed molecules. Such randomness must be taken into account to understand the properties of graphene. On the other hand, the effect of randomness in α-(ET)$_2$I$_3$ is considered to be very small. Another consequence of the bulk layered structure of α-(ET)$_2$I$_3$ is that measurements of thermal and magnetic quantities are possible, where a bulk of solid is needed to obtain sufficient signals.

5. **Constituent units**
   The constituent units of graphene are the carbon atoms, which form robust covalent bonds. On the other hand, those of α-(ET)$_2$I$_3$ are the ET molecules. Compared with the case of atoms, the bonding between molecules is weak, and it causes small transfer integrals among the HOMOs forming the band around the Fermi energy. Because of this small transfer integrals, other energy scales such as external fields and electron-electron interaction become relatively large. In fact, long-range electron-electron interaction causes charge ordering as mentioned above. Another property caused by the weak bonding between molecules is the controllability of electronic states under a pressure. By the pressure, the transfer integrals increase, and other energy scales become relatively small. This causes rich phase diagrams of molecular conductors in the temperature-pressure plane.

1.2 Electron-Electron Interaction in Dirac Fermions

In the one-electron model introduced in §1.1, electron-electron interaction is ignored. However, it is known that the interaction is strong and long range. In ordinary metals, the validity of the one-electron model has been established on the basis of the theory of screening of electric field, and the Landau theory of Fermi liquid [45].

These issues have been investigated in Dirac fermions in solids, in particular, in graphene [46]. It has been shown that the long-range interaction is not screened in the ordinary way when the Fermi energy coincides with the Dirac point. This unscreened long-range interaction leads to characteristic behaviors near the Dirac point, which is distinguished from the ordinary Fermi liquid. One of such behaviors is a logarithmic increase of Fermi velocity near the Dirac point, which has been observed experimentally [47] (Fig. 1.6).

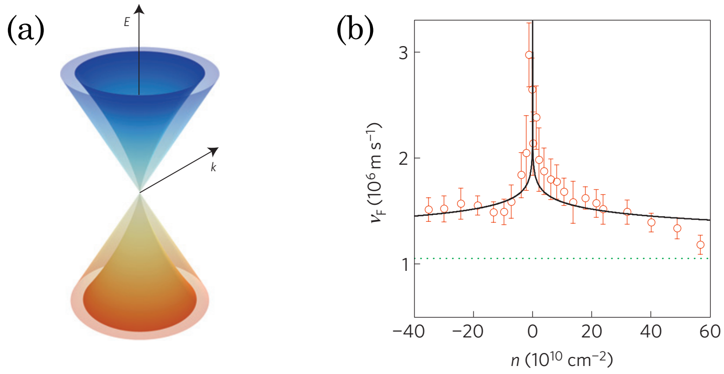

Figure 1.6: (a) Reshaping of Dirac dispersion due to long-range electron-electron interaction [47]. (b) Density dependence of Fermi velocity for suspended graphene [47]. [Reprinted figure with permission from D. C. Elias *et al.*, Nat. Phys. **7** (2011) 701. Copyright (2011) by Nature Publishing Group.]

In Dirac fermion systems, ordered states caused by electron-electron interaction have been studied theoretically, where the one-electron picture is drastically changed from the non-interacting case [46]. Charge and magnetic orders and superconductivity have been discussed in graphene.

Another situation where the electron-electron interaction plays a major role is a magnetic impurity in a metal [48, 49]. In ordinary metals, the localized magnetic moment caused by strong electron correlation in the impurity atom is screened by conduction electrons at low temperatures. This is the Kondo effect. It is known that the ground state is connected continuously to the non-interacting ground state as in the Landau theory of Fermi liquid. This problem has also been studied in Dirac fermion systems. When the Fermi energy is at the Dirac point, the screening of the localized magnetic moment depends on the strength of the coupling between the localized magnetic moment and the conduction electrons [46]. At the border of the two regions in the phase diagram, there is a quantum critical point, which does not exist in ordinary metals.

1.3 Outline of This Thesis

As reviewed above, the discovery of new class of solids, Dirac fermion systems, has stimulated theoretical studies on effects of electron-electron interaction in these systems. By the rapid and intensive research, understanding of some basic aspects has now been obtained. The next step of the research is to understand real and concrete phenomena on the electron-electron interaction experimentally found in the individual Dirac fermion systems. Such efforts will extend the frontier of the research field and enrich the physics of Dirac fermions in solids.

In this thesis, effects of electron-electron interaction on Dirac fermions in solids are studied theoretically in relation to experimental facts on graphene and α-(ET)$_2$I$_3$. In chapter 2, local electron correlation, or the Kondo effect, is studied in graphene with defects. In chapter 4, effects of electron-electron interaction in the bulk are studied in the Dirac fermion phase of α-(ET)$_2$I$_3$. This phase is located next to charge-ordered phase, which means that the long-range electron-electron interaction is strong in this material. As a topic related to both chapter 2 and 4, electronic states near single defect in the Dirac fermion phase of α-(ET)$_2$I$_3$ are studied in chapter 3. Although electron-electron interaction is ignored in this chapter, the realistic lattice and band structures of α-(ET)$_2$I$_3$ are taken into account. The thesis is summarized in chapter 5.

Chapter 2

Kondo Effect in Graphene with Defects

In this chapter, the Kondo effect due to point defects in graphene is studied. After a brief review of the Kondo effect in ordinary metals and the experimentally observed Kondo effect in graphene (§2.1), an effective model for this Kondo effect is developed in §2.2.1, where the electronic state and the lattice structure of the defect are examined. In this model, the π orbitals form the conduction electron states, and the dangling sp^2 orbitals around the defect form the localized magnetic moment. In §2.2.2, the conduction electron states which are coupled with the dangling sp^2 orbital are clarified by transforming the effective model into a one-dimensional representation. This model is analyzed by the Wilson's numerical renormalization group (NRG) method, which is introduced in §2.3. In §2.4, it is shown that the experimentally observed gate-voltage dependence of the Kondo temperature can be understood in this framework when the density of defects is low. In §2.5, localized states of π electrons which are induced by the defects are taken into account, and it is shown that these states assist the Kondo screening when the density of defects is finite. In §2.6, the behavior of this localized state in a magnetic field is studied by using a tight-binding model with Peierls phase. It is found that the orbital motion of the π electrons in the magnetic field modulates the localized state and causes the Kondo effect which is sensitive to the magnetic field. In §2.7, the results are summarized and its relevance to the experimental results are discussed.

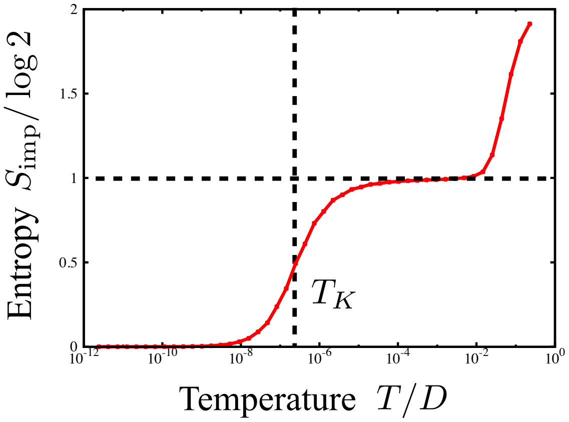

Figure 2.1: Temperature dependence of the impurity contribution of entropy S_{imp} in an ordinary metal calculated by the numerical renormalization group (NRG) method. Here, the spin of the impurity is 1/2. The Boltzmann constant is $k_B = 1$, and the temperature is normalized by a cut-off energy D. The vertical and horizontal dotted lines represent $T = T_K$ and $S_{\mathrm{imp}} = \log 2$, respectively.

2.1 Introduction

2.1.1 Kondo Effect in Ordinary Metals

In ordinary metals, a localized magnetic moment on an impurity is screened by the conduction electrons at low temperatures [48]. Figure 2.1 shows temperature dependence of the impurity contribution of entropy S_{imp} calculated by the Wilson's numerical renormalization group (NRG) method [50]. Here, the spin of the impurity is 1/2, and the temperature is normalized by a cut-off energy D. In this thesis, the Boltzmann constant is $k_B = 1$. As the temperature is lowered, a crossover from the state with $S_{\mathrm{imp}} = \log 2$ to that with $S_{\mathrm{imp}} = 0$ occurs around a temperature T_K. This corresponds to the crossover from the unscreened localized moment state to the screened state or the Kondo-Yosida singlet state. This crossover accompanies anomalies in resistivity and thermodynamic quantities such as specific heat and spin susceptibility when the density of the impurities is finite. These phenomena associated with this crossover and its characteristic temperature T_K are called the Kondo effect and the Kondo temperature, respectively. Especially, the representative of the Kondo effect is the temperature dependence of the resistivity, which shows a logarithmic increase around T_K [51] and saturates as $\sim T^2$ at low temperatures.

A simple model which describes a magnetic impurity in a metal is the Anderson model, which is given by

$$H = H_0 + H_{\mathrm{imp}} + H_{\mathrm{hyb}}, \tag{2.1}$$

$$H_0 = \sum_{k\sigma=\uparrow\downarrow} \epsilon_k c^\dagger_{k\sigma} c_{k\sigma}, \tag{2.2}$$

$$H_{\mathrm{imp}} = \sum_\sigma \epsilon_d d^\dagger_\sigma d_\sigma + U d^\dagger_\uparrow d_\uparrow d^\dagger_\downarrow d_\downarrow, \tag{2.3}$$

$$H_{\mathrm{hyb}} = \sum_\sigma V c^\dagger_{i=0\sigma} d_\sigma + \mathrm{h.c.}. \tag{2.4}$$

Here, H_0 is the Hamiltonian of the conduction electrons, where ϵ_k are energy eigenvalues of states k, and $c^\dagger_{k\sigma}$ and $c_{k\sigma}$ are the corresponding creation and annihilation operators with spin $\sigma =\uparrow\downarrow$. H_{imp} is that of the impurity, where ϵ_d is an energy level of the impurity atom, and $d^\dagger_\sigma$ and d_σ are the corresponding creation and annihilation operators. U is a Coulomb interaction in the impurity. H_{hyb} represents the hybridization between the conduction electrons and the impurity, where V is its strength, and $c^\dagger_{i=0\sigma}$ is the creation operator of conduction electrons on the impurity site.

On this model, whether the Kondo effect occurs or not depends on the parameters ϵ_d, U, and V. When V is zero, the Hamiltonian is readily solved, and the impurity has a localized moment if $\epsilon_d < 0$ and $U > |\epsilon_d|$. When V is finite, on the other hand, the problem becomes a many-body problem, where all the degrees of freedom are coupled with each other through the impurity, which is called the Kondo problem. For this problem, methods such as the numerical renormalization group method [50] have been developed, and it has been revealed that the crossover from the localized moment state to the Kondo-Yosida singlet state occurs if V is finite. Although the qualitative picture has long been obtained by this model, a realistic estimation of these parameters has appeared only recently for iron impurities in gold and silver [52], where density functional theory (DFT) calculations are used.

2.1.2 Kondo Effect in Graphene

After the fabrication of graphene, the Kondo effect in graphene has attracted much theoretical attention, because exotic Kondo effects and associated phenomena due to its Dirac conduction electrons are expected [53], such as multichannel Kondo effects, gate-tunable Kondo effects, and an impurity quantum phase transition between an unscreened and a screened localized moment state [46, 54, 55, 56, 57].

As candidates of the realization of the Kondo effect in graphene, the graphene with magnetic impurities such as Fe or Co has been investigated by DFT calculations [53]. The possibility of the Kondo effect in these systems has been argued by examining the lattice positions, the spin state of the impurity atom, and the strength and symmetry of

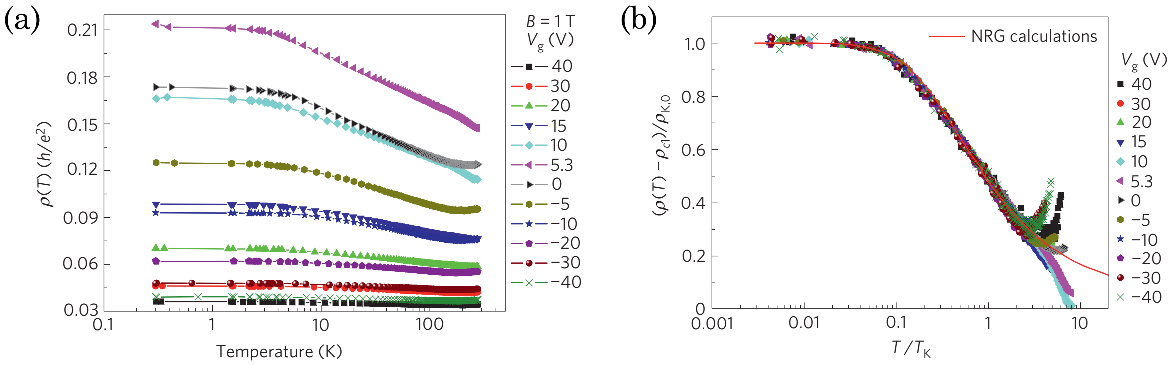

Figure 2.2: (a) Temperature dependence of resistivity of graphene with defects in the magnetic field $B = 1$ T for several gate voltages [59]. (b) Normalized Kondo part of the resistivity plotted against T/T_K. The red line is the universal Kondo behavior calculated by using the numerical renormalization group method. [Reprinted figure with permission from J.-H. Chen *et al.*, Nat. Phys. **7** (2011) 535. Copyright (2011) by Nature Publishing Group.]

the hybridization between the impurity and the conduction electrons. Experiments on graphene with such magnetic impurities have been attempted, and spectral signatures of the Kondo screening have been observed in scanning tunneling microscope (STM) experiments [58]. In such systems, however, Kondo effect had not been observed in resistivity measurements.

In 2011, the Kondo effect was reported in the resistivity of graphene with defects as shown in Fig. 2.2 [59]. The defects were introduced by the irradiation of He^+ ions with the energy of 500 eV. Figure 2.2(a) shows the temperature dependence for several gate voltages. As the temperature is lowered, the resistivity first increases logarithmically, and then saturates at low temperatures. In Fig. 2.2(b), the temperature dependent part of the resistivity (which is normalized) is plotted against the temperature divided by a scale T_K. It was found that this part of the resistivity for different gate voltages falls into a single line by choosing T_K appropriately for each gate voltage. The line can be fitted well by the universal temperature dependence of the Kondo effect as shown is Fig. 2.2(b). The gate-voltage dependence of T_K for two samples are shown in Fig. 2.3. They show minima around the charge neutrality point.

Figure 2.4 shows the magnetoresistance of the same sample at the temperature $T =$ 300 mK for several gate voltages [59]. Magnetic field is applied perpendicular to the graphene plane. The negative magnetoresistance at small magnetic fields originates from the weak localization. The contribution of the weak localization is suppressed by the magnetic field $B \sim 1$ T, and a magnetoresistance due to another mechanism occurs at higher magnetic fields. In the case of the Kondo effect, the Zeeman effect of magnetic

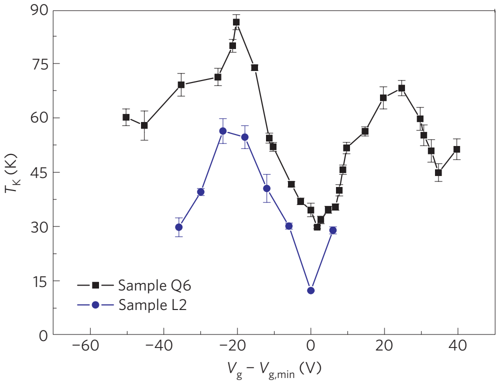

Figure 2.3: Gate-voltage dependence of Kondo temperature T_K for two samples of graphene with defects [59]. The charge neutrality point is at $V_g - V_{g,\text{min}} = 0$. [Reprinted figure with permission from J.-H. Chen *et al.*, Nat. Phys. **7** (2011) 535. Copyright (2011) by Nature Publishing Group.]

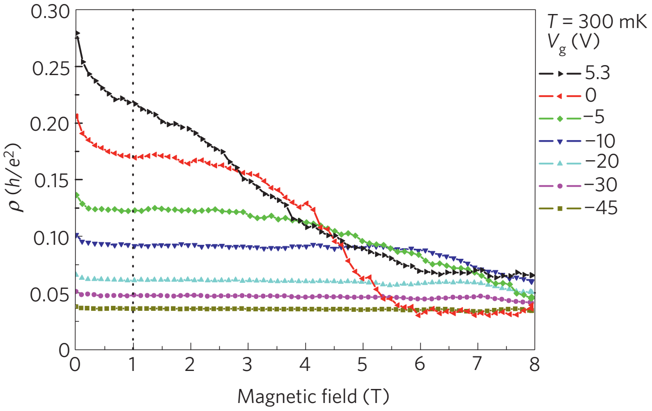

Figure 2.4: Magnetoresistance of graphene with defects for several gate voltages at the temperature $T = 300$ mK [59]. [Reprinted figure with permission from J.-H. Chen *et al.*, Nat. Phys. **7** (2011) 535. Copyright (2011) by Nature Publishing Group.]

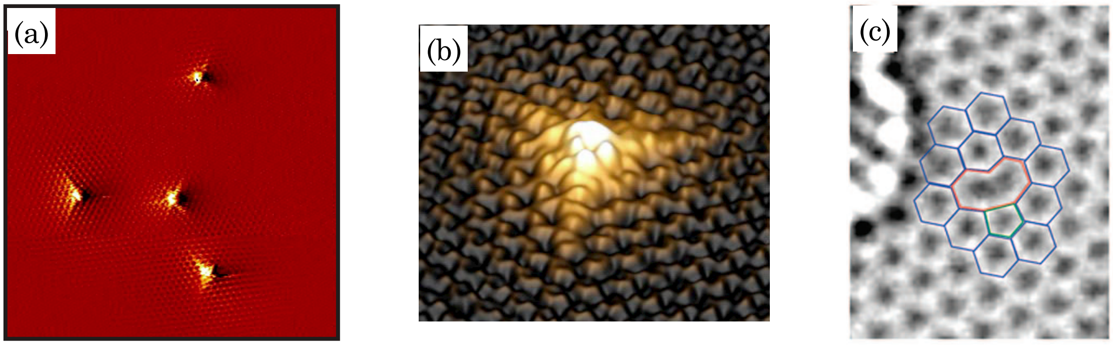

Figure 2.5: (a) Scanning tunneling microscopy (STM) image of the graphite surface irradiated with Ar^+ ions [63]. (b) Three-dimensional view of a single isolated defect [63]. [Reprinted figure with permission from M. M. Ugeda *et al.*, Phys. Rev. Lett. **104** (2010) 096804. Copyright (2010) by the American Physical Society.] (c) Transmission electron microscopy (TEM) image of a reconstructed defect in graphene [65]. [Reprinted figure with permission from J. C. Meyer *et al.*, Nano Lett. **8** (2008) 3582. Copyright (2008) by the American Chemical Society.]

field can cause such a negative magnetoresistance. From these observations, the Kondo effect due to magnetic origin was concluded in this system.

2.1.3 Magnetism in Graphene with Defects

Actually, the defects in graphene or graphite have been studied as a source of magnetism [60]. In graphite, it has been observed that magnetic moments are induced by irradiation of high-energy (2.25 MeV) protons [61]. In the graphene irradiated with ions, the magnetic moments have also been observed [62]. It has been indicated that the defect individually behaves as a localized magnetic moment.

Such defects have been studied in STM experiments [63, 64]. Figures 2.5(a) and (b) show the STM images of the graphite surface irradiated with Ar^+ ions [63]. These figures show that the introduced defects are point defects (or point vacancies). The defects in graphene have also been investigated with transmission electron microscopes (TEMs) [65]. Figure 2.5(c) shows the TEM image of a defect in graphene. Here, reconstruction and deformation of the defect are observed.

Such a point defect in graphene has been studied with the DFT calculations. First, the lattice structure was investigated [66]. Two possible structures were considered, which are shown in Figs. 2.6(a) and (b): one is a threefold symmetric structure that preserves the original symmetry, and the other is a twofold symmetric structure in which one of the C-C distances is shortened. It was clarified that the latter is more stable owning to the Jahn-Teller effect, and it has an out-of-plane displacement as shown in Fig. 2.6(c),

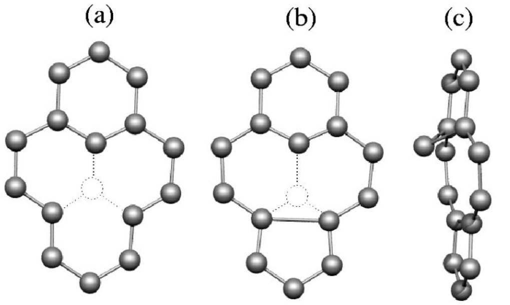

Figure 2.6: Optimized lattice structures of a point defect in graphene obtained by the density functional theory calculations [66]. (a) Threefold symmetric structure. (b) Twofold symmetric structure. (c) Side view of the twofold symmetric structure. [Reprinted figure with permission from A. A. El-Barbary *et al.*, Phys. Rev. B **68** (2003) 144107. Copyright (2003) by the American Physical Society.]

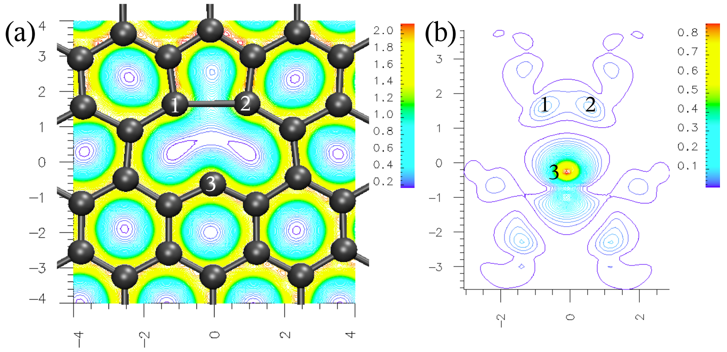

Figure 2.7: (a) Structure, charge density, and (b) spin density of a point defect in graphene obtained by spin-polarized density functional theory calculations [67]. [Reprinted figure with permission from P. O. Lehtinen *et al.*, Phys. Rev. Lett. **93** (2004) 187202. Copyright (2004) by the American Physical Society.]

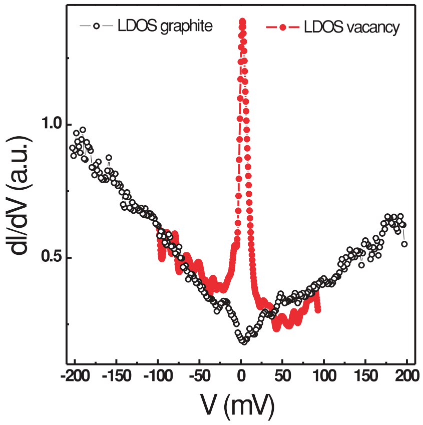

Figure 2.8: Local density of states of graphite measured with scanning tunneling spectroscopy (STS) [63]. The black open circles show that of pristine graphite and the red solid circles show that on top of the point defect. [Reprinted figure with permission from M. M. Ugeda *et al.*, Phys. Rev. Lett. **104** (2010) 096804. Copyright (2010) by the American Physical Society.]

while the former has a planar structure. Second, the spin state was investigated by using spin-polarized DFT calculations [67, 68]. It was shown that the defect is magnetic and the dangling sp^2 bond which appears at the defect is responsible for the magnetic moment as shown in Fig. 2.7(b).

2.1.4 Localized State of π Electrons at the Defect

In graphene, effects of defect scattering on the π electrons have been studied theoretically, and it has been suggested that the point defect induces a localized state of π electrons around the defect whose energy eigenvalue coincides with the energy of the Dirac points [69, 70, 71, 72]. Such a localized state has been observed experimentally with the STM as a bright spot shown in Figs. 2.5(a) and (b) [63, 64]. In scanning tunneling spectroscopy (STS) experiments, the localized state exhibits a sharp peak in local density of states (LDOS) near the defect, as shown in Fig 2.8 [63].

2.1.5 Purposes of This Study

Although the Kondo effect in graphene with defects seems to be due to the localized magnetic moments on the sp^2 orbital at the defects, there are several unclear points in this Kondo effect as listed below.

1. **Hybridization between the sp^2 orbital and the π conduction states**
   A hybridization between localized magnetic moments and conduction electrons are

necessary for a Kondo effect. However, in the planer graphene, there is no hybridization between the sp^2 orbital and the π conduction states, since they are orthogonal. To understand the finite hybridization, detailed consideration on the electronic and lattice structure of the defect is needed.

2. **Gate-voltage dependence of the Kondo temperature**
   Experimentally, the Kondo temperature depends on the gate voltage [59]. In particular, around the charge neutrality point, the Kondo temperature shows a nonzero minimum value and almost symmetric dependence for the positive and negative gate voltages.

3. **Defect scattering of conduction electrons**
   In the theory of Kondo effects in ordinary metals, effects of defect or impurity scattering on the conduction electrons are neglected, because such scattering usually causes relatively small change of density of states (DOS) of conduction electrons, and it is irrelevant to low-energy behaviors. In graphene, however, the DOS near the charge neutrality point is small, and the modulation of the conduction electron states by the defect scattering can play important roles.

4. **Negative magnetoresistance**
   Experimentally, a negative magnetoresistance has been observed in addition to that from the weak localization, and it is considered to be due to the Kondo effect. In the usual Kondo effect, the energy scale of a characteristic magnetic field of the negative magnetoresistance is the same order as that of the Kondo temperature. However, experimentally, the characteristic magnetic field is one tenth smaller than the value expected from the Kondo temperature, which means that this Kondo effect is sensitive to the magnetic field.

In this chapter, the first and second points are clarified in §2.2.1 and §2.4, respectively. This part has been published in ref. [73]. On the third point, although a model has been proposed where the localized state of π electrons is rather artificially added at the defect [74], more consideration on the derivation of the model seems to be necessary. In §2.2.2, we develop a one-dimensional representation of the conduction electron states which naturally includes the effects of defect scattering. By using this model, the effects of defect scattering on the π electrons are studied in §2.5.

After the studies of ref. [73, 74], the Kondo effect in graphene with defects has been studied theoretically in several works [75, 76, 77]. However, studies on the fourth point are limited [78]. In §2.6, we discuss this point in relation to behaviors of the localized state of π electrons in magnetic field.

Here, we mention another interpretation of the experiment [59]: It has been proposed that the electron-electron interaction in the presence of the disorder is responsible for the

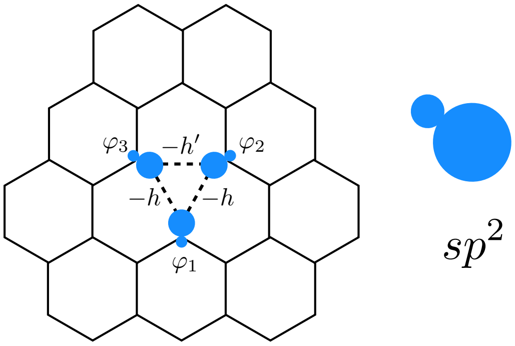

Figure 2.9: Schematic picture of a point defect in graphene and sp^2 orbitals (circles) around it (φ_i, $i = 1, 2,$ and 3). $-h$ and $-h'$ are transfer integrals between them.

logarithmic increase of the resistivity at low temperatures [79, 80]. Further experimental studies are needed on this issue. In this chapter, we explore the possibility of the Kondo effect.

2.2 Localized Moment and its Hybridization with Conduction Electrons

2.2.1 Cluster Model for the Defect

Here, considering a cluster model for the defect, we clarify the origin of the localized magnetic moment and its hybridization with conduction electrons. Figure 2.9 shows the schematic picture of the point defect in graphene. Around the point defect, there are three sp^2 orbitals φ_i (circles) which do not form covalent bond, where i indicates one of the three sites (i = 1, 2, or 3) around the defect. There are also π orbitals on carbon atoms which are not shown in Fig. 2.9.

First, we consider an isolated cluster that consists of three sp^2 orbitals, as depicted in Fig. 2.9, as a model for the localized state of sp^2 orbitals around the defect. A tight-binding approximation is applied to this cluster. In Fig. 2.9, $-h$ and $-h'$ are transfer integrals between the sp^2 orbitals ($h, h' > 0$). The threefold symmetric structure corresponds to the case with $h = h'$, and the twofold symmetric one to $h' > h$, where it is assumed that the distance between sites 2 and 3 is shorter than the others.

The energy eigenvalues and the corresponding wave functions of this cluster model are

$$\begin{aligned}
E_3 &= h', & \psi_3 &= \frac{1}{\sqrt{2}}(\varphi_2 - \varphi_3), \\
E_2 &= \frac{-h' + \sqrt{8h^2 + h'^2}}{2}, & \psi_2 &= C_+\varphi_1 - \frac{1}{\sqrt{2}}C_-(\varphi_2 + \varphi_3), \\
E_1 &= \frac{-h' - \sqrt{8h^2 + h'^2}}{2}, & \psi_1 &= C_-\varphi_1 + \frac{1}{\sqrt{2}}C_+(\varphi_2 + \varphi_3),
\end{aligned} \tag{2.5}$$

with

$$C_\pm = \left[\frac{1}{2}\left(1 \pm \frac{h'}{\sqrt{8h^2 + h'^2}}\right)\right]^{1/2}, \tag{2.6}$$

which are depicted in Fig. 2.10. There are three electrons on these sp^2 orbitals. Since the number of electrons is odd, there is an unfilled level and nonzero spin appears. Interpreting the Kohn-Sham eigenvalues of the DFT calculations [66] in terms of these tight-binding energy levels, we semiquantitatively estimate h'/h to be $h'/h \simeq 5$. The comparison between the eigenvalues (2.5) and the Kohn-Sham eigenvalues is shown in Figs. 2.11. When $h'/h \simeq 5$, $C_\pm$ becomes $C_+ \simeq 1$, $C_- \ll 1$, and the wave function of the lowest level ψ_1 becomes a bonding state $\psi_1 = (\varphi_2 + \varphi_3)/\sqrt{2}$, while the second state becomes $\psi_2 = \varphi_1$. Thus, φ_1 becomes the highest occupied molecular orbital of this cluster, and causes a localized magnetic moment. It should be noted that in a divacancy case, four electrons are present in the sp^2 orbitals and the localized spin does not appear.

Second, we consider the hybridization between this localized magnetic moment on the sp^2 orbital and the conduction electrons which consist of π orbitals. It depends on the lattice structure of the defect. When the defect has the planar structure, there is no hybridization between the sp^2 and π orbitals, which is schematically shown in Fig. 2.12(a). However, with an out-of-plane displacement, finite hybridization between the sp^2 orbital φ_i and the two π orbitals at the other sites $j \neq i$ appears as in Fig. 2.12(b). As mentioned above, from the DFT calculations, the twofold symmetric structure with an out-of-plane displacement is suggested to be more stable owing to the Jahn-Teller effect [66].

In the following we consider the structure shown in Fig. 2.13, where only one sp^2 orbital ($i = 1$) is active and it hybridizes with the π orbitals at sites 2 and 3. (The bonding state of sp^2 orbitals at sites 2 and 3 is neglected.) We assume that the hybridization term is given by

$$H_{\mathrm{hyb}} = \sum_{\sigma=\uparrow\downarrow}\left[V\left(a^\dagger_{2\sigma} + a^\dagger_{3\sigma}\right)d_\sigma + \mathrm{h.c.}\right], \tag{2.7}$$

where $a_{i\sigma}$ is an annihilation operator of a π electron at site i with spin $\sigma =\uparrow, \downarrow$ and d_σ is an annihilation operator of an electron on the sp^2 orbital at site $i = 1$. V is the amplitude

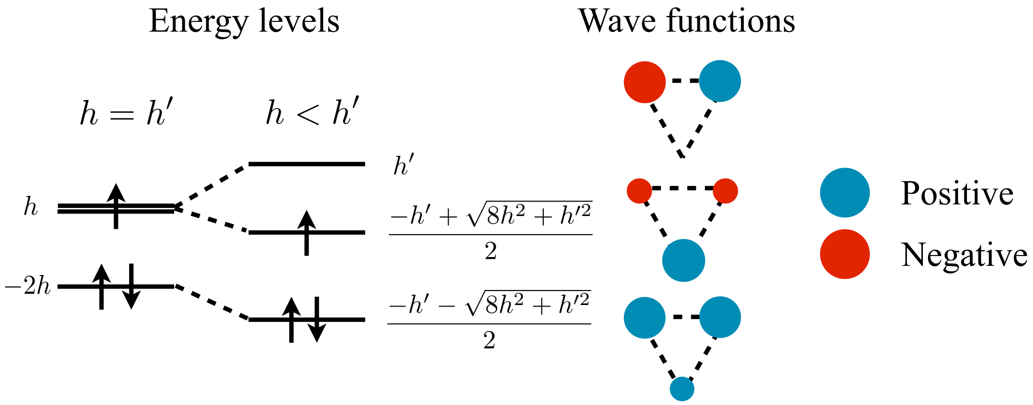
Energy levels
Wave functions
$h = h'$
$h < h'$
h'
h
$-2h$
$\frac{-h' + \sqrt{8h^2 + h'^2}}{2}$
$\frac{-h' - \sqrt{8h^2 + h'^2}}{2}$
Positive
Negative

Figure 2.10: Energy levels and the corresponding wave functions of a cluster model for localized states of sp^2 orbitals around a point defect in graphene. The energy levels and the eigenvalues are shown for the case of $h = h'$ and $h < h'$, which correspond to the threefold symmetric defect and the twofold distorted one, respectively. In the former, the highest energy levels degenerate, while in the latter, these levels split. There are three electrons in these levels, where the arrows mean electrons with spin. In the case of $h < h'$, the second level becomes the highest occupied molecular orbital (HOMO). The wave functions are schematically shown on the right of each energy level. The size of the circles represents the amplitude of the wave function on each sp^2 orbital. The colors (blue or red) denote its signs (positive or negative, respectively). When $h \ll h'$, the wave function of the second level localizes on one of the sp^2 orbitals.

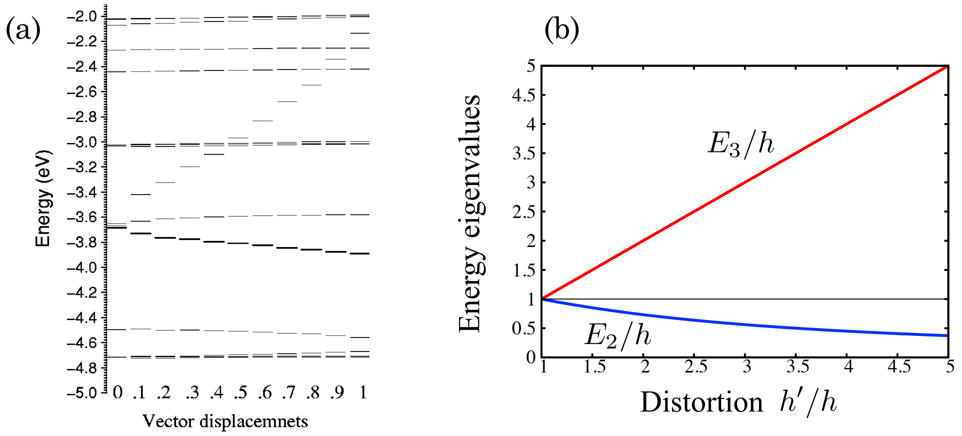

Figure 2.11: (a) Kohn-Sham eigenvalues of graphene with a point defect as a function of distortion [66]. The structure is linearly interpolated from the threefold symmetric one to the twofold distorted one, which correspond to the vector displacement of 0. and 1, respectively. The two branches of levels which show significant variation of energy correspond to the σ states localized at the defect. The degenerate levels in the threefold symmetric structure split into two levels with the distortion. [Reprinted figure with permission from A. A. El-Barbary *et al.*, Phys. Rev. B **68** (2003) 144107. Copyright (2003) by the American Physical Society.] (b) Energy eigenvalues of the cluster model E_3/h and E_2/h as a function of h'/h.

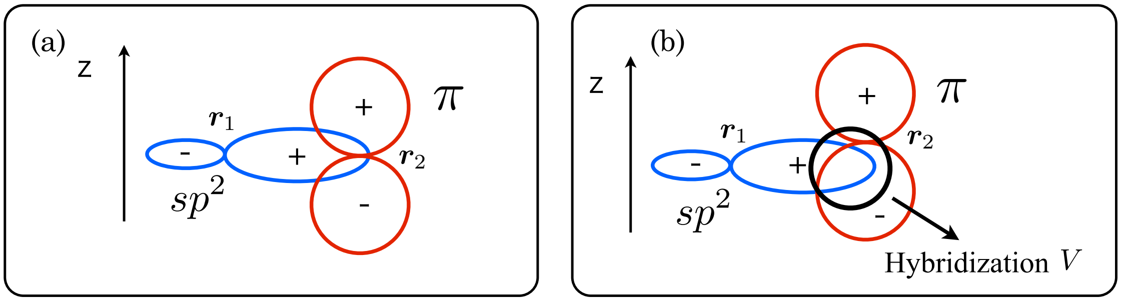

Figure 2.12: Schematic picture of sp^2 (blue) and π (red) orbitals on the different carbon atoms at $\boldsymbol{r}_1$ and $\boldsymbol{r}_2$. The signs (+ and −) represent those of the orbitals. z axis is perpendicular to the graphene plane. (a) Planar structure. The hybridization integral vanishes owning to the sign change of the π orbital. (b) In the presence of out-of-plane displacement of the carbon atom. Finite hybridization V appears owning to the relative displacement of the π orbital.

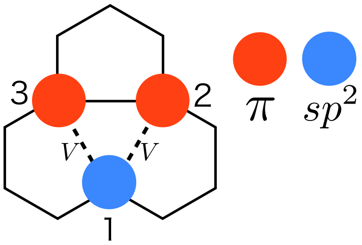

Figure 2.13: Schematic picture of the electronic state around the defect. Two of the three sp^2 orbitals ($i = 2, 3$) form a covalent bond. The circle at the site 1 shows the active sp^2 orbital and those at the sites 2 and 3 the π orbitals. V is the amplitude of the hybridization between the active sp^2 orbital and the two π orbitals.

of hybridization. Taking account of the localized nature of the active sp^2 orbital in the defect, we assume that the effective Hamiltonian for this orbital becomes

$$H_{\mathrm{def}} = \sum_{\sigma} (\epsilon_{sp^2} - \mu) d_{\sigma}^{\dagger} d_{\sigma} + U d_{\uparrow}^{\dagger} d_{\uparrow} d_{\downarrow}^{\dagger} d_{\downarrow}, \tag{2.8}$$

where ϵ_{sp^2}, μ, and U are the energy level, chemical potential, and Coulomb interaction on the sp^2 orbital, respectively. The Coulomb interaction term is essential for describing the Kondo effect.

The conduction electron states are formed by π orbitals in graphene, which are described by the following tight-binding model with a nearest-neighbor transfer integral $t(> 0)$ [10],

$$H_{\mathrm{gra}} = -t \sum_{\langle ij \rangle \sigma}{}' \left(a_{i\sigma}^{\dagger} b_{j\sigma} + \mathrm{h.c.} \right) - \mu N, \tag{2.9}$$

where $b_{j\sigma}$ is an annihilation operator of a π electron at site j of the sublattice B, and N is the total number of π electrons. In eq. (2.7), only the π orbitals of the sublattice A, $a_{i\sigma}$, appear since we have assumed the missing carbon atom to be on the sublattice B. The prime in eq. (2.9) denotes the presence of the point defect. The point defect in π electrons is represented by the zero transfer integrals between the missing site and the neighboring site. Here, we ignore the Coulomb interaction in the π orbitals. Although band structure may be modified by the Coulomb interaction in the bulk as mentioned in §1.2, the Dirac dispersion is preserved and we assume that eq. (2.9) represents such renormalized Dirac fermions. Finally, the effective Hamiltonian of graphene with the point defect becomes $H = H_{\mathrm{gra}} + H_{\mathrm{def}} + H_{\mathrm{hyb}}$.

2.2.2 One-Dimensional Representation of the Conduction Electron States

To clarify the conduction electron states which are coupled with the sp^2 orbital at the defect, and to apply the NRG method, we transform this effective Hamiltonian (2.7), (2.8), and (2.9) into a one-dimensional representation. In the usual Kondo problems, a magnetic impurity interacts with conduction electrons at the same site. In this case, the conduction electron states are expanded by the spherical waves, and states with particular symmetries such as s, p, or d wave symmetries are coupled with the impurity. For example, when the interaction between the impurity and the conduction electrons is spherical, only the states with s wave symmetry is coupled with the impurity. Such states are labeled by the wave vectors in the radial direction. As a result, a one-dimensional representation is obtained. However, in the present model, there are two centers: the sp^2 orbital at the defect interacts with the π orbitals of sites 2 and 3. Such a geometry has been treated in the two-impurity Kondo problem [81]. We follow the method developed for it [81, 82, 83], generalizing the method to include the effects of defect scattering on the π conduction electrons.

To express the hybridization term (2.7) in a one-dimensional representation, we introduce the following operator for π electrons [82, 83];

$$a^\dagger_{\varepsilon i\sigma} = \sum_k c^\dagger_{k\sigma} \langle k|Ai\rangle \delta\left(\varepsilon - \varepsilon_k\right), \tag{2.10}$$

where ε_k and $|k\rangle$ are the energy eigenvalues and the wave functions of the Hamiltonian (2.9), and $c^\dagger_{k\sigma}$ is the corresponding creation operator with spin σ. $|Ai\rangle$ represents the π electron state localized at the site $i(= 2$ or $3)$ of sublattice A. $\delta(\varepsilon)$ is the Dirac delta function. These operators are related to the original one $a_{i\sigma}$ by

$$\int \mathrm{d}\varepsilon a_{\varepsilon i\sigma} = a_{i\sigma}. \tag{2.11}$$

The anti-commutation relations of these operators are calculated as $\left\{a_{\varepsilon i\sigma}, a^\dagger_{\varepsilon' j\sigma}\right\} = \delta\left(\varepsilon - \varepsilon'\right) g_{ij}(\varepsilon)$, $\{a_{\varepsilon i\sigma}, a_{\varepsilon' j\sigma}\} = 0$, and $\left\{a^\dagger_{\varepsilon i\sigma}, a^\dagger_{\varepsilon' j\sigma}\right\} = 0$, where $g_{ij}(\varepsilon)$ is introduced as

$$g_{ij}(\varepsilon) = \sum_k \langle k|Ai\rangle \langle Aj|k\rangle \delta\left(\varepsilon - \varepsilon_k\right). \tag{2.12}$$

The diagonal element $g_{ii}(\varepsilon)$ corresponds to the LDOS at site i of sublattice A. Owning to the twofold symmetry in the present system, the LDOS at the site i = 1 and 2 are identical: $g_{22}(\varepsilon) = g_{33}(\varepsilon)$. The off-diagonal elements satisfy $g_{23}(\varepsilon) = g_{32}(\varepsilon)$, since the wave functions can be chosen to be real. Then, from $a_{\varepsilon 2\sigma}$ and $a_{\varepsilon 3\sigma}$, the following operators which satisfy the usual anti-commutation relations are obtained;

$$c_{\varepsilon\sigma e} = \frac{1}{N_e^{1/2}(\varepsilon)} \left(a_{\varepsilon 2\sigma} + a_{\varepsilon 3\sigma} \right), \tag{2.13}$$

$$c_{\varepsilon\sigma o} = \frac{1}{N_o^{1/2}(\varepsilon)} \left(a_{\varepsilon 2\sigma} - a_{\varepsilon 3\sigma} \right), \tag{2.14}$$

where e and o denote even and odd, respectively, and

$$\begin{aligned} N_e(\varepsilon) &= g_{22}(\varepsilon) + g_{23}(\varepsilon) + g_{32}(\varepsilon) + g_{33}(\varepsilon), \\ N_o(\varepsilon) &= g_{22}(\varepsilon) - g_{23}(\varepsilon) - g_{32}(\varepsilon) + g_{33}(\varepsilon). \end{aligned} \tag{2.15}$$

With these operators, the hybridization term (2.7) is expressed as

$$H_{\text{hyb}} = \sum_\sigma \int \mathrm{d}\varepsilon N_e^{1/2}(\varepsilon) \left(V c^\dagger_{\varepsilon\sigma e} d_\sigma + \text{h.c.} \right). \tag{2.16}$$

Since $N_e(\varepsilon)$ is essentially the LDOS of π electrons at the defect, this expression shows the importance of the LDOS at the defect, not the total DOS. Note that only one channel of the conduction electron $c_{\varepsilon\sigma e}$ hybridizes with the sp^2 orbital. This is because the sp^2 orbital hybridizes equally with the π orbitals at sites 2 and 3 as in Fig. 2.13. When the hybridization is not equal, both even and odd states are coupled to the sp^2 orbital.

Using eqs. (2.9), (2.10), and (2.13), it can be shown that $c_{\varepsilon\sigma e}$ satisfies the commutation relation $\left[H_{\text{gra}}, c^\dagger_{\varepsilon\sigma e}\right] = (\varepsilon - \mu) c^\dagger_{\varepsilon\sigma e}$. Thus, neglecting the other channels of the conduction electrons, we assume that the conduction electron term (2.9) can be written as [81, 82, 83]

$$H_{\text{gra}} = \sum_\sigma \int \mathrm{d}\varepsilon \, (\varepsilon - \mu) \, c^\dagger_{\varepsilon\sigma e} c_{\varepsilon\sigma e}. \tag{2.17}$$

Since decoupled channels of conduction electrons are neglected, this model can be used only when the defect contribution is concerned. The transformation above has also been justified in ref. [84] by integrating out the conduction electron degrees of freedom in the functional integral representation.

2.3 Numerical Renormalization Group Method

Here, the NRG method is briefly reviewed [85]. In the NRG method, the conduction electron states near the Fermi energy are treated as accurately as possible and the those far from the Fermi energy less accurately. Such a treatment is implemented by the following steps.

1. Logarithmic intervals
   The states which are continuously distributed in the range $|\varepsilon| < D$ are divided into logarithmic intervals as $\Lambda^{-m-1} < |\varepsilon| < \Lambda^{-m}$, where Λ is a parameter with $\Lambda > 1$ and $m = 0, 1, 2, \cdots$.

2. Discretization
   In each interval, the creation operator of conduction electrons is expanded with a Fourier transformation. By retaining only the constant Fourier component in each interval, the original continuous Hamiltonian is approximated by discrete one. The original continuous Hamiltonian can be recovered in the limit $\Lambda \to 1$.

3. Mapping onto a semi-infinite chain
   This discretized model is mapped onto a semi-infinite chain, with the impurity at the zeroth site.

4. Truncation
   This semi-infinite chain is truncated at the Nth site and diagonalized numerically.

The important point in the fourth step is that a scaling factor $\sim \Lambda^{-N/2}$ is introduced simultaneously. The truncated Hamiltonian H_N is related to the semi-infinite chain Hamiltonian H by

$$H = \lim_{N\to\infty} \alpha \Lambda^{-(N-1)/2} H_N. \tag{2.18}$$

Then, H_N satisfies the following recursion formula,

$$H_{N+1} = \Lambda^{1/2} H_N + \sum_\sigma \left[\Lambda^{-1/2} \epsilon_{N+1} c^\dagger_{N+1\sigma} c_{N+1\sigma} + t_N \left(c^\dagger_{N\sigma} c_{N+1\sigma} + c^\dagger_{N+1\sigma} c_{N\sigma} \right) \right], \tag{2.19}$$

$$H_0 = \Lambda^{-1/2} \left[\sum_\sigma \epsilon_0 c^\dagger_{0\sigma} c_{0\sigma} + \frac{1}{\alpha} (H_{\rm def} + H_{\rm hyb}) \right], \tag{2.20}$$

$$H_{\rm hyb} = VF \sum_\sigma \left(c^\dagger_{0\sigma} d_\sigma + \text{h.c.} \right), \tag{2.21}$$

where $c_{n\sigma}$ and $c^\dagger_{n\sigma}$ are annihilation and creation operators of the conduction electrons with spin σ on the nth site of the chain. $\alpha = (1 + \Lambda^{-1})/2$ and F are factors. t_N and ϵ_{N+1} are the "hopping parameter" and the "on-site potential", respectively. These parameters reflect the DOS of the conduction electrons (or $N_e(\varepsilon)$ in the present model), and have numerical values of order of unity [86].

Using the recursion formula (2.19), the truncated Hamiltonian is diagonalized successively from H_0 to H_N. In every diagonalization, higher energy states are eliminated. This procedure corresponds to a renormalization group transformation, namely, coarse graining and subsequent scale transformation. The elimination of higher energy states corresponds to the coarse graining. The scale transformation is included in eq. (2.19) as the factor $\Lambda^{1/2}$ in front of H_N. Owning to this factor, the energy eigenvalues in every diagonalization remain finite with values of order of unity.

By using the resulting energy eigenvalues $E_N(r)$ and many-body eigenstates $|r\rangle_N$, where r represents a set of quantum numbers, thermodynamic quantities at finite temperatures are calculated as follows [85]. Because of the scaling factor $\Lambda^{-(N-1)/2}$ in eq. (2.18), the energy eigenvalues in the original scale $\tilde{E}_N(r)$ are related to $E_N(r)$ by

$$\tilde{E}_N(r) \sim \Lambda^{-(N-1)/2} E_N(r). \tag{2.22}$$

The partition function of H_N is introduced as

$$Z_N = \sum_r \mathrm{e}^{-E_N(r)/T}, \tag{2.23}$$

where $1/T$ is a constant of order of unity. Because of eq. (2.22), the factors $E_N(r)/T$ in the exponential function are written as

$$\frac{E_N(r)}{T} \sim \frac{\tilde{E}_N(r)}{T\Lambda^{-(N-1)/2}}, \tag{2.24}$$

which shows that the thermodynamic quantities at the temperature $T\Lambda^{-(N-1)/2}$ can be obtained from Z_N.

Entropy of the whole system S_N is calculated as

$$S_N = \frac{1}{T}\langle H_N \rangle + \log Z_N, \tag{2.25}$$

where

$$\frac{1}{T}\langle H_N \rangle = \frac{1}{Z_N} \sum_r \frac{E_N(r)}{T} \mathrm{e}^{-E_N(r)/T}. \tag{2.26}$$

The important quantity is the impurity contribution to the entropy, S_N^{imp}, which is defined as the difference between the entropy in the presence of impurity and that without it:

$$S_N^{\mathrm{imp}} = S_N - S_N^{\mathrm{bath}}. \tag{2.27}$$

The entropy of the conduction electrons S_N^{bath} is calculated directly from the conduction electron Hamiltonian. Other thermodynamic quantities are also calculated in the same way. In the following, Λ is set to be $\Lambda = 2$, and 300 states are retained in every step of diagonalization.

2.4 Low-Energy States and the Kondo Temperature

To clarify the low-energy states and to calculate the physical quantities, we apply the NRG method for the model of eqs. (2.8), (2.16), and (2.17), following the formalism of ref. [86].

When the density of defects is low, distances between the defects are large and the overlaps between the localized states of π electrons at different defects are almost zero. In this case, the LDOS of π electrons at the defect has a form of Dirac delta function as a function of energy, and does not contribute to the Kondo screening. On this consideration, here we investigate the model without the localized state of π electrons. The effect of the localized state of π electrons is discussed in the next section.

In this case, by diagonalizing in $\boldsymbol{k}$ space and retaining low-energy states, the Hamiltonian of the conduction electrons (2.9) is expressed as [10, 56]

$$H_{\rm gra} = \sum_{\sigma} \sum_{n=1,2} \sum_{\tau=\pm} \int_{|\boldsymbol{k}|<k_c} {\rm d}\boldsymbol{k} \left[\varepsilon_n(\boldsymbol{k}) - \mu\right] c^{\dagger}_{\boldsymbol{k}\sigma n\tau} c_{\boldsymbol{k}\sigma n\tau}, \tag{2.28}$$

with the linear dispersion $\varepsilon_n(\boldsymbol{k}) = (-1)^n v_F|\boldsymbol{k}|$, where v_F is Fermi velocity, and $n(=1,2)$ and $\tau(=\pm)$ are band and valley indices, respectively. Here, the Dirac points are located at $\boldsymbol{K}_{\pm} = (\pm 4\pi/3a, 0)$ in the Brillouin zone corresponding to the two valleys, with a being the lattice constant. $\boldsymbol{k}$ is measured from $\boldsymbol{K}_{\pm}$ for $\tau = \pm$. The region of the $\boldsymbol{k}$ integral is limited to $|\boldsymbol{k}| < k_{\rm c}$, where $k_{\rm c}$ is a cut-off wave number. The annihilation operator of sublattice A, $a_{i\sigma}$, is expanded in $c_{\boldsymbol{k}\sigma s\tau}$ as

$$a_{i\sigma} = \sqrt{\frac{\Omega_{\rm cell}}{2(2\pi)^2}} \sum_{n\tau} \int {\rm d}\boldsymbol{k} {\rm e}^{{\rm i}(\boldsymbol{k}+\boldsymbol{K}_\tau)\cdot \boldsymbol{r}_i} c_{\boldsymbol{k}\sigma n\tau}, \tag{2.29}$$

where $\Omega_{\rm cell}$ is the area of the unit cell of graphene, and $\boldsymbol{r}_2 = \boldsymbol{R}/2$ and $\boldsymbol{r}_3 = -\boldsymbol{R}/2$ with $\boldsymbol{R} = (a, 0)$.

In the present case, the one-dimensional representation of conduction electrons derived in §2.2.2 is explicitly obtained. The operator introduced in eq. (2.10) is written as

$$a_{\varepsilon i\sigma} = \sqrt{\frac{\Omega_{\rm cell}}{2(2\pi)^2}} \sum_{n\tau} \int {\rm d}\boldsymbol{k} \delta(\varepsilon_n(\boldsymbol{k}) - \varepsilon) {\rm e}^{{\rm i}(\boldsymbol{k}+\boldsymbol{K}_\tau)\cdot \boldsymbol{r}_i} c_{\boldsymbol{k}\sigma n\tau}, \tag{2.30}$$

which leads to an expression of $N_{e,o}$ introduced in eq. (2.15) as

$$N_{e,o}(\varepsilon) = \frac{\Omega_{\rm cell}}{\pi v_F^2}|\varepsilon| \left[1 \mp \frac{1}{2} J_0\left(\frac{|\varepsilon|}{v_F}a\right)\right]. \tag{2.31}$$

Here, $J_0(x)$ is the zeroth Bessel function. Using these operators, the hybridization term (2.7) is written as

$$H_{\rm hyb} = V \sum_{\sigma} \int_{-D}^{D} {\rm d}\varepsilon N_e^{1/2}(\varepsilon) \left(c^{\dagger}_{\varepsilon\sigma e} d_\sigma + {\rm h.c.}\right), \tag{2.32}$$

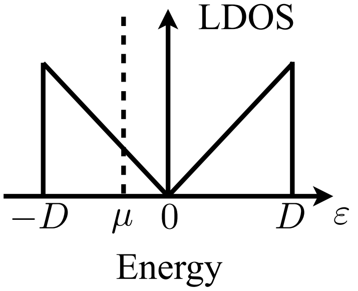

Figure 2.14: Local density of states of conduction electrons in the model in §2.4 as a function of energy ε, where μ and D are a chemical potential and a cut-off energy, respectively.

where a cut-off energy D is introduced. Since the dependence of $J_0(|\varepsilon|a/v_F)$ on small $|\varepsilon|a/v_F$ is weaker than $|\varepsilon|$, we approximate $J_0(|\varepsilon|a/v_F)$ as $J_0(0)(=1)$. By assuming that $(\Omega_{\text{cell}}/2\pi v_F^2)^{1/2} \simeq 1/D$, the hybridization term is expressed as

$$H_{\text{hyb}} = \frac{V}{D}\sum_{\sigma}\int_{-D}^{D} \mathrm{d}\varepsilon|\varepsilon|^{1/2}\left(c^{\dagger}_{\varepsilon\sigma e}d_{\sigma} + \text{h.c.}\right). \tag{2.33}$$

This model of eqs. (2.8), (2.17), and (2.33) is known as the single-channel pseudogap Anderson model [86] with a finite chemical potential, where the DOS of the conduction electrons is proportional to $|\varepsilon|$ as shown in Fig. 2.14. The Kondo problem in such pseudogap systems has been studied in detail [86] for the case with $\mu = 0$. The main feature for $\mu = 0$ is as follows. In the particle-hole symmetric ($2\epsilon_{sp^2} + U = 0$) case, no Kondo screening occurs, i.e. the localized moment is not screened by conduction electrons. On the other hand, in the particle-hole asymmetric ($2\epsilon_{sp^2} + U \neq 0$) case, the localized moment is screened when the coupling constant V is larger than a critical value V_c. In real materials, the system is expected to be particle-hole asymmetric. In ref. [86], the particle-hole symmetric case and the $U = \infty$ case were mainly treated, and the case with realistic particle-hole asymmetry has not been studied in detail. Hence, we focus on the particle-hole asymmetric case with realistic parameters. We also study the chemical potential dependence, which previously has not been studied in detail.

To clarify the low-energy states of this model in the parameter space (V, μ), we calculate the temperature dependence of the entropy of the electron on the sp^2 orbital, S_{def}, by the NRG method. The bandwidth of graphene is about $D \simeq 8$ eV [10]. We assume that $\epsilon_{sp^2} \simeq -1$ eV and $U \simeq 3$ eV [68]. Thus we use the parameters $\epsilon_{sp^2}/D = -0.125$ and $U/D = 0.375$, in the following. First, we investigate the $\mu = 0$ case.

Figure 2.15 shows S_{def} as a function of temperature T/D for three values of hybridization V ($V/D = 0.4$, 0.6311, and 0.8). It is found that the critical value of hybridization for the present parameters is $V_c/D = 0.6311$. At $V = V_c$, S_{def} becomes $\log 3$, which is

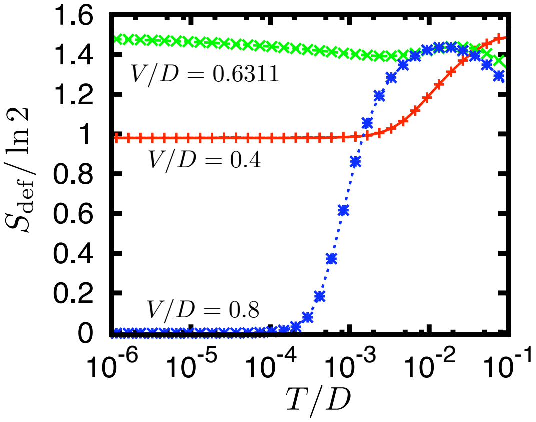

Figure 2.15: Entropy of electron on the sp^2 orbital, $S_{\rm def}$, at chemical potential $\mu = 0$ as a function of temperature T/D for the hybridization $V/D = 0.4$, 0.6311, and 0.8. Here, the Boltzmann constant is $k_B = 1$. [Reprinted figure with permission from T. Kanao, H. Matsuura, and M. Ogata, J. Phys. Soc. Jpn. **81** (2012) 063709. Copyright (2012) by the Physical Society of Japan.]

known as the valence-fluctuation fixed point of the pseudogap system [86]. For $V < V_c$, the entropy remains $\log 2$ at the lowest temperature ($\sim 10^{-6}D$), which indicates an unscreened localized moment. For $V > V_c$, $S_{\rm def}$ goes to zero, indicating that the localized moment is screened. Despite there being no conduction electron DOS at $\mu = 0$, the Kondo screening occurs owing to the particle-hole asymmetry.

Figure 2.16 shows $S_{\rm def}$ as a function of chemical potential μ/D and temperature T/D for the same values of hybridization V ($V/D = 0.4$, 0.6311, and 0.8). In Figs. 2.16(a) and 2.16(b), we can see that $S_{\rm def}$ goes to zero at low temperatures when $\mu \neq 0$. For $V > V_c$ [Fig. 2.16(c)], $S_{\rm def}$ goes to zero at low temperatures for all values of μ.

Combining these data, we plot the low-temperature V-μ phase diagram in Fig. 2.17. The whole region is divided into the local-moment (LM) region and the asymmetric strong-coupling (ASC) region. The valence-fluctuation (VF) fixed point is located at $V = V_c$, $\mu = 0$.

In the experiment [59], it is observed that the Kondo temperature depends on the gate voltage. In particular, at the charge neutrality point ($\mu = 0$), the Kondo temperature has a finite value, and it shows an almost symmetric dependence for the positive and negative gate voltages.

In order to compare the NRG result with those of the experiment, we plot the Kondo temperature as a function of μ/D for four values of hybridization V/D in Fig. 2.18. Here, the Kondo temperature T_K is defined by the relation $S_{\rm def}(T_K)/\log 2 = 1/2$. In the experimental situation, the chemical potential μ can be varied by applying the gate voltage in the range of $|\mu| \lesssim 0.2$ eV ($\simeq 0.025D$) [18]. As shown in Fig. 2.18, $T_K \ll 10^{-6}D$

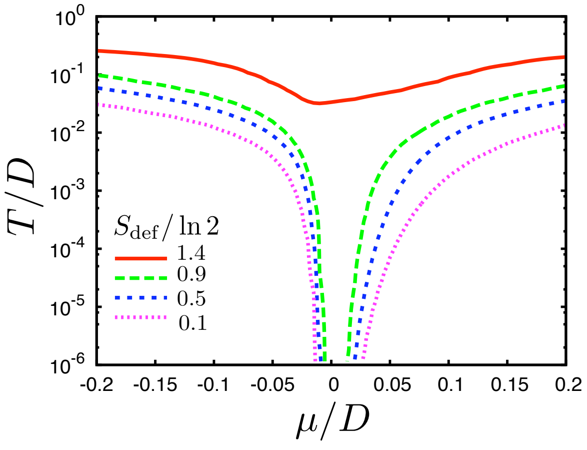

(a) $V/D = 0.4$

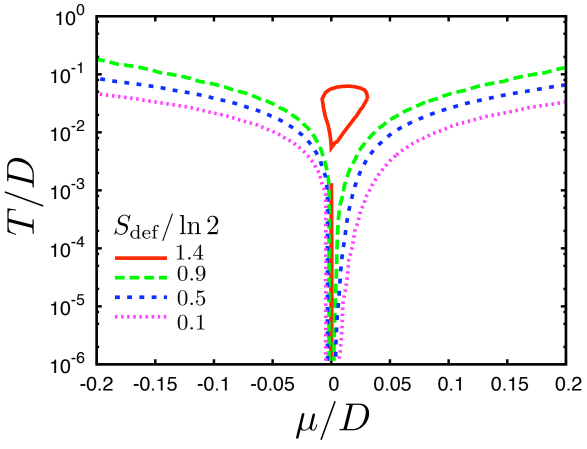

(b) $V/D = 0.6311$

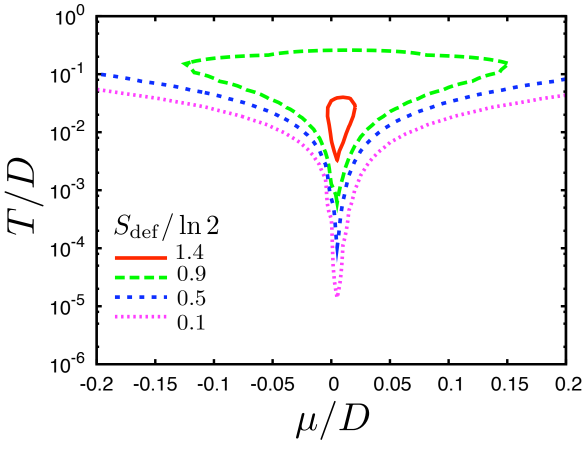

(c) $V/D = 0.8$

Figure 2.16: Contour plots of $S_{\mathrm{def}}/\log 2$ as a function of chemical potential μ/D and temperature T/D. [Reprinted figure with permission from T. Kanao, H. Matsuura, and M. Ogata, J. Phys. Soc. Jpn. **81** (2012) 063709. Copyright (2012) by the Physical Society of Japan.]

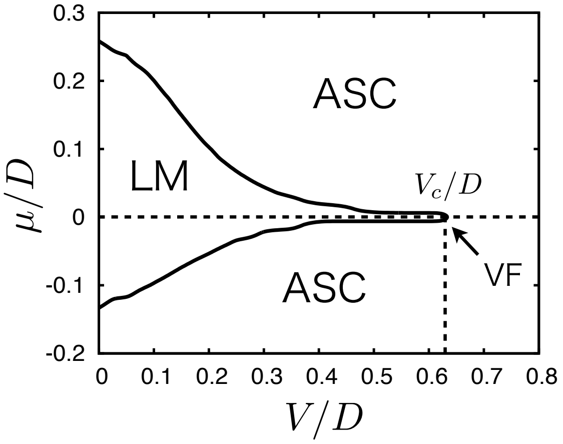

Figure 2.17: Local-moment (LM) region and asymmetric strong-coupling (ASC) region in the low-temperature hybridization-chemical potential diagram. The valence-fluctuation (VF) fixed point is located at $V_c/D = 0.6311$, $\mu/D = 0$. [Reprinted figure with permission from T. Kanao, H. Matsuura, and M. Ogata, J. Phys. Soc. Jpn. **81** (2012) 063709. Copyright (2012) by the Physical Society of Japan.]

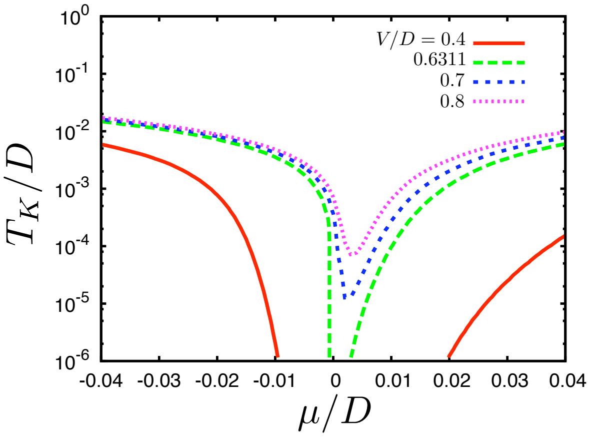

Figure 2.18: Kondo temperature as a function of chemical potential μ/D for four values of hybridization V/D. Here, $\epsilon_{sp^2}/D = -0.125$ and $U/D = 0.375$. [Reprinted figure with permission from T. Kanao, H. Matsuura, and M. Ogata, J. Phys. Soc. Jpn. **81** (2012) 063709. Copyright (2012) by the Physical Society of Japan.]

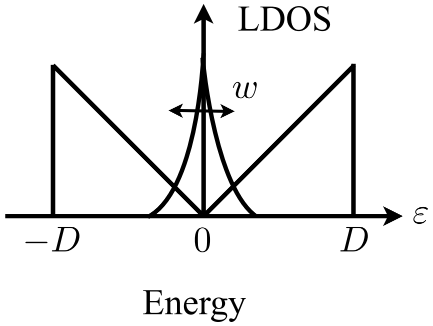

Figure 2.19: Local density of states of conduction electrons in the model in §2.5 as a function of energy ε, where D is a cut-off energy. A peak due to a localized state of π electrons is included, where w is a width of the peak.

for $V \leq V_c$ at $\mu = 0$. However, T_K is finite for $V > V_c$ even at $\mu = 0$. This behavior reproduces the experimental behavior. We find the almost symmetric dependence on the positive and negative chemical potentials. Note that this feature is not obtained in the $U = \infty$ case [55], where T_K becomes totally asymmetric.

2.5 Role of the Localized State of π Electrons at the Defect

In this section, we consider the effect of the localized state of π electrons on the Kondo effect. As shown in Fig. 2.8, the localized state of π electrons causes a peak in the LDOS on the defect as a function of energy at the charge neutrality point. To take into account this peak of the LDOS, we assume a model shown in Fig. 2.19,

$$N_e(\varepsilon) = |\varepsilon| + \frac{\lambda}{2w} \mathrm{e}^{-|\varepsilon|/w}, \tag{2.34}$$

where λ and w are the intensity and the width of the peak, respectively. The second term becomes a Dirac delta function in the limit $w \to 0$. In the case of low density of defects, as mentioned in the previous section, the LDOS at the defect is a Dirac delta function with zero width. On the other hand, in the case of finite concentration of defects, the LDOS can have a finite width owning to overlaps of the wave functions of the localized states on different defects [87, 88]. Assuming finite widths of the LDOS, we analyze this model by the NRG method. The $\mu = 0$ case is studied, where effect of the peak of the LDOS is most significant.

Figure 2.20(a) shows the temperature dependence of entropy of the electron on the defect sp^2 orbital, $S_{\mathrm{def}}/\log 2$, for $V/D = 0.01$, 0.05, and 0.1 in the presence of finite peak width $w/D = 0.01$. The other parameters are the same as in §2.4. It is found that the

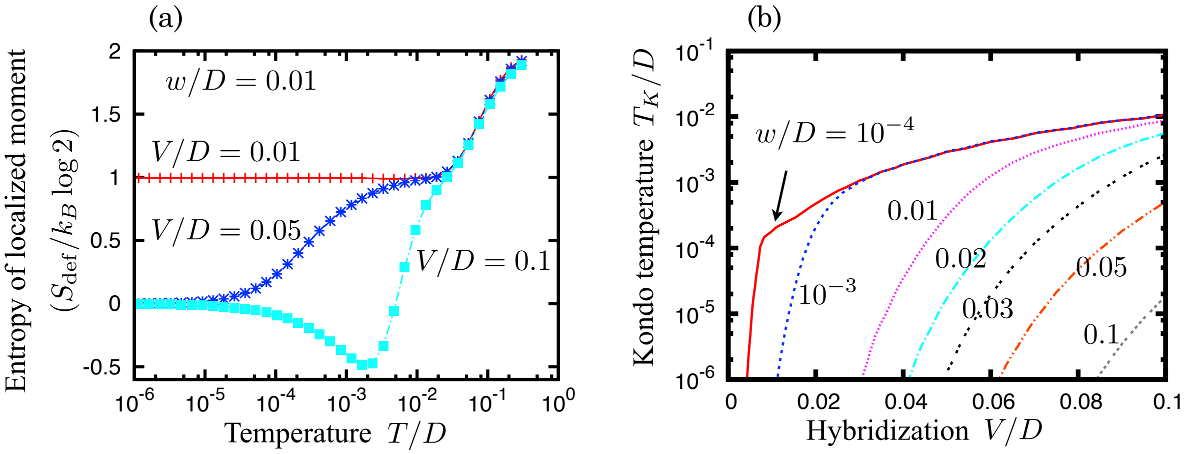

Figure 2.20: (a) Temperature dependence of entropy of the electron on the defect sp^2 orbital, $S_{\rm def}/\log 2$, in the presence of a peak in the local density of states of π electrons with the width $w/D = 0.01$ at the chemical potential $\mu = 0$, for the hybridization $V/D = 0.01$, 0.05, and 0.1. (b) Kondo temperature T_K/D as a function of hybridization V/D for several widths w/D.

low-energy state ($\sim 10^{-6}D$) changes from the unscreened localized moment state to the Kondo-Yosida singlet state with increasing hybridization from $V/D = 0.01$ to 0.05. This is about one tenth smaller than the critical value of hybridization without the peak of the LDOS. In the case of $V/D = 0.1$, $S_{\rm def}$ is negative in a certain range of temperature. The similar behavior has been known in the narrow-band Anderson model [89].

In Fig. 2.20(b), the Kondo temperatures T_K/D as a function of V/D for several w/D are shown. The Kondo temperature sensitively depends on w/D. With smaller w/D, T_K becomes larger owning to the larger LDOS at the Fermi energy. The Kondo effect can occur with a realistic smaller value of hybridization between the sp^2 orbital at the defect and the π electrons.

2.6 Effects of Magnetic Field

As mentioned in §2.1.2, a negative magnetoresistance has been observed experimentally in this Kondo effect [59]. In the usual Kondo effect, the Zeeman effect on the localized magnetic moment causes a negative magnetoresistance, because it suppresses the formation of the Kondo-Yosida single. The Kondo-Yosida singlet is suppressed when the energy scales of the magnetic field and the Kondo temperature become the same order, which leads to a characteristic magnetic field in the negative magnetoresistance. In the Kondo effect in graphene with defects, however, the experimentally observed characteristic magnetic field is smaller than the energy scale of its Kondo temperature by one

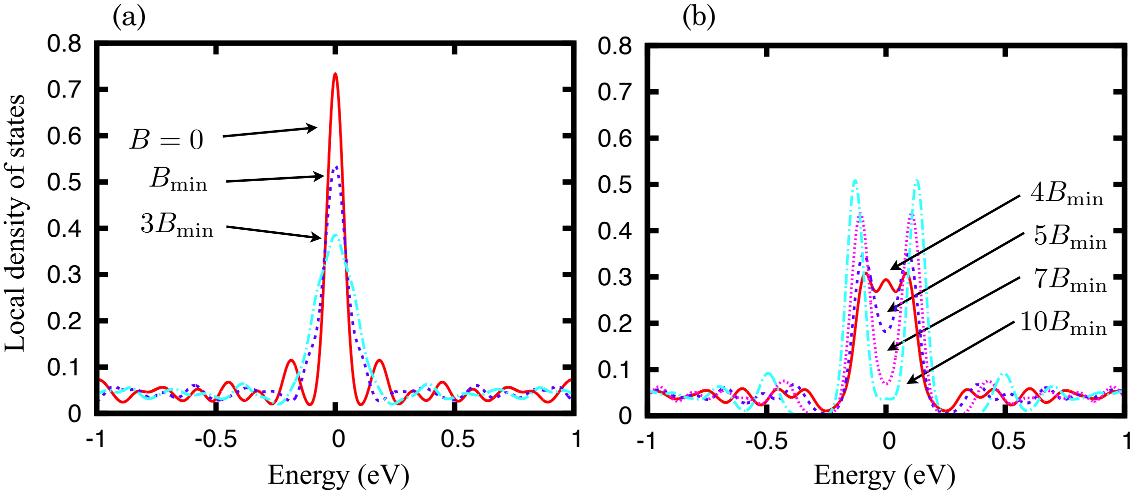

Figure 2.21: Local density of states of the π electrons at a point defect as a function of energy in the magnetic filed of (a) $B/B_{\mathrm{min}} = 0$, 1, and 3 and (b) $B/B_{\mathrm{min}} = 4$, 5, 7, and 10. B_{min} is determined by the system size. In the present calculation, $B_{\mathrm{min}} \simeq 21.2$ T.

order of magnitude (Fig. 2.4). This means that this Kondo effect is more sensitive to the magnetic field than the usual one. The origin of this behavior has not been understood.

First, to clarify the origin of this behavior of the negative magnetoresistance, we study the effect of the Zeeman field on the model in §2.4 by the NRG method. The Zeeman field is added to H_{def} [eq. (2.8)]. We calculate the magnetization of the sp^2 orbital at the defect as a function of the Zeeman field at low temperature. As a result, the usual behavior is observed, i.e. the magnetization shows an increase around $h \sim T_K$ with increasing Zeeman field, which indicate the suppression of the Kondo-Yosida singlet. This implies that the characteristic magnetic field due to the Zeeman effect is the same order as the Kondo temperature, which does not explain the experimental fact. In this model, we have found an unusual fixed point at the border of the spin polarized state and the Kondo-Yosida singlet state at $\mu = 0$. At this fixed point, the entropy is $\log 2$ and the expectation value of S_z^2 is $1/8$. The analysis of this fixed point is described in the appendix of this chapter.

Second, we consider the orbital effect of magnetic field on the π electrons. In the previous section, we have shown that the Kondo screening is assisted by the peak of the LDOS of π electrons which is caused by the defect scattering. Since the Kondo temperature sensitively depends on the height of the peak, small modulation of the localized state by the magnetic field will cause appreciable change in the Kondo screening.

To clarify the effect of the orbital motion of the π electrons in the magnetic field, we solve the nearest-neighbor tight-binding model for the π states of graphene in the magnetic field with a single point defect. The orbital effect of the magnetic field is introduced by the Peierls phase with the “string gauge” [90]. Under the periodic boundary condition, the possible magnetic fields are restricted to $B = nB_{\rm min}$ with $n = 0, 1, 2, \cdots$, where $B_{\rm min}$ is determined by the system size. In the present calculation, 61^2 unit cells are used, which corresponds to $B_{\rm min} \simeq 21.1$ T.

Figures 2.21 show the LDOS at the defect as a function of energy in several magnetic fields. We find that the height of the peak decreases and the width increases for relatively small B as shown in Fig. 2.21(a). At higher magnetic fields, the peak splits into two peaks as shown in Fig. 2.21(b). Since the Kondo screening is suppressed with decreasing peak height, this indicates that the orbital effect on the π electrons in magnetic field can cause a Kondo effect which is sensitive and weak against the magnetic field.

2.7 Summary and Discussions

The Kondo effect due to point defects in graphene has been investigated, where the electronic state and the lattice structure of the defect are taken into account. We have shown that the localized magnetic moment on the dangling sp^2 orbital at the defect can interact with the π conduction electrons if the lattice around the defect is distorted in the direction perpendicular to the graphene plane. We have developed an effective model for this Kondo effect, and found that the resulting one-dimensional representation of the model is a single-channel Anderson model. In this model, the characteristic feature of the Dirac conduction electrons appears through the local density of states (LDOS) at the defect. Through the LDOS, this model can include the effects of the localized state of π electrons which appears at the defect. We have analyzed low-energy behaviors of the resulting model by the numerical renormalization group (NRG) method.

First, assuming low density of the defects, we have investigated the model without the localized state of π electrons. When the hybridization between the sp^2 and π orbital is large, the Kondo temperature shows a nonzero minimum value at the zero chemical potential and almost symmetric dependence for the positive and negative chemical potentials. The effect of Zeeman field has also been investigated in this model. It has been shown that the effect of Zeeman field is rather usual in this model.

Second, assuming a finite density of the defects, we have studied the effect of the localized state of π electrons. We have shown that this localized state assists the Kondo screening when the chemical potential is at the Dirac points. In relation to this behavior, we have studied the effect of the orbital motion of the π electrons in magnetic field, and found that the orbital motion reduces the LDOS of π electrons at the defect.

Here, we discuss the relevance of the above results to the experimental facts on the Kondo effect in graphene with defects. The chemical potential dependence of the Kondo temperature obtained in the case of low density of defects can qualitatively explain the dependence observed experimentally at low gate voltage. Yet, the critical hybridization without the localized states of π electrons, $V_c \simeq 0.6D$, is rather large compared with the band width. When the localized states of π electrons are included, which corresponds to the case with finite density of defects, the critical hybridization can be one tenth smaller than this value, which is considered to be more realistic. However, since the Kondo temperature depends exponentially on the parameters in the model, quantitative fitting of the experimental results is difficult.

The reduction of the LDOS of π electrons at the defect by the orbital motion in magnetic field will suppress the Kondo screening, and hence will explain the tendency experimentally observed in magnetic field. To discuss the magnetoresistance quantitatively, calculations using the NRG method with the LDOS in the magnetic field will be necessary.

Appendix of Chapter 2 Effect of Zeeman Field

In this appendix, we study effects of Zeeman field on the low-energy states of the model in §2.4. The contents of this appendix have been published in ref. [78]. The Zeeman field h is introduced into the Hamiltonian for the defect sp^2 orbital (2.8) as

$$H_{\mathrm{def}} = \sum_{\sigma} (\epsilon_{sp^2} - \mu) d_{\sigma}^{\dagger} d_{\sigma} + U d_{\uparrow}^{\dagger} d_{\uparrow} d_{\downarrow}^{\dagger} d_{\downarrow} - \sum_{\sigma} h \sigma d_{\sigma}^{\dagger} d_{\sigma}. \tag{2.35}$$

In addition to S_{def}, we calculate the temperature dependence of the expectation value of square of the z component of localized moment, $\langle S_z^2 \rangle_{\mathrm{def}}$ in the NRG method. The parameters $\epsilon_{sp^2}/D = -0.125$ and $U/D = 0.375$ are the same as in the previous sections.

Figure 2.22(a) shows S_{def} as a function of temperature for the hybridization $V/D =$ 0.4, 0.6330, and 0.8 in the Zeeman field $h/D = 10^{-4}$ at $\mu = 0$. For the case with $V/D =$ 0.4 and 0.8, $S_{\mathrm{def}} \simeq 0$ at low temperatures. However, their temperature dependences are different: At $V/D = 0.4$, for $T \simeq 10^{-4} D (\simeq h)$, S_{def} changes from $\log 2$ to $\log 1 = 0$. In this case, the ground state is a spin polarized state. In contrast, at $V/D = 0.8$, S_{def} changes from $\log 3$ to $\log 1$ for $T/D \simeq 10^{-3}$. This temperature is much larger than the Zeeman field $h/D = 10^{-4}$. Thus, the ground state is considered to be the Kondo-Yosida singlet state. At a critical point $V/D = 0.6330$, we find that S_{def} approaches $\log 2$ at the lowest temperature as shown in the inset of Fig. 2.22(a).

To obtain more information on the electronic states at low energies, we calculate $\langle S_z^2 \rangle_{\mathrm{def}}$. Figure 2.22(b) shows $\langle S_z^2 \rangle_{\mathrm{def}}$ as a function of temperature for the same parameters. For the case with $V/D = 0.4$ and 0.8, we find $\langle S_z^2 \rangle_{\mathrm{def}} \simeq 1/4$ and 0, respectively at low temperature. This confirms the ground states suggested above: the spin polarized state for $V/D = 0.4$, and the Kondo-Yosida singlet state for $V/D = 0.8$. We also find that $\langle S_z^2 \rangle_{\mathrm{def}}$ suddenly changes from 1/4 to 0 at $V/D = 0.6330$ when V is changed. Thus, $V/D = 0.6330 \simeq \tilde{V}_c/D$ is a critical value which separates the spin polarized state and the Kondo-Yosida singlet state. At $V \simeq \tilde{V}_c$, $\langle S_z^2 \rangle_{\mathrm{def}} \simeq 1/8$.

The critical value in the Zeeman field $\tilde{V}_c$ is larger than the critical value V_c at $h = 0$, because the Kondo-Yosida singlet state is suppressed by the Zeeman field. We suppose that $\tilde{V}_c$ is determined by the relation $T_K \sim h$, where T_K is the Kondo temperature. The values of $S_{\mathrm{def}} = \log 2$ and $\langle S_z^2 \rangle_{\mathrm{def}} = 1/8$ at $\tilde{V}_c$ imply that there are two degenerate impurity states at this point. We expect that these two states are up-spin state and empty (unoccupied) state, since $\langle S_z^2 \rangle_{\mathrm{def}} = 1/8$ can be interpreted as $[(1/2)^2 + 0]/2$. This situation has been studied with perturbative renormalization group methods, and the same interpretation has been suggested [91].

At finite chemical potentials in the Zeeman field, S_{def} is always zero at low temperatures. At low temperatures, $\langle S_z^2 \rangle_{\mathrm{def}}$ shows the change from $\langle S_z^2 \rangle_{\mathrm{def}} = 1/4$ to 0 as V increases. Any unusual fixed point is not observed in this case.

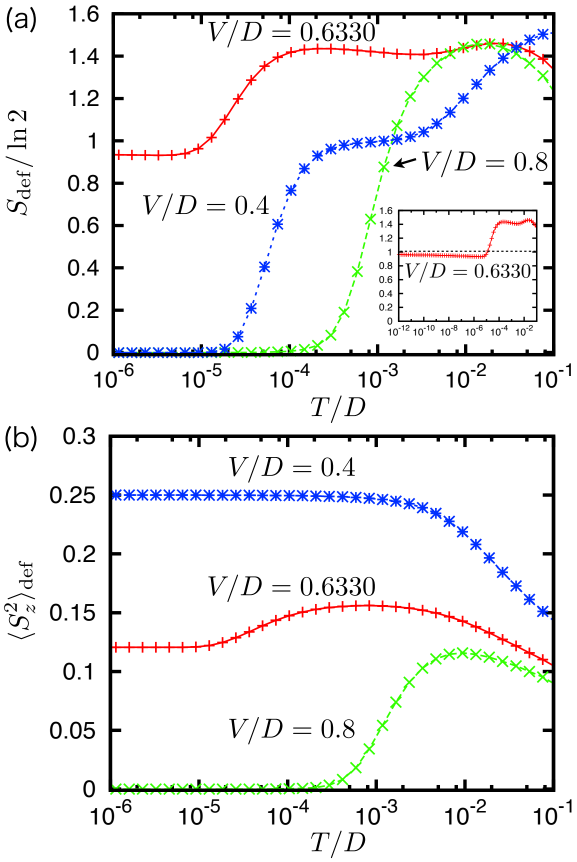

Figure 2.22: (a) Temperature dependence of entropy of the electron on the defect sp^2 orbital, $S_{\rm def}$, in the Zeeman field $h/D = 10^{-4}$ at the chemical potential $\mu = 0$ for the hybridization $V/D = 0.4$, 0.6330, and 0.8. The inset shows $S_{\rm def}$ at $V/D = 0.6330$ for $10^{-12} < T/D < 10^{-1}$. (b) Temperature dependence of expectation value of S_z^2, $\langle S_z^2 \rangle_{\rm def}$, for the same parameters as in (a). [Reprinted figure with permission from T. Kanao, H. Matsuura, and M. Ogata: J. Phys.: Conf. Ser. **456** (2013) 012018. Copyright (2013) by IOP Publishing Ltd.]

Chapter 3

Localized State in α-(BEDT-TTF)$_2$I$_3$ Induced by Single Defect

As mentioned in chapter 2, a localized state of Dirac fermions is induced by a single defect in graphene. In this chapter, we investigate whether such a state is induced by a single defect in α-(BEDT-TTF)$_2$I$_3$ by using a realistic tight-binding model which describes Dirac fermions in this material. After a brief introduction on defects in this material in §3.1, the model is introduced in §3.2. By diagonalizing the Hamiltonian with a single defect in §3.3, it is demonstrated that a localized state is induced at the energy of Dirac point when the defect is at the site A or A'. This localized state enhances the local density of states in a finite region around the defect, and it shows an anisotropy. In §3.4, the existence of this localized state is confirmed by using the Green's function method, and its wave function is evaluated in the $\boldsymbol{k}$ space. It is clarified that this localized state consists of both the electron and hole states near the Dirac points, and shows anisotropy around the Dirac points due to the tilting of the Dirac cones in α-(BEDT-TTF)$_2$I$_3$. The anisotropy of the localized state in the real space is understood from this tilting of the Dirac cones in the $\boldsymbol{k}$ space. The sublattice components of the wave function are also calculated in the $\boldsymbol{k}$ space. When the defect is placed at the sublattice A, the largest contribution to the induced localized state is the sublattice A' component, and vice versa. The experimental detection of this localized state is discussed in §3.5. The results are summarized in §3.6.

3.1 Introduction

As reviewed in chapter 1, the massless Dirac fermions in α-(ET)$_2$I$_3$ under pressure have been established by both experimental and theoretical studies. For the massless Dirac fermions, a temperature-independent resistivity is expected. However, it has been reported

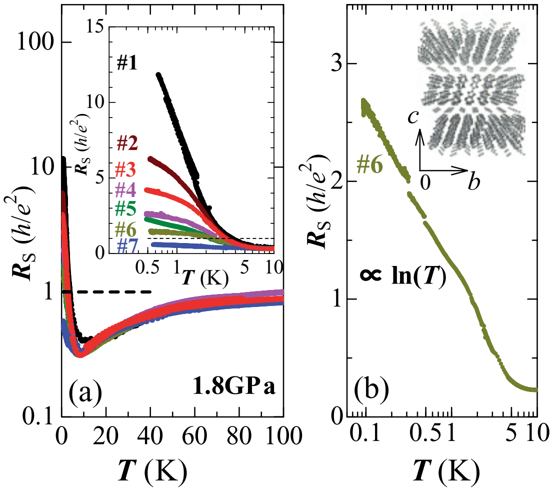

Figure 3.1: (a) Temperature dependence of sheet resistivity of α-(BEDT-TTF)$_2$I$_3$ for several samples under the pressure of 1.8 GPa [92]. The inset shows the sheet resistivity at temperatures below 10 K. (b) Temperature dependence of the sheet resistivity for sample 6 plotted in logarithmic scale. [Reprinted figure with permission from N. Tajima *et al.*, Phys. Rev. B **85** (2012) 033401. Copyright (2012) by the American Physical Society.]

that the resistivity exhibits a logarithmic increase below ~ 5 K as shown in Fig. 3.1 [92]. Because this behavior shows sample dependence and because the impurity concentration in this material is usually very small ($\lesssim 10^{-6}$), defects have been suggested to be responsible for it. In this material, the defects of ET molecules or I_3^- anions are possible. As other causes of this behavior, effects of electron-electron interaction and randomness have been also suggested in ref. [92]. Another unclear problem on this material is whether other carriers are present in addition to the Dirac fermions [93].

Generally, defects (or impurities) in solids have long been studied, because they can change macroscopic properties of the solid or because they can be used as a microscopic probe of the electronic states of the bulk. The electronic states around defects have been measured microscopically by using the scanning tunneling microscopy (STM) and scanning tunneling spectroscopy (STS), or in the case of finite concentration of defect, by the nuclear magnetic resonance (NMR).

As mentioned in chapter 2, the effects of defects have been studied in detail in graphene. By a point defect, a localized state is induced at the energy of the Dirac points [63, 64, 69, 70, 71, 72, 88]. When the particle-hole symmetry is present as in the nearest-neighbor tight-binding model on the honeycomb lattice, the induced state is "quasilocalized": its wave function decays in a power law. On the other hand, when the particle-hole symmetry is broken by, for example, introducing next-nearest-neighbor transfer integrals, then the state becomes a resonance [70, 88]. The existence of the localized state at the energy of Dirac points in the former case can be related to chiral symmetry [88, 94]. The chiral symmetry is defined by $\{\varGamma, \mathcal{H}\} = 0$, where $\mathcal{H}$ and $\varGamma$ are the Hamiltonian and a chiral operator which satisfies $\varGamma^2 = 1$, respectively. A point defect can be modeled by forbidding the hopping into the missing site. Such a defect preserves the chiral symmetry as follows. In this case, the Hamiltonian can be written with the creation and annihilation operators introduced in eq. (1.2) as

$$H = \sum_{\sigma=\uparrow\downarrow} \begin{pmatrix} a^\dagger_{1\sigma} \cdots a^\dagger_{N\sigma} \, b^\dagger_{1\sigma} \cdots b^\dagger_{N\sigma} \end{pmatrix} \mathcal{H} \begin{pmatrix} a_{1\sigma} \\ \vdots \\ a_{N\sigma} \\ b_{1\sigma} \\ \vdots \\ b_{N\sigma} \end{pmatrix}, \tag{3.1}$$

$$\mathcal{H} = \begin{pmatrix} & h \\ h^\dagger & \end{pmatrix}, \tag{3.2}$$

where there is no hopping between the same sublattices. Then, the chiral operator expressed as

$$\varGamma = \begin{pmatrix} 1 & \\ & -1 \end{pmatrix}, \tag{3.3}$$

satisfies $\{\varGamma, \mathcal{H}\} = 0$. If ψ and E are an eigenstate and its energy eigenvalue, then $\varGamma\psi$ is another eigenstate and its energy eigenvalue is $-E$. Thus the chiral symmetry ensures a particle-hole symmetric energy spectrum. If odd number of states are induced by the defect, at least one state must appear at $E = 0$.

On α-(ET)$_2$I$_3$, however, theoretical studies on the effect of defects are limited so far [95, 96], and it is not clear whether such a localized state is induced by defect in this material, which has a lattice structure with a lower symmetry and more sublattice degrees of freedom than graphene. Although the Dirac cones are tilted and the conventional chiral symmetry is broken in this material, a generalized chiral symmetry has been found in the effective Hamiltonian for such a tilted Dirac cone system [94].

In this chapter, we investigate the effects of a single defect on the Dirac fermions in α-(ET)$_2$I$_3$ with the emphasis on its characteristic lattice and band structure, namely, the four sublattice degrees of freedom and the tilted Dirac cones. We ignore electron-electron interaction in this chapter, and concentrate on the one-electron model. The one-electron model will give valid qualitative picture as long as there are no charge or magnetic orders. Effects of the electron-electron interaction are investigated in chapter 4.

3.2 Tight-Binding Model with a Single Defect

According to the density functional theory calculations [34, 97], the energy band of α-(ET)$_2$I$_3$ near the Fermi energy is formed by the highest occupied molecular orbital (HOMO) of the ET molecule. The band structure near the Fermi energy is well reproduced by the tight-binding Hamiltonian consisting of the nearest-neighbor and the next-nearest-neighbor transfer integrals [34]. Between the conducting layers of ET molecules, there are insulating layers of I$_3^-$ anions. Because the interlayer transfer integrals are estimated to be about 10^{-2} times smaller than those of intralayer, we ignore the interlayer transfer integrals and concentrate on a single isolated two-dimensional conducting layer.

The tight-binding Hamiltonian without defect is written as

$$H_0 = \sum_{\sigma=\uparrow,\downarrow} \sum_{i,j} \sum_{\alpha,\beta=A,A',B,C} t_{i\alpha;j\beta} c^{\dagger}_{i\alpha\sigma} c_{j\beta\sigma}, \tag{3.4}$$

where the indices i and j represent the unit cells of α-(ET)$_2$I$_3$. As introduced in chapter 1, there are four ET molecules (sites) in a unit cell A, A', B, and C, which are represented by indices α and β. The index $\sigma =\uparrow\downarrow$ represents the spin of an electron. $c^{\dagger}_{i\alpha\sigma}$ and $c_{j\beta\sigma}$ are the corresponding creation and annihilation operators of electrons on the HOMO of the ET molecule. The transfer integrals $t_{i\alpha;j\beta}$ of ref. [34] (under ambient pressure at 8 K in Table III) are used. These transfer integrals reproduce the Dirac cones in the $\boldsymbol{k}$ space, and the energy of the Dirac points coincides with the Fermi energy. No other Fermi surface is present in this model. In this study, the Fermi energy is fixed at the value determined by the condition that the electron density is 3/4 when the defect is not present. In this chapter, the origin of energy is taken at the Fermi energy. The band dispersion calculated from the tight-binding model in ref. [34] is shown in Fig. 3.2. The direction of k_x and k_y axes are chosen to be that of axes $-b$ and a, respectively.

The ideal vacancy defect of ET molecule is modeled by zero transfer integrals between the defect site and the surrounding sites. This situation, where electrons cannot enter the defect site, is also realized by putting an infinitely strong on-site potential $I \to \infty$,

$$H' = I \sum_{\sigma=\uparrow\downarrow} c^{\dagger}_{i^*\alpha^*\sigma} c_{i^*\alpha^*\sigma}, \tag{3.5}$$

on the defect at the sublattice α^* in the unit cell i^*. We calculated both cases, and confirmed the equivalence of them. In this study, the results of the case with an infinitely strong on-site potential $I \to \infty$ are mainly shown. In real material, however, the scattering potential caused by defect is finite, as has been pointed out in the graphene case [72]. The case of finite scattering potential is discussed in §3.4.

As shown in Fig. 3.3, I$_3^-$ anions are located on the sites C or on the neighboring two sites of A and A' when they are projected on the two-dimensional ET plane [26, 95].

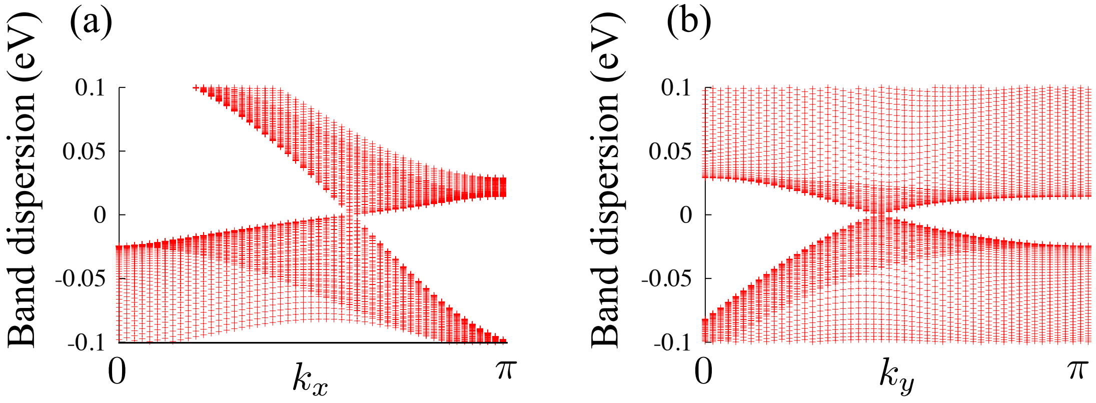

Figure 3.2: Band dispersion of α-(BEDT-TTF)$_2$I$_3$ near the Fermi energy calculated from the tight-binding model in ref. [34]. Here, lattice constants are unity, and the Fermi energy is zero. The direction of k_x and k_y axes are chosen to be that of axes $-b$ and a, respectively. The band dispersion in the region of $0 < k_x < \pi$, $0 < k_y < \pi$ is projected on the planes of (a) $k_y = 0$ and (b) $k_x = 0$.

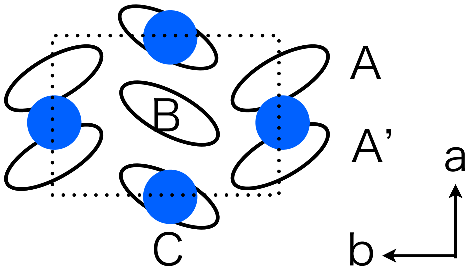

Figure 3.3: Location of I$_3^-$ anions (blue filled circles), which are projected on a two-dimensional BEDT-TTF plane [26, 95]. The dotted rectangle denotes a unit cell. The directions of a and b axes are shown.

Thus, a vacancy defect of I_3^- anion causes scattering potential on these sites. To study the effects of an I_3^- anion defect, we also calculate the case of on-site potential on two neighboring sites A and A'.

3.3 Diagonalization of Hamiltonian with a Single Defect

To clarify whether localized states are induced by a single defect or not, we directly diagonalize the Hamiltonian $H = H_0 + H'$ in the real space. In the following, the spin degree of freedom is neglected. One defect is placed at the center, and the periodic boundary condition is assumed. The diagonalization yields the energy eigenvalues ϵ_l and the wave functions $\psi_l(\boldsymbol{r}_{i\alpha})$ with l being the labels of the eigenstates.

First, in order to estimate the degree of localization of every state $|l\rangle$, we calculate the inverse participation ratio (IPR) which is defined as [70]

$$P_l = \sum_i \sum_{\alpha=A,A',B,C} \left|\psi_l(\boldsymbol{r}_{i\alpha})\right|^4, \tag{3.6}$$

assuming the normalization condition $\sum_{i\alpha} \left|\psi_l(\boldsymbol{r}_{i\alpha})\right|^2 = 1$. P_l has the following properties: $0 < P_l \leq 1$, and $P_l \to 1$ when the state is localized, and $P_l \sim 1/N_s \to 0$ when extended in the limit of infinite system size $N_s \to \infty$. When a localized state decays exponentially with a localization length ξ_l, it is related to P_l by

$$\xi_l \sim \frac{a}{\sqrt{2\pi P_l}}, \tag{3.7}$$

in two-dimensional systems, where a is a lattice constant.

In Fig. 3.4, the IPRs of each eigenstate with a defect at A, A', B, C, or two neighboring defects at A and A' are plotted against its energy eigenvalue. The total density of states (DOS) without defect (in arbitrary unit) is also shown. Around the origin of the energy, the DOS shows a linear energy dependence due to the Dirac dispersion. Here, the case of $I \to \infty$ is shown with the number of sites $N_s = 4 \times 51^2$. It is found that the localized states appear at the energy of the Dirac points and in the band gap around -0.1 eV when the defect site is A or A'. The localization lengths of these states are estimated by using eq. (3.7) as $\xi_l/a \sim 5$ and 2, respectively, which shows that the localized state at the Dirac points is extended in a finite region. All the other states are extended.

To clarify the relation to the "quasilocalized" state in graphene mentioned in §3.1, we investigate system-size dependence of the IPR of these localized states. It has been known that the IPR of the quasilocalized state vanishes logarithmically as $\sim 1/\log^2 N_s$ [88]. Figure 3.5 shows the system-size dependence of the IPR of the localized states in α-(ET)$_2$I$_3$. Within the number of sites calculated, the IPRs of both localized states saturate,

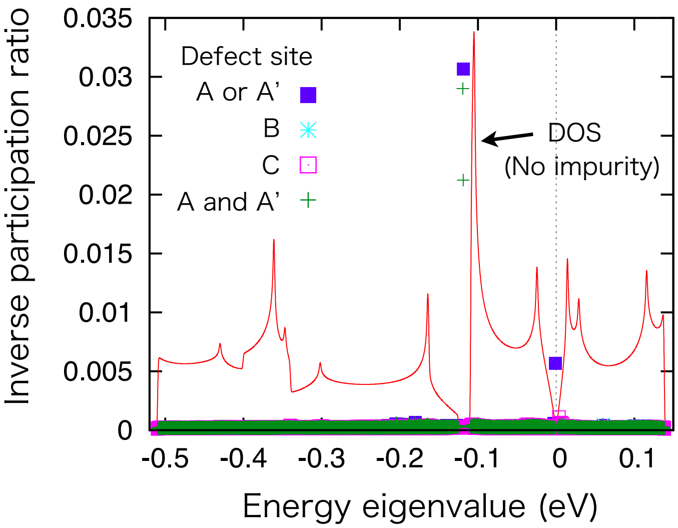

Figure 3.4: Inverse participation ratio (IPR) of each eigenstate in the presence of a defect, plotted against its energy eigenvalue. The cases of the defect on sublattice A, A, B, C, or both A and A' are shown. The origin of energy is taken at the Fermi energy. Here, the total number of sites is $N_s = 4 \times 51^2 = 10404$. The total density of states without defect (in arbitrary unit) is also shown.

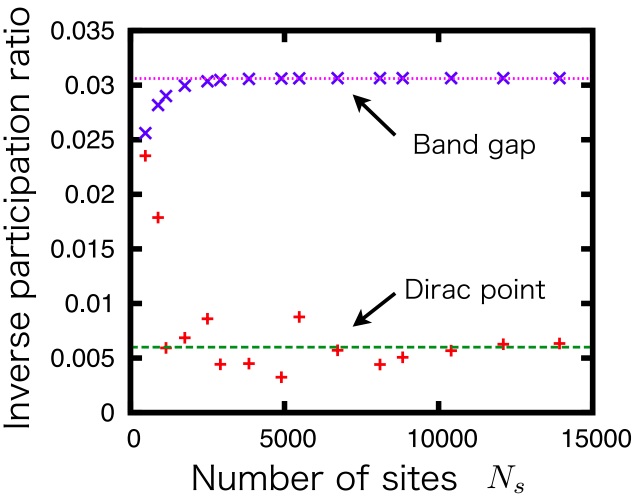

Figure 3.5: System-size dependence of IPRs of localized states induced by a defect at site A. The IPRs of the localized states both at the Dirac points and in the band gap are shown. The broken lines represent saturated values of the IPRs for each state.

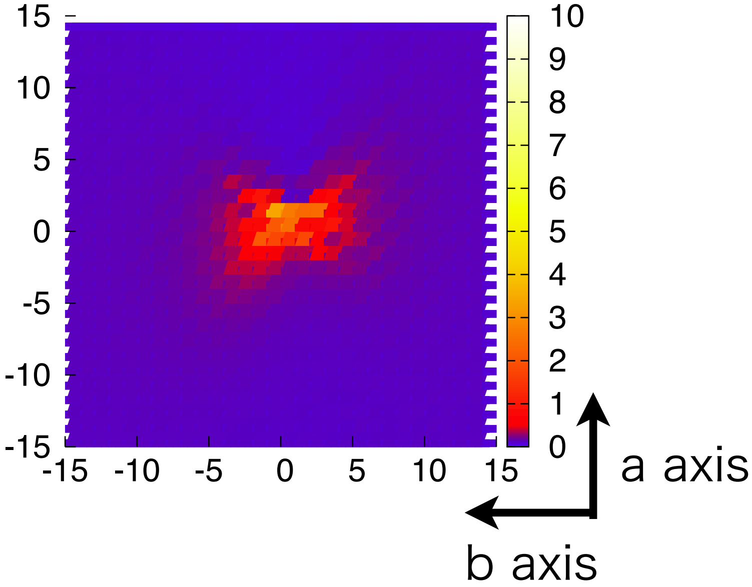

Figure 3.6: Real-space map of local density of states for $\omega = 0$ eV around a defect at the site A, which is placed at the origin (the center). The directions of a and b axes are shown.

and do not show the quasilocalized behavior. The absence of the quasilocalized behavior can be related to the absence of the particle-hole symmetry around the Dirac points in this material [88]. Note that, however, the saturation of the IPR for the localized state at the Dirac points is slow compared with the rapid saturation for the localized state in the band gap.

When the defects are placed at both A and A', localized states appear only in the band gap. In the case of defect at B or C, no localized state is induced. Since the defect at C or the two neighboring defects at both A and A' correspond to the I_3^- anion defect, this result shows that in the case of an I_3^- anion defect, the localized state is not induced at the energy of the Dirac points.

Second, local density of states (LDOS) in the presence of the defect is calculated, which can be measured experimentally by the STM and STS. To improve numerical accuracy, the supercell method is used, where the defects are placed periodically. In this method, the LDOS is given by [98]

$$\rho(\boldsymbol{r}_{i\alpha}, \omega) = \frac{1}{N_{\mathrm{sc}}} \sum_{\boldsymbol{k}l} \left|\psi_{\boldsymbol{k}l}(\boldsymbol{r}_{i\alpha})\right|^2 \delta(\omega - \epsilon_{\boldsymbol{k}l}), \tag{3.8}$$

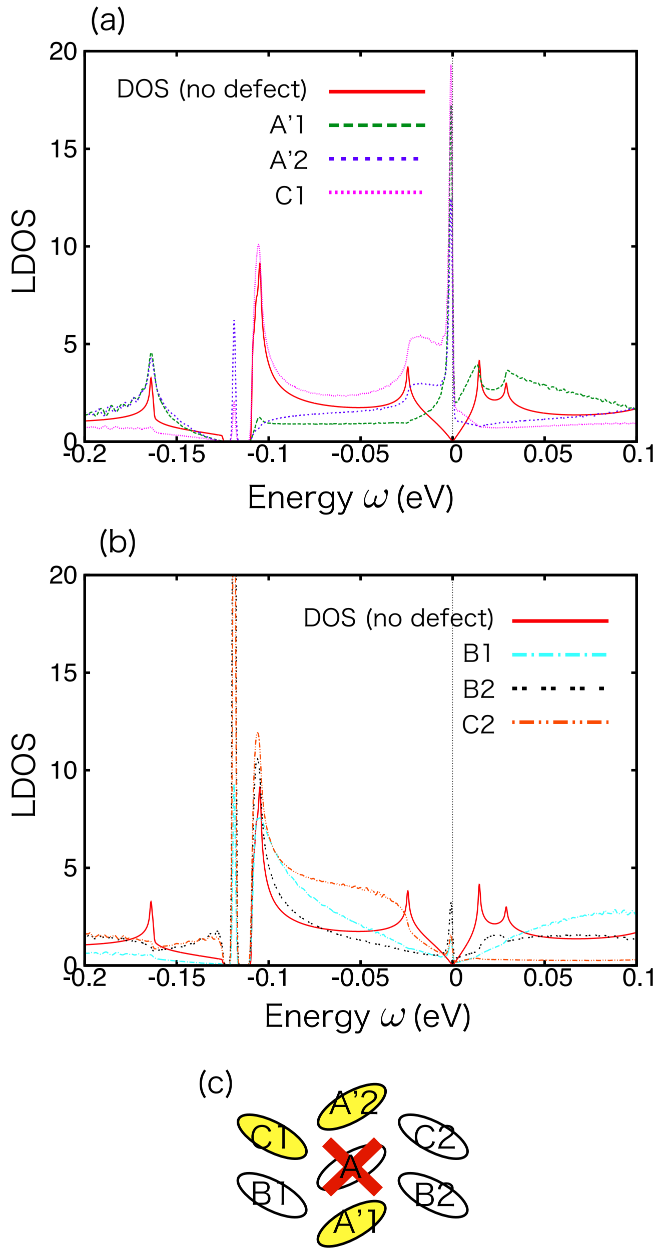

Figure 3.7: Energy dependence of local density of states (LDOS) at several sites around a defect at the site A. (a) The LDOS at the sites $A'1$, $A'2$, and $C1$ show a sharp peak at the energy of Dirac points ($\omega = 0$ eV). (b) The LDOS at the sites $B1$, $B2$, and $C2$ show a sharp peak in the band gap around $\omega = -0.1$ eV. (c) The defect site A, which is indicated by an X, and the sites around it, which are labeled by $A'1$, $A'2$, $B1$, $B2$, $C1$, and $C2$. The LDOS at the colored sites are shown in (a).

where ω, $\psi_{\boldsymbol{k}l}(\boldsymbol{r}_{i\alpha})$, $\epsilon_{\boldsymbol{k}l}$, and $N_{\rm SC}$ are the energy, the wave functions and the energy eigenvalues with wave vector $\boldsymbol{k}$, and the number of supercells, respectively. Figure 3.6 shows the real-space map of the LDOS for $\omega = 0$ eV with the defect at the site A. Here, the case with single supercell is shown. It is observed that the LDOS is enhanced in the vicinity of the defect, and it extends in about five unit cells, which is consistent with the localization length estimated from the IPR. It also shows an anisotropy. The anisotropy of the wave function is examined in the $\boldsymbol{k}$ space in §3.4.

The energy dependence of the LDOS in the vicinity of the defect placed at site A is shown in Fig. 3.7. Here, the system size is 4×35^2, and 9×9 supercells are used. The sites surrounding the defect site A are labeled as in Fig. 3.7(c). It is found that the LDOS on the sites $A'1$, $A'2$, and $C1$ [colored sites in Fig. 3.7(c)] exhibit sharp peaks at the energy of Dirac points as in Fig. 3.7(a), while those on the sites $B1$, $B2$, and $C2$ have peaks in the band gap around $\omega = -0.1$ eV as in Fig. 3.7(b). The LDOS in the case of defect at the site B or C are also calculated, (which are not shown) and it is found that LDOS is not induced at the energy of the Dirac points nor in the band gap, as is expected from the result of IPRs. From these result, it is indicated that the equivalent sites A and A' are important on the electronic states near the Dirac points.

3.4 Green's Function in the Presence of Single Defect

To obtain more information about this localized state, we consider the Green's function, which is derived exactly in this single on-site impurity case [99]. By using it, $\boldsymbol{k}$-space pictures are obtained without diagonalizing large matrices.

The retarded Green's function of the Hamiltonian $H = H_0 + H'$ is introduced as

$$(\omega^+ - H)G(\omega) = 1, \tag{3.9}$$

where ω is an energy and $\omega^+ = \omega + {\rm i}\eta$ with $\eta \to +0$. With a retarded Green's function without defect $G^0(\omega)$ which satisfies $(\omega^+ - H_0)G^0(\omega) = 1$, eq. (3.9) is transformed as

$$G(\omega) = G^0(\omega) + G^0(\omega)H'G(\omega), \tag{3.10}$$

since an operation of $\omega^+ - H_0$ on its both sides leads to $(\omega^+ - H_0)G(\omega) = 1 + H'G(\omega)$, and hence eq. (3.9) is reproduced. In the site representation $r = \boldsymbol{r}_{i\alpha}$ and $r' = \boldsymbol{r}_{j\beta}$, eq. (3.10) is expressed as

$$G(r, r'; \omega) = G^0(r, r'; \omega) + \sum_{ss'} G^0(r, s; \omega)H'(s, s')G(s', r'; \omega). \tag{3.11}$$

This equation holds for general scattering potential. When the scattering potential is localized at a single site r^*, then, $H'(s, s') = I\delta_{ss'}\delta_{sr^*}$, and eq. (3.11) becomes $G(r, r'; \omega) =$

$G^0(r, r'; \omega) + G^0(r, r^*; \omega) I G(r^*, r'; \omega)$. By solving this equation, the Green's function is obtained as

$$G(\boldsymbol{r}_{i\alpha}, \boldsymbol{r}_{j\beta}; \omega) = G^0(\boldsymbol{r}_{i\alpha}, \boldsymbol{r}_{j\beta}; \omega) + \frac{G^0(\boldsymbol{r}_{i\alpha}, \boldsymbol{r}_{i^*\alpha^*}; \omega) G^0(\boldsymbol{r}_{i^*\alpha^*}, \boldsymbol{r}_{j\beta}; \omega)}{1/I - G^0(\boldsymbol{r}_{i^*\alpha^*}, \boldsymbol{r}_{i^*\alpha^*}; \omega)}. \tag{3.12}$$

The position of the defect is the site α^* of unit cell i^*.

Because a pole of the Green's function corresponds to an energy eigenvalue, the energy eigenvalue of the state induced by the defect scattering is determined as the root ω of the equation [99]

$$\frac{1}{I} - G^0(\boldsymbol{r}_{i^*\alpha^*}, \boldsymbol{r}_{i^*\alpha^*}; \omega) = 0. \tag{3.13}$$

Being independent of i^*, $G^0(\boldsymbol{r}_{i^*\alpha^*}, \boldsymbol{r}_{i^*\alpha^*}; \omega)$ is calculated in the $\boldsymbol{k}$ space as

$$G^0(\boldsymbol{r}_{i^*\alpha^*}, \boldsymbol{r}_{i^*\alpha^*}; \omega) = \frac{1}{N_{\mathrm{uc}}} \sum_{\boldsymbol{k}} \sum_{m=1}^{4} \frac{|\phi^0_{\boldsymbol{k}m\alpha^*}|^2}{\omega - \epsilon^0_{\boldsymbol{k}m} + \mathrm{i}\eta}, \tag{3.14}$$

where N_{uc} is the number of unit cells. $\epsilon^0_{\boldsymbol{k}m}$ and $\phi^0_{\boldsymbol{k}m\alpha}$ are energy eigenvalues of band $m = 1, 2, 3,$ and 4 with wave vector $\boldsymbol{k}$ and the corresponding eigenvectors, respectively. Solutions of eq. (3.13) must satisfy $1/I - \mathrm{Re}G^0(\boldsymbol{r}_{i^*\alpha^*}, \boldsymbol{r}_{i^*\alpha^*}; \omega) = 0$ and $\mathrm{Im}G^0(\boldsymbol{r}_{i^*\alpha^*}, \boldsymbol{r}_{i^*\alpha^*}; \omega) = 0$ simultaneously. Since $-\mathrm{Im}G^0(\boldsymbol{r}_{i^*\alpha^*}, \boldsymbol{r}_{i^*\alpha^*}; \omega)$ is proportional to the sublattice α^* component of DOS $\rho_{\alpha^*}(\omega)$, the imaginary part of eq. (3.13) shows that a state induced by the defect scattering can appear only at the energy where the sublattice α^* component of DOS is zero.

Figure 3.8 shows $\mathrm{Re}G^0(\boldsymbol{r}_{i^*\alpha^*}, \boldsymbol{r}_{i^*\alpha^*}; \omega)$ and $-\pi\mathrm{Im}G^0(\boldsymbol{r}_{i^*\alpha^*}, \boldsymbol{r}_{i^*\alpha^*}; \omega)$ for site $\alpha^* = A, A', B,$ and C as a function of energy ω. When $|I| \to \infty$, the eigenvalue equation (3.13) has solutions only in the case of the defect at site $\alpha^* = A$ or A' [Fig. 3.8(a)], and these solutions are located at the energy of the Dirac points or in the band gap around -0.1 eV. This confirms the results obtained from the IPR and the LDOS in §3.3. From Fig. 3.8(a), it can be seen that scattering potential larger than $|I| \sim 1$ eV is sufficient to introduce a state at the energy of Dirac points. Here, it is also found that $G^0(\boldsymbol{r}_{i^*\alpha^*}, \boldsymbol{r}_{i^*\alpha^*}; \omega)$ for $\alpha^* = A$ or A' shows similar energy dependence at the energy of Dirac points and in the band gap as in Fig. 3.8(a). This implies that the origin of the localized state at the energy of Dirac points is similar to that of an ordinary localized state in a band gap. The difference is that a large scattering potential is needed to introduce a state at the energy of Dirac point while a small scattering potential is sufficient in the band gap. From Fig. 3.8(b) and (c), it is found that the eigenvalue equation (3.13) for $\alpha^* = B$ or C also has solutions at the energy of Dirac points when I is a positive value in a certain range. This means that the localized state can also appear when a certain positive scattering potential is at the sites B or C.

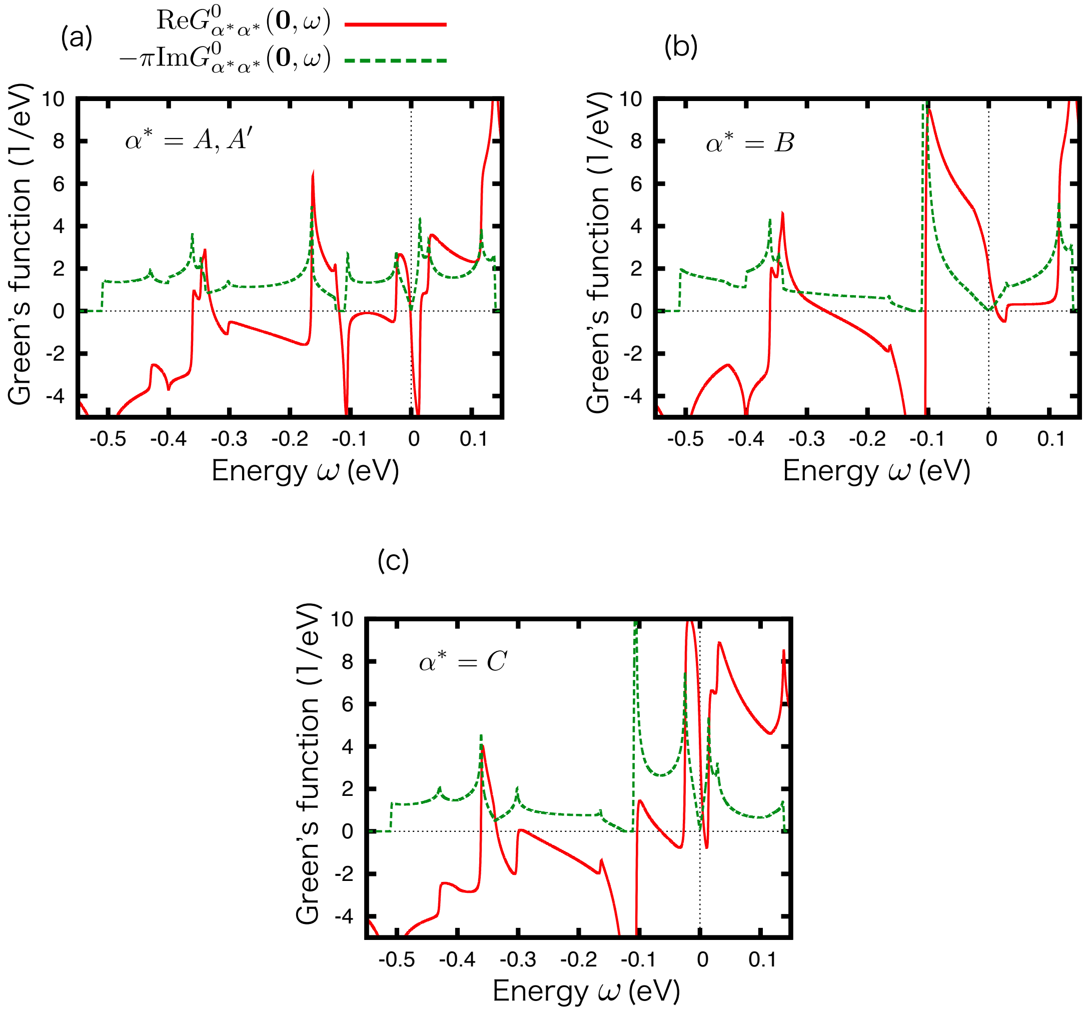

Figure 3.8: On-site components of retarded Green's function without defect, $\mathrm{Re}G^0(\boldsymbol{r}_{i^*\alpha^*}, \boldsymbol{r}_{i^*\alpha^*}; \omega)$ and $-\pi\mathrm{Im}G^0(\boldsymbol{r}_{i^*\alpha^*}, \boldsymbol{r}_{i^*\alpha^*}; \omega)$ as a function of energy ω. $-\mathrm{Im}G^0(\boldsymbol{r}_{i^*\alpha^*}, \boldsymbol{r}_{i^*\alpha^*}; \omega)$ is proportional to the sublattice α^* component of the density of states $\rho_{\alpha^*}(\omega)$. (a) Component of sublattice $\alpha^* = A$ or A'. (b) B. (c) C.

From the Green's function eq. (3.12), the wave function of the localized state induced by the defect is obtained as

$$\psi^d(\boldsymbol{r}_{i\alpha})\psi^{d*}(\boldsymbol{r}_{j\beta}) = \lim_{\omega\to\epsilon_d}(\omega-\epsilon_d)G(\boldsymbol{r}_{i\alpha},\boldsymbol{r}_{j\beta};\omega) \tag{3.15}$$

$$= N_{\alpha^*}(\epsilon_d)G^0(\boldsymbol{r}_{i\alpha},\boldsymbol{r}_{i^*\alpha^*};\epsilon_d)G^0(\boldsymbol{r}_{i^*\alpha^*},\boldsymbol{r}_{j\beta};\epsilon_d), \tag{3.16}$$

where ϵ_d is the energy eigenvalue of the state induced, and $N_{\alpha^*}(\epsilon_d)$ is the normalization coefficient [99]. Here, the localized state does not degenerate. By the Fourier transformation, the components with wave vector $\boldsymbol{k}$ is expressed as

$$\psi^d_{\boldsymbol{k}m}\psi^{d*}_{\boldsymbol{k}n} = N_{\alpha^*}(\epsilon_d)G^0_{\boldsymbol{k}m}(\epsilon_d)\phi^{0*}_{\boldsymbol{k}m\alpha^*}\phi^0_{\boldsymbol{k}n\alpha^*}G^0_{\boldsymbol{k}n}(\epsilon_d), \tag{3.17}$$

in the band representation, and

$$\psi^d_{\boldsymbol{k}\alpha}\psi^{d*}_{\boldsymbol{k}\beta} = N_{\alpha^*}(\epsilon_d)\sum_{m,n=1}^{4}\phi^0_{\boldsymbol{k}m\alpha}G^0_{\boldsymbol{k}m}(\epsilon_d)\phi^{0*}_{\boldsymbol{k}m\alpha^*}\phi^0_{\boldsymbol{k}n\alpha^*}G^0_{\boldsymbol{k}n}(\epsilon_d)\phi^{0*}_{\boldsymbol{k}n\beta}, \tag{3.18}$$

in the sublattice representation, where $G^0_{\boldsymbol{k}m}(\omega) = 1/(\omega + \mathrm{i}\eta - \epsilon^0_{\boldsymbol{k}m})$ is the band representation of the Green's function in the $\boldsymbol{k}$ space without defect.

Figures 3.9 show the band representations of the wave function in the $\boldsymbol{k}$ space $\psi^d_{\boldsymbol{k}m}\psi^{d*}_{\boldsymbol{k}n}$ when the defect is at the site A. Here, the lattice constants are set to be unity. The components of the bands $m, n = 1, 2$ are shown. These bands form the Dirac cones. Here, the band index is chosen so that $\epsilon_{\boldsymbol{k}m} > \epsilon_{\boldsymbol{k}m+1}$. The components of the other bands are zero. In each figure, two bright spots which are related with each other by the space inversion are found. These positions coincide with the Dirac points, which shows that the localized state consists of the $\boldsymbol{k}$ states around the Dirac points. Note that the two Dirac points equally contribute to the localized state. This is because the strongly localized scattering potential mixes all the $\boldsymbol{k}$ states, and the states near the both Dirac points are equally mixed when the induced state is at the energy of the Dirac points. At the Dirac points, the orders of the amplitudes are same for the bands $m = n = 1$, $m = n = 2$, and $m = 1$, $n = 2$, which shows that the localized state consists of both the electron and hole states near the Dirac points.

In Fig. 3.9, anisotropy around the Dirac points is found. This anisotropy is understood from the tilting of the Dirac cones shown in Fig. 3.2: Among the $\boldsymbol{k}$ states in the Dirac cones, the $\boldsymbol{k}$ states located in the direction with a moderate slope of the Dirac cone contribute more than the $\boldsymbol{k}$ states located in the direction with a sharp slope. This is due to the factor $\sim 1/\left(\epsilon^0_{\boldsymbol{k}m}\right)^2$ in eq. (3.17).

Figures 3.10 show the sublattice representations of the amplitudes of the wave functions $\left|\psi^d_{\boldsymbol{k}\alpha}\right|^2$. The amplitudes are also large near the Dirac points and show anisotropy around them, which comes from the tilting of the Dirac cones. These facts indicate that

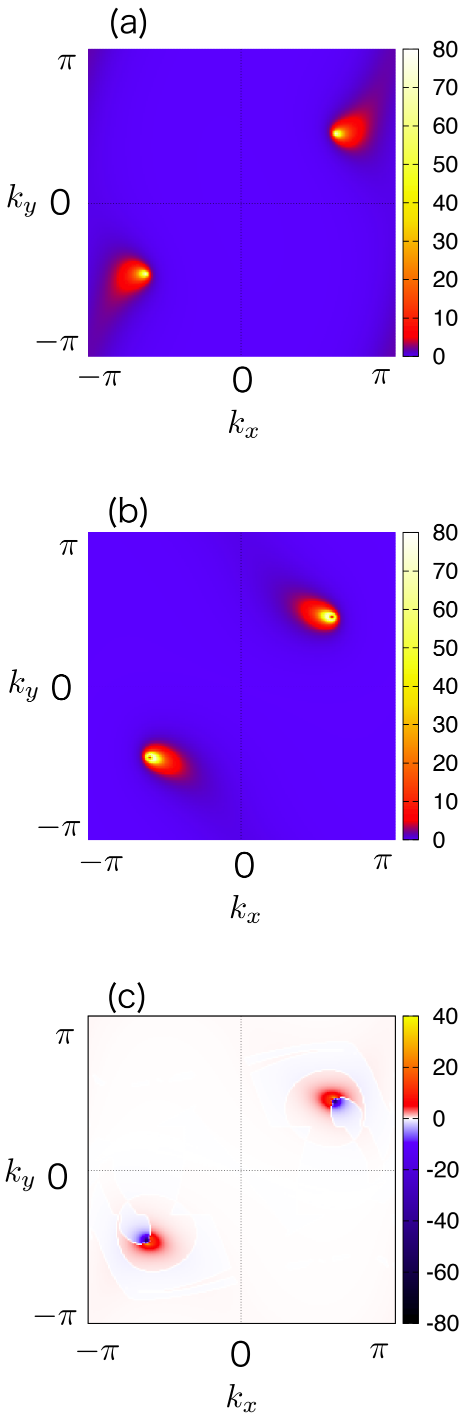

Figure 3.9: Band representations of the wave function of the localized state induced by the defect at site A, in the $\boldsymbol{k}$ space, $\psi^{d}_{\boldsymbol{k}m}\psi^{d*}_{\boldsymbol{k}n}$, for the band (a) $m = n = 1$, (b) $m = n = 2$, and (c) $m = 1, n = 2$, where $\epsilon_{\boldsymbol{k}1} > \epsilon_{\boldsymbol{k}2}$. In (c), the real part is shown. The direction of k_x and k_y axes are chosen to be that of $-b$ and a, respectively.

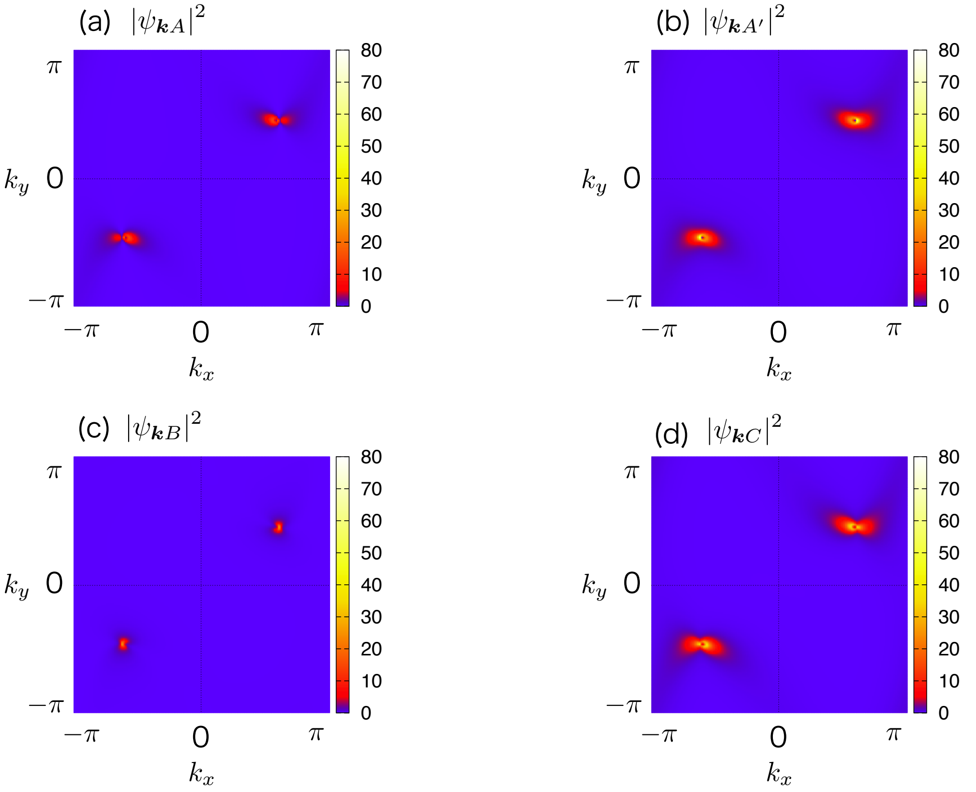

Figure 3.10: Sublattice representations of the wave function of the localized state induced by the defect at site A, in the $\boldsymbol{k}$ space, $\left|\psi^{d}_{\boldsymbol{k}\alpha}\right|^2$, for the sublattice (a) $\alpha = A$, (b) A', (c) B, and (d) C.

the anisotropy found in the real-space map of the LDOS shown in Fig. 3.6 originate from the tilting of the Dirac cones in α-(ET)$_2$I$_3$. In Figs. 3.6, 3.9, and 3.10, the directions of the axes are chosen to be the same.

A comparison of Figs. 3.10(a) and (b) shows that the sublattice A component is much smaller than that of A'. Here, the defect is at the site A. This behavior is similar to that of graphene, where the sublattice A component is zero when the defect is at the site A in the particle-hole symmetric case, and the state consists of only the sublattice B component [69, 70, 71]. A comparison of Figs. 3.10(c) and (d) shows that the sublattice C component is larger than that of B. This would be related to the difference of the sublattice components of DOS around the energy of the Dirac points, which is larger for C than B [100] as in Figs. 3.8(b) and (c). However, at the Dirac point, the value of the sublattice C is about half of that of A'. This indicates the importance of the sublattice A and A' degrees of freedom in this localized state.

3.5 Discussions

Here, we discuss the experimental detection of this localized state in α-(ET)$_2$I$_3$. If the defect of ET molecule at the site A or A' behaves as a strong scatterer ($|I| \sim 1$ eV or larger), the localized state will appear at the energy of the Dirac points. Or by a certain smaller positive scattering potential at the site B or C will cause similar state. We expect that not only the molecular vacancy but also a rotated molecule can act as a strong scatterer because the rotation of a molecule will suppress the transfer integrals into the molecule. Such a molecular rotation may occur more frequently than a molecular vacancy.

This state can be observed with microscopic measurements such as the STM and STS. A real-space map and local spectra obtained in STM and STS measurements will resemble Fig. 3.6 and Figs. 3.7, respectively. By examining anisotropy of the localized state in STM image, information on the tilting of the Dirac cones such as its direction in the conducting plane and the tilting angle can be obtained. Since this localized state consists of the Dirac fermions, other information on them such as the position of the Dirac cones in the Brillouin zone is obtained by transforming the STM image into the $\boldsymbol{k}$ space separately for each sublattice as in Fig. 3.10.

With finite density of such defects, the induced localized states can be also detected by bulk measurements such as NMR, by which spin susceptibility and nuclear spin-lattice relaxation rate can be measured. These states induce finite DOS at the energy of Dirac points, which coincides with the Fermi energy in this material if the 3/4 filling is fixed. The induced DOS causes an increase of the spin susceptibility compared with the case of no defect. Since the individual localized states have certain extension and enhance the DOS in the local regions, they will cause two nuclear spin-lattice relaxation rates, where one is from molecules near the defects and the other from those far away. Such two nuclear spin-lattice relaxation rates which originate from impurity states have been observed in d-wave superconductors [101].

Finally, we comment on the case that other Fermi surfaces exist in addition to the Dirac points. As shown in §3.4, when the defect is at the site α^*, a localized state can appear only at the energy where the sublattice α^* component of DOS is zero. Then, states other than those at the Dirac points prevent the appearance of the localized state. This fact can be used in judging whether other Fermi surfaces coexist: If the localized state at the energy of the Dirac points is observed at the defect by, for example, STM, then, only the Dirac fermions exist, and if not, other Fermi surfaces coexist.

3.6 Summary

The effects of defects on the electronic states of α-(BEDT-TTF)$_2$I$_3$ have been investigated by solving the realistic tight-binding Hamiltonian. The model will be valid as long as there are no charge or magnetic orders. By calculating the inverse participation ratio, we have found that a localized state at the energy of the Dirac points is induced by the defect at the site A or A', while the state is not induced by the defect at the site B, C, or I_3^-. This has also been confirmed by using the Green's function method. This localized state strongly enhances the LDOS in the vicinity of the defect. Using the Green's function method, we have evaluated the wave function of the localized state in the $\boldsymbol{k}$ space, and found that this localized state consists of the electron and hole states around the Dirac point, and shows anisotropy around the Dirac points, which reflects the tilting of the Dirac cones in α-(BEDT-TTF)$_2$I$_3$. This anisotropy leads to that in the real space. The sublattice components of the localized state are calculated. In the case of defect at the site A, the sublattice A' component is largest, and vice versa. These phenomena can be observed in experimental measurements such as the STM and STS or the NMR. In the case that other Fermi surfaces are present in addition to the Dirac fermions, the localized state will not be introduced, and this fact can be used in judging whether other Fermi surfaces coexist or not.

Chapter 4

Effects of Charge Fluctuations on Dirac Fermions in α-(BEDT-TTF)$_2$I$_3$

Motivated by anomalous behaviors such as the logarithmic increase of resistivity at low temperatures introduced in chapter 3, we study effects of charge fluctuations in the vicinity of charge-ordered phase of α-(ET)$_2$I$_3$ in this chapter. In §4.1, the properties of charge-ordered phase and neighboring Dirac fermion phase are reviewed. Anomalous behaviors in the Dirac fermion phase observed experimentally at low temperatures are described. As an origin of this anomalous behaviors, we investigate effects of charge fluctuations near the quantum critical point associated with the charge ordering. From a minimal model introduced in §4.2.1 which describes Dirac fermions in two dimensions and their charge ordering transition, a Landau-Ginzburg-Wilson functional is derived in §4.2.2. Here, the Fermi energy is fixed at the energy of the Dirac points. It is found that the charge fluctuations in Dirac fermions obey a characteristic dispersion which contains variables q and ω_l in a symmetric manner. By analyzing this functional with the perturbative renormalization group (PRG) method in §4.3.1 and with the self-consistent renormalization (SCR) theory in §4.3.2, it is shown that the effects of the mode-mode coupling between the fluctuations tend to be less effective in Dirac fermions compared with the case of conventional magnetic fluctuations in metals. In §4.4, the effects of charge fluctuations on physical quantities are investigated in the vicinity of the quantum critical point by using the SCR theory. It is shown that the interaction between the electrons and the charge fluctuations causes peaks in the electron self-energy as a function of temperature and energy ω when the mode-mode coupling is strong. These peaks lead to a non-monotonic temperature dependence of electric resistivity (or damping rate of electrons), and suppression of density of states. The specific heat of the charge fluctuations is also calculated. In §4.5, the results are summarized and the relevance to the experimental results is discussed.

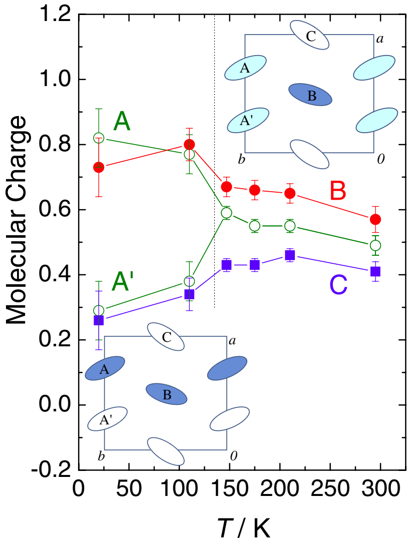

Figure 4.1: Temperature dependence of molecular charges for sublattices A, A', B, and C in α-(BEDT-TTF)$_2$I$_3$ at ambient pressure, measured in the X-ray diffraction experiment [103]. At the left bottom of the figure, the pattern of the charge ordering is shown (the horizontal pattern). At the right top of the figure, the pattern of the charge disproportionation in the normal phase is also shown. [Reprinted figure with permission from T. Kakiuchi *et al.*, J. Phys. Soc. Jpn. **76** (2007) 113702. Copyright (2007) by the Physical Society of Japan.]

4.1 Introduction

4.1.1 Charge Ordering in α-(BEDT-TTF)$_2$I$_3$

In α-(ET)$_2$I$_3$ under ambient pressure, a metal-insulator transition takes place at 135 K, where the resistivity exhibits a drastic increase as shown in Fig. 1.4(a). It has been shown that this metal-insulator transition is a charge ordering transition, as has been revealed by NMR [27, 102], Raman spectroscopy [28], and X-ray diffraction [103]. Generally, the charge ordering is caused by strong long-range electron-electron interaction [104, 105]. In the charge-ordered state, charge rich sites (atoms or molecules) and charge poor sites align regularly, and several ordering patterns are possible.

The pattern of charge ordering in α-(ET)$_2$I$_3$ has been observed directly in the X-ray diffraction experiment, and identified to be a horizontal pattern as shown in Fig. 4.1 [103], which had been predicted theoretically based on the mean field approximation [106]. In this pattern, the charge rich and poor sites align horizontally to the stacking columns of ET molecules. The symmetry between molecules A and A' is broken in this state. The unit cell with four sites is unchanged through the transition, which means that the ordering wave vector is zero: $\boldsymbol{q} = 0$.

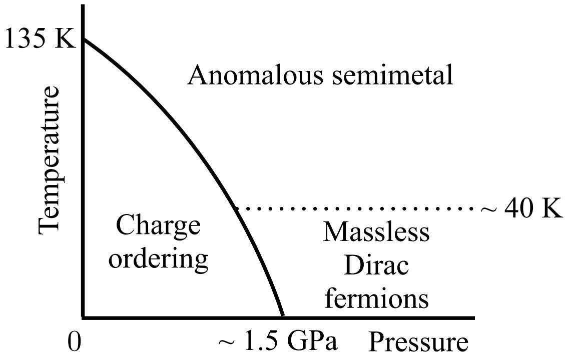

Figure 4.2: Schematic pressure-temperature phase diagram of α-(BEDT-TTF)$_2$I$_3$ [43]. The critical pressure $\sim$ 1.5 GPa and the characteristic temperature $\sim$ 40 K are shown.

At the charge ordering transition, the spin susceptibility abruptly drops and decreases exponentially toward zero temperature [107]. This indicates a non-magnetic ground state with a spin gap. The ground state of spin degrees of freedom in this charge-ordered state has been discussed theoretically, and a spin-singlet state due to alternating couplings between spins in the effective one-dimensional spin chains has been suggested [106]. This picture has been supported by a recent theoretical study with the variational Monte Carlo method which can deal with quantum fluctuations beyond the mean field approximation [108, 109].

The specific heat shows relatively small hysteresis at the transition [110], which is caused by small modulation of the lattice [103, 111]. This modulation is a small rotation of molecules rather than displacement. It is suggested that this modulation of lattice is a secondary effect of the electronic charge ordering, and that the main cause of the phase transition is the instability within the electronic degrees of freedom. Without the lattice modulation, a continuous transition is suggested from the variational Monte Carlo study [109].

By applying hydrostatic pressures, the transition temperature decreases, and above $\sim$1.5 GPa the transition is suppressed [Fig. 1.4(a)]. A pressure-temperature phase diagram based on the transport measurements is shown in Fig. 4.2 [43]. In the low-temperature region below 40 K and above the pressure of $\sim$1.5 GPa, the quantities such as carrier density are understood as a result of massless Dirac fermions. The high-temperature region is called (anomalous) semimetal because the Dirac dispersion is no longer valid in this temperature region. However, these two regions are connected without any phase transition. The important feature of this phase diagram is that the charge-ordered phase exists next to the Dirac fermion phase. This indicates that the charge ordering is formed by the Dirac fermions in α-(ET)$_2$I$_3$.

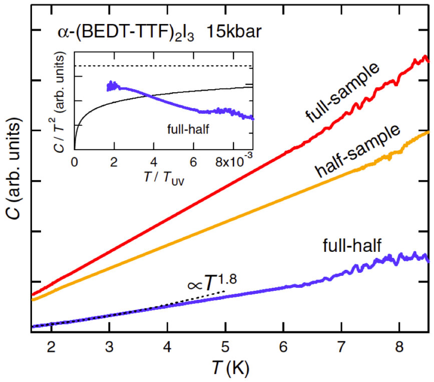

Figure 4.3: Temperature dependence of specific heat of α-(BEDT-TTF)$_2$I$_3$ under the pressure of 15 Kbar [40]. The inset shows the specific heat divided by T^2. [Reprinted figure with permission from T. Konoike, K. Uchida, and T. Osada, J. Phys. Soc. Jpn. **81** (2012) 043601. Copyright (2012) by the Physical Society of Japan.]

4.1.2 Anomalous Properties of Dirac Fermion Phase

Recently, the Dirac fermion phase of α-(ET)$_2$I$_3$ has been re-examined, and some behaviors beyond non-interacting clean Dirac fermions have been observed. In the massless Dirac fermion phase, temperature-independent resistivity is expected. However, it has been reported that the resistivity under the pressure of 1.8 GPa shows a logarithmic increase below $\sim$5 K as shown in Fig. 3.1 [92]. As the origin of this phenomenon, Anderson localization and Kondo effect have been argued in ref. [92], but distinct explanation has not been obtained yet.

The magnetic properties of the Dirac fermion phase has been examined in NMR experiments. The spin susceptibility and the nuclear spin-lattice relaxation rate $(T_1T)^{-1}$ have been reported [43]. At low temperatures, the spin susceptibility is suppressed compared with the prediction based on a non-interacting model [100]. This is regarded as suppression of the density of states caused by long-range electron-electron interaction introduced in chapter 1 [112]. The nuclear spin-lattice relaxation rate shows a deviation from expected T^2 dependence and an increase at the lowest temperatures. The origin of this increase has not been clarified. A specific heat measurement has also been reported as shown in Fig. 4.3 [40]. It shows a compatible behavior with expected T^2 dependence.

4.1.3 Charge Fluctuations in the vicinity of Charge Ordering

Generally, in the vicinity of a continuous phase transition, fluctuations associated with the order develop and they cause critical phenomena [113, 114]. These fluctuations are variations of the order parameter in space and time, consisting of thermal and quantum fluctuations. When the transition occurs at a finite temperature, the thermal fluctuations dominate. These are called classical critical phenomena. On the other hand, when the transition occurs near the zero temperature by changing parameters of the system, the quantum fluctuations become important. These are called quantum critical phenomena, and the point in the phase diagram where the zero temperature transition occurs is called a quantum critical point [115, 116].

The quantum critical phenomena associated with magnetic orders have been studied extensively [115, 116, 117]. Theory of classical critical phenomena has been generalized to deal with the quantum critical phenomena, and theoretical methods such as the perturbative renormalization group (PRG) method [115, 116] and the self-consistent renormalization (SCR) theory [117] have been developed. By these methods, it has been shown that the critical magnetic fluctuations can cause non-Fermi liquid temperature dependence of physical quantities. The enhanced magnetic fluctuations are also argued as an origin of effective electron-electron interactions which lead to superconductivity [118]. Recently, the quantum critical phenomena associated with valence fluctuations have also been discussed using the SCR theory [119].

Effects of the charge fluctuations in organic conductors in the vicinity of charge-ordered phase have been studied theoretically [105] and experimentally [120]. Several interesting states have been studied such as a metallic state caused by quantum melting of charge ordering with geometrical frustration [121, 122] and superconductivity mediated by charge fluctuations [123, 124]. Effects of the charge fluctuations on physical properties have also been explored. Non-Fermi liquid behaviors have been discussed based on the random phase approximation [125] and based on the finite temperature Lanczos diagonalization [126]. Enhancement of the Pauli paramagnetism [127], deformation of the Fermi surface [128], and instability toward inhomogeneous electronic states [129] have been discussed.

Since the Dirac fermion phase of α-(ET)$_2$I$_3$ is located next to the charge-ordered phase and the transition is almost continuos, charge fluctuations are expected to be important. Behaviors of the charge fluctuations in Dirac fermions at the Dirac point may be different from those in the conventional metals with Fermi surfaces which have been studied before. In the following, we study the effects of such critical charge fluctuations on the Dirac fermions by using a simple model. We use the PRG method and SCR theory to analyze the model and to calculate physical quantities.

4.2 Landau-Ginzburg-Wilson Functional for Dirac Fermions near Charge Ordering

4.2.1 Minimal Model for Dirac Fermions near Charge Ordering

The simplest lattice model which has Dirac fermions and in which charge ordering occurs with ordering wave vector $\boldsymbol{q} = 0$ is the extended Hubbard model on the honeycomb lattice [130, 131]. The interacting part of the extended Hubbard model consists of terms of on-site repulsive electron-electron interaction U and nearest-neighbor one V. By mean field approximations, it has been shown that a large value of V causes the charge ordering, while that of U causes a magnetic one [130, 131]. Here, we consider the case near the charge ordering and far from the magnetic one. In this case, the on-site interaction U will only cause corrections of one-body parameters, and the behavior of the charge fluctuations will be qualitatively the same as that in the case of $U = 0$. In the following, we consider the case of $U = 0$ as a minimal model.

The non-interacting part of the Hamiltonian H_0 is the same as that of graphene introduced in eq. (1.2) with $\mu = 0$. We assume that the sublattices A and A' in α-(ET)$_2$I$_3$ correspond to the sublattices A and B in the honeycomb lattice. Here, the sublattices of the honeycomb lattice are denoted by A and B. The interacting part of the Hamiltonian is introduced as

$$H_1 = V \sum_{\langle ij \rangle} n_{ia} n_{jb}, \tag{4.1}$$

where $V(> 0)$ is the nearest-neighbor repulsive electron-electron interaction, and n_{ia} (n_{jb}) is the number of electrons on the sublattice A (B) of the unit cell i (j): $n_{ia} = \sum_\sigma a^\dagger_{i\sigma} a_{i\sigma}$ and $n_{jb} = \sum_\sigma b^\dagger_{j\sigma} b_{j\sigma}$.

4.2.2 Derivation of Landau-Ginzburg-Wilson Functional

From the model introduced in §4.2.1, we derive a Landau-Ginzburg-Wilson functional which describes the charge fluctuations near the charge ordering, following the formalism based on functional integral representation [115, 116, 132]. The Landau-Ginzburg-Wilson functional is the basis for the PRG method and the SCR theory.

The partition function is expressed in a functional integral representation as

$$Z = \int \mathcal{D}\left(c^\dagger c\right) \exp\left[- \int_0^\beta \mathrm{d}\tau L(c^\dagger, c) \right], \tag{4.2}$$

$$L(c^\dagger, c) = \sum_{\boldsymbol{k}\sigma, s=A,B} c^\dagger_{\boldsymbol{k}\sigma s} \partial\tau c_{\boldsymbol{k}\sigma s} + H_0 + H_1, \tag{4.3}$$

where τ is an imaginary time and $\beta = 1/T$ is an inverse temperature. The subscript s denotes the sublattices A and B. H_1 can be represented as

$$H_1 = \frac{V}{4} \sum_{\langle ij \rangle} \Big[(n_{ia} + n_{jb})^2 - (n_{ia} - n_{jb})^2 \Big]. \tag{4.4}$$

In the charge ordering in α-(ET)$_2$I$_3$, the difference of electron density between the sublattices is important and $(n_{ia} + n_{jb})^2$ is thought of as a constant. Hence we neglect the term $(n_{ia} + n_{jb})^2$. Then, we decouple the interaction term by introducing a bosonic Stratonovich-Hubbard field φ_i: $-(n_{ia} - n_{jb})^2 + (\varphi_i + n_{ia} - n_{jb})^2 = \varphi_i^2 + 2\varphi_i(n_{ia} - n_{jb})$ [133]. φ_i can be considered to be the field which represents the charge fluctuations. In the Fourier representation, H_1 becomes

$$H_1 = \frac{v(0)}{2} \sum_{\boldsymbol{q}} \varphi_{\boldsymbol{q}} \varphi_{-\boldsymbol{q}} + \frac{1}{\sqrt{N}} \sum_{\boldsymbol{q}} \left[v(0) \rho_{\boldsymbol{q}a} - v(-\boldsymbol{q}) \rho_{\boldsymbol{q}b} \right] \varphi_{-\boldsymbol{q}}, \tag{4.5}$$

where

$$v(\boldsymbol{q}) = \frac{V}{2} \sum_{\boldsymbol{\delta}} \mathrm{e}^{-\mathrm{i}\boldsymbol{q}\cdot\boldsymbol{\delta}}, \tag{4.6}$$

$$\rho_{\boldsymbol{q}s} = \sum_{\boldsymbol{k}\sigma} c^{\dagger}_{\boldsymbol{k}\sigma s} c_{\boldsymbol{k}+\boldsymbol{q}\sigma s}. \tag{4.7}$$

N is the number of unit cells, and $\boldsymbol{\delta}$ is the vector connecting the nearest-neighbor sites.

After $c^{\dagger}$ and c are integrated out, the partition function is expanded in terms of H_1 by fourth order using the method of many-particle physics [132]. This expansion leads to a Landau-Ginzburg-Wilson functional which is generalized to include quantum fluctuations,

$$Z = \int \mathcal{D}\varphi \mathrm{e}^{-S}, \tag{4.8}$$

$$\begin{aligned} S = {} & \frac{1}{2} \sum_{q} \Pi_2(q) \varphi_q \varphi_{-q} + \frac{1}{3} \sum_{q_1 q_2 q_3} \Pi_3(q_1 q_2 q_3) \varphi_{q_1} \varphi_{q_2} \varphi_{q_3} \delta_{q_1+q_2+q_3,0} \\ & + \frac{1}{4} \sum_{q_1 q_2 q_3 q_4} \Pi_4(q_1 q_2 q_3 q_4) \varphi_{q_1} \varphi_{q_2} \varphi_{q_3} \varphi_{q_4} \delta_{q_1+q_2+q_3+q_4,0}, \end{aligned} \tag{4.9}$$

where $q = (\boldsymbol{q}, i\omega_l)$, and ω_l is a bosonic Matsubara frequency. The first order term vanishes. By introducing a non-interacting sublattice susceptibility,

$$\chi^0_{ss'}(\boldsymbol{q}, i\omega_l) = -\frac{T}{N} \sum_{\boldsymbol{k}\omega_m} G^0_{\boldsymbol{k}+\boldsymbol{q}ss'}(i\omega_m + i\omega_l) G^0_{\boldsymbol{k}s's}(i\omega_m), \tag{4.10}$$

where $G^0_{\boldsymbol{k}ss'}(i\omega_m)$ is a sublattice representation of the non-interacting Green's function and ω_m is a fermionic Matsubara frequency, the second order term is calculated as

$$\Pi_2(q) = v(0) - 2\Big\{ \Big[v^2(0) + |v(\boldsymbol{q})|^2\Big]\chi^0_{aa}(q) - v(0)\Big[v(\boldsymbol{q})\chi^0_{ab}(q) + v^*(\boldsymbol{q})\chi^0_{ba}(q)\Big]\Big\} \tag{4.11}$$

$$\simeq v(0)\Big[1 - 2v(0)\chi^0_c(q)\Big], \tag{4.12}$$

$$\chi^0_c(q) = 2\chi^0_{aa}(q) - \chi^0_{ab}(q) - \chi^0_{ba}(q). \tag{4.13}$$

Here, $v(\boldsymbol{q})$ is approximated by $v(0)$, as the fluctuation of $\boldsymbol{q} = 0$ is most important and the $\boldsymbol{q}$ dependence of $v(\boldsymbol{q})$ around $\boldsymbol{q} = 0$ is weaker than that of $\chi^0_{ss'}(q)$, and a non-interacting susceptibility $\chi^0_c(q)$ is introduced. Π_3 and Π_4 are also approximated by the value at $\boldsymbol{q} = 0$:

$$\Pi_3(000) = 0, \tag{4.14}$$

$$\Pi_4(0000) = \frac{4v^4(0)}{(N\beta)^2}\sum_{k}\Big[\big(G^0_{kaa}\big)^2 - G^0_{kab}G^0_{kba}\Big]^2. \tag{4.15}$$

The latter is always positive. Until this point, the formalism is rather general. The characteristic features of the Dirac fermions appear in the following.

The non-interacting susceptibility eq. (4.13) can be explicitly calculated when the band structure is approximated by the linear dispersion. Similar quantities have been calculated in ref. [134], and we calculate $\chi^0_c(q)$ following the method in ref. [134].

By using the energy eigenvalues and the wave functions introduced in chapter 1, eq. (1.4) and (1.5), $\chi^0_c(q)$ is expressed as

$$\chi^0_c(\boldsymbol{q}, i\omega_l) = \frac{1}{2N}\sum_{\boldsymbol{k}n,n'=\pm1}\Big[1 - nn'\cos\left(\arg\phi_{\boldsymbol{k}+\boldsymbol{q}} - \arg\phi_{\boldsymbol{k}}\right)\Big]\frac{f(\epsilon_{\boldsymbol{k}+\boldsymbol{q}n}) - f(\epsilon_{\boldsymbol{k}n'})}{i\omega_l - \epsilon_{\boldsymbol{k}+\boldsymbol{q}n} + \epsilon_{\boldsymbol{k}n'}}, \tag{4.16}$$

where $f(\epsilon) = 1/\left(e^{\epsilon/T} + 1\right)$. At $T = 0$ (and $\mu = 0$), only interband processes $n \neq n'$ contribute, and eq. (4.16) becomes

$$\chi^0_c(\boldsymbol{q}, i\omega_l) = \frac{1}{2N}\sum_{\boldsymbol{k}}\Big[1 + \cos\left(\arg\phi_{\boldsymbol{k}+\boldsymbol{q}} - \arg\phi_{\boldsymbol{k}}\right)\Big] \times \left[\frac{-1}{i\omega_l - |\phi_{\boldsymbol{k}+\boldsymbol{q}}| - |\phi_{\boldsymbol{k}}|} + \frac{1}{i\omega_l + |\phi_{\boldsymbol{k}+\boldsymbol{q}}| + |\phi_{\boldsymbol{k}}|}\right]. \tag{4.17}$$

Then, $\phi_{\boldsymbol{k}}$ is approximated by the form around the Dirac points as $\phi_{\boldsymbol{K}(\boldsymbol{K}')+\boldsymbol{k}} \simeq v(\pm k_x - \mathrm{i}k_y)$ and $\arg\phi_{\boldsymbol{K}(\boldsymbol{K}')+\boldsymbol{k}} \simeq \mp\theta_{\boldsymbol{k}} (= \mp\tan^{-1} k_y/k_x)$, which gives

$$\chi^0_c(\boldsymbol{q}, i\omega_l) \simeq \frac{1}{N}\sum_{\boldsymbol{k}}\Big[1 + \cos\left(\theta_{\boldsymbol{k}+\boldsymbol{q}} - \theta_{\boldsymbol{k}}\right)\Big] \times \left[\frac{-1}{i\omega_l - v|\boldsymbol{k}+\boldsymbol{q}| - v|\boldsymbol{k}|} + \frac{1}{i\omega_l + v|\boldsymbol{k}+\boldsymbol{q}| + v|\boldsymbol{k}|}\right]. \tag{4.18}$$

The two Dirac points contribute identically. By analytic continuation of $i\omega_l \to \omega + i\eta$ with $\eta \to +0$ and by using $1/(x+i\eta) = \mathcal{P}/x - i\pi\delta(x)$ with $\mathcal{P}$ and $\delta(x)$ being the principal integration and the Dirac delta function, respectively, the imaginary part of the retarded susceptibility can be calculated as

$$\begin{aligned}\mathrm{Im}\chi_c^{0R}(\boldsymbol{q},\omega) &= \mathrm{Im}\chi_c^{0}(\boldsymbol{q},\omega+i\eta) &(4.19)\\ &= \frac{a^2}{4v^2}\mathrm{sgn}(\omega)\sqrt{\omega^2-(vq)^2}\theta(|\omega|-vq)\theta(2D-|\omega|), &(4.20)\end{aligned}$$

where a is a lattice constant, and a cutoff energy D is introduced. $\theta(x)$ is the Heaviside step function. The real part can be obtained by the Kramers-Kronig relation:

$$\begin{aligned}\mathrm{Re}\chi_c^{0R}(\boldsymbol{q},\omega) &= -\frac{1}{\pi}\int_{-\infty}^{\infty}\mathrm{d}\epsilon\,\mathrm{Im}\chi_c^{0R}(\boldsymbol{q},\epsilon)\mathcal{P}\frac{1}{\omega-\epsilon} &(4.21)\\ &\simeq \frac{a^2}{2\pi v^2}\left[2D-\frac{\pi}{2}\sqrt{(vq)^2-\omega^2}\theta(vq-|\omega|)\right], &(4.22)\end{aligned}$$

where terms of higher order in $1/D$ is neglected. From them, $\chi_c^0(\boldsymbol{q},i\omega_l)$ is deduced as

$$\chi_c^0(\boldsymbol{q},i\omega_l) = \frac{a^2}{2\pi v^2}\left[2D-\frac{\pi}{2}\sqrt{(vq)^2+\omega_l^2}\right]. \tag{4.23}$$

The coefficients and the signs can be confirmed by directly calculating the case of $q = 0$ or $\omega_l = 0$ from eq. (4.18). The temperature dependence of $\chi_c^0(0,0)$ is calculated from eq. (4.16) as

$$\begin{aligned}\chi_c^0(0,0) &= \frac{a^2}{\pi v^2}\left[D-2T\log 2+2T\log\left(1+\mathrm{e}^{-D/T}\right)\right] &(4.24)\\ &\simeq \frac{a^2}{\pi v^2}\left[D-2T\log 2\right] \quad (T/D \ll 1), &(4.25)\end{aligned}$$

which depends on T linearly at low temperatures.

From eqs. (4.12) and (4.23), $\Pi_2(q)$ under the linear dispersion approximation is obtained as

$$\Pi_2(\boldsymbol{q},i\omega_l) = \delta_0 + A\sqrt{(vq)^2+\omega_l^2}, \tag{4.26}$$

where

$$\delta_0 = v(0)\left[1-2v(0)\chi_c^0(0)\right], \tag{4.27}$$

and $A = a^2v^2(0)/2v^2$ are introduced. From eqs. (4.14), (4.15), and (4.26), the Landau-Ginzburg-Wilson functional eq. (4.9) is expressed as

$$\begin{aligned}S = &\frac{1}{2}\sum_{\boldsymbol{q}\omega_l}\left[\delta_0 + A\sqrt{(vq)^2+\omega_l^2}\right]\varphi_q\varphi_{-q}\\ &+\frac{g}{4}\frac{T}{N}\sum_{q_1,q_2,q_3,q_4}\varphi_{q_1}\varphi_{q_2}\varphi_{q_3}\varphi_{q_4}\delta_{q_1+q_2+q_3+q_4,0}, \end{aligned}\tag{4.28}$$

where $g = N\beta\Pi_4(0000) > 0$. δ_0 measures the distance from the transition point determined by the mean field approximation. $\delta_0 < 0$ and $\delta_0 > 0$ correspond to the ordered phase and the normal phase, respectively. The quadratic term represents the dispersion and the dynamics of charge fluctuations, which is called a Gaussian term. The fourth order term couples these individual fluctuation modes with each other, which is called a mode-mode coupling. g is the coupling constant. In the case of $g = 0$, this functional describes the free bosons and the problem is solved by the Gaussian integration. In the case of $g \neq 0$, exact integration is no longer possible and, some approximation methods are necessary to deal with the coupling term precisely. In this purpose, the PRG method and the SCR theory have been developed.

The important feature of the functional eq. (4.28) is that $\boldsymbol{q}$ and ω_l are included in a symmetric manner, which is "Lorentz invariant" [46]. This contrasts to asymmetric forms which appear in conventional cases of metals near magnetic ordering: In these cases, $\Pi_2^{\mathrm{conv}}(\boldsymbol{q}, i\omega_l)$ behaves as

$$\Pi_2^{\mathrm{conv}}(\boldsymbol{q}, i\omega_l) \simeq \delta_0 + Aq^2 + \frac{|\omega_l|}{\Gamma_q}, \tag{4.29}$$

near an ordering wave vector, with $\Gamma_q \propto q$ (ferromagnetic case) [115] or $\Gamma_q \propto$ const. (antiferromagnetic case) [116].

4.3 Analysis of the Landau-Ginzburg-Wilson Functional

4.3.1 Perturbative Renormalization Group Analysis

Here, we clarify the relevance of the mode-mode coupling term to low-energy behaviors of the present model by applying the PRG method [115, 116, 132]. A set of renormalization group equations for the parameters in the Landau-Ginzburg-Wilson functional is derived by the following steps.

1. Integrating out high-energy fluctuation modes
   By introducing a renormalization scale parameter b which satisfies $b > 1$ and $b - 1 \ll 1$, high-energy fluctuation modes with $\Lambda/b < q < \Lambda$ and $D/b < \epsilon < D$ are integrated out, where Λ is a cutoff momentum. In this step, the partition function is expanded perturbatively with the coupling term.

2. Rescaling of q and ω_l
   To recover the original integral region, the integral variables are rescaled as $q = q'/b$ and $\omega_l = \omega_l'/b^z$, where a dynamical exponent z is introduced. The rescaling of ω_l corresponds to a rescaling of the temperature $T = T'/b^z$.

3. Rescaling of δ and φ_q
   The dynamical exponent z and the rescaling of other variables are chosen so that the Gaussian term is invariant under this transformation. Here, $z = 1$, $\delta = \delta'/b$, and $\varphi_q = \varphi'_{q'} b^{(d+z+1)/2}$ satisfy this condition. δ denotes the renormalized δ_0. d is the spacial dimension of the system. Here, $d = 2$.

4. Renormalization group equations
   A comparison of the functional before and after the transformation yields the renormalization group equations for the parameters.

In the present case, we obtain the following equations which is valid for small $g(b)$:

$$\frac{\mathrm{d}\delta(b)}{\mathrm{d}\ln b} = \delta(b) + 3g(b)f_2(T(b), \delta(b)), \tag{4.30}$$

$$\frac{\mathrm{d}g(b)}{\mathrm{d}\ln b} = (2 - d - z)g(b) - 9g^2(b)f_4(T(b), \delta(b)), \tag{4.31}$$

$$\frac{\mathrm{d}T(b)}{\mathrm{d}\ln b} = zT(b), \tag{4.32}$$

where $f_2(T, \delta)$ and $f_4(T, \delta)$ are integrals with the explicit forms of

$$f_2(T, \delta) = \frac{D}{\pi} \coth \frac{D}{2T} \int_0^\Lambda \frac{\mathrm{d}^d q}{(2\pi)^d} \frac{A\sqrt{D^2 - (vq)^2}}{\delta^2 + A^2\left(D^2 - (vq)^2\right)}, \tag{4.33}$$

$$f_4(T, \delta) = \frac{D}{\pi} \coth \frac{D}{2T} \int_0^\Lambda \frac{\mathrm{d}^d q}{(2\pi)^d} \frac{2\delta A\sqrt{D^2 - (vq)^2}}{\left[\delta^2 + A^2\left(D^2 - (vq)^2\right)\right]^2}. \tag{4.34}$$

By solving these renormalization group equations, the low-energy behaviors of the system can be deduced. Equation (4.31) shows that in the present system, where $d+z = 3 > 2$, $g(b)$ becomes small for large b, that is, g is irrelevant and the upper critical dimension is $d+z = 2$. This implies that the low-energy behaviors are described effectively by a renormalized Gaussian model. Higher order terms also become small when they are renormalized. This is the main result which we deduce from the present renormalization group analysis, although it is possible to proceed further to extract other results from these equations.

Here, we make a remark on the upper critical dimension $d + z = 2$. In the case of metals near magnetic ordering, it has been known that the upper critical dimension is $d + z = 4$. This difference originates from the powers of q in Π_2: It behaves as $\sim q$ in the present system [eq. (4.26)], while $\sim q^2$ in the metals near magnetic ordering [eq. (4.29)]. The upper critical dimension $d + z = 2$ is a characteristic feature of charge fluctuations in Dirac fermions in two dimensions. The smaller value of the upper critical dimension means that the effects of mode-mode coupling is weaker in the present system than in conventional cases in metals.

4.3.2 Self-Consistent Renormalization Theory

To calculate physical quantities on the basis of the Landau-Ginzburg-Wilson functional eq. (4.28), we apply the SCR theory [117]. One way of formulating the SCR theory is to approximate the functional eq. (4.28) by the best Gaussian model using a variational principle [132]. The Gaussian approximation is in accordance with the result obtained by the PRG analysis in §4.3.1. The validity of this approximation is also discussed within the SCR framework in the following.

For a general trial functional S_{eff} including a variational parameter, the Feynman's inequality on free energy holds as $F \leq F_{\text{eff}} + T\langle S - S_{\text{eff}}\rangle_{\text{eff}} = \tilde{F}$, where F and $\tilde{F}$ are the exact free energy and the free energy calculated from S_{eff}, respectively. The variational parameter is determined by minimizing $\tilde{F}$, which gives the best functional within the introduced approximation.

In the SCR theory, the effective functional is assumed to be

$$S_{\text{eff}} = \frac{1}{2}\sum_{\boldsymbol{q}\omega_l}\left[\delta + A\sqrt{(vq)^2+\omega_l^2}\right]\varphi_q\varphi_{-q}, \tag{4.35}$$

where δ is regarded as a variational parameter. F_{eff} and $\langle S - S_{\text{eff}}\rangle_{\text{eff}}$ can be calculated by using the Gaussian integration as

$$F_{\text{eff}} = \frac{T}{2}\sum_{\boldsymbol{q}\omega_l}\ln D^{-1}(q) + \text{const.}, \tag{4.36}$$

$$\langle S - S_{\text{eff}}\rangle_{\text{eff}} = \frac{1}{2}(\delta_0 - \delta)\sum_{\boldsymbol{q}\omega_l}D(q) + \frac{3g}{4}\frac{T}{N}\left[\sum_{\boldsymbol{q}\omega_l}D(q)\right]^2, \tag{4.37}$$

where

$$D(\boldsymbol{q}, i\omega_l) = \langle\varphi_q\varphi_{-q}\rangle_{\text{eff}} = \frac{1}{\delta + A\sqrt{(vq)^2+\omega_l^2}}, \tag{4.38}$$

is the amplitude of the fluctuation with $\boldsymbol{q}$ and ω_l. The minimization condition $\partial\tilde{F}(\delta)/\partial\delta = 0$ gives a self-consistent equation,

$$\delta = \delta_0 + 3g\frac{T}{N}\sum_{\boldsymbol{q}\omega_l}D(q). \tag{4.39}$$

Since $\delta = 0$ determines the transition point, this equation means that the transition point is modified by the fluctuations which are coupled with each other by g. By this term, the temperature dependence of δ is modified from that of δ_0, and it leads to non-trivial temperature dependence of physical quantities. The self-consistent equation (4.39) can also be derived from a mean field approximation by decoupling the coupling term as

$$\sum_{q_1,q_2,q_3,q_4}\varphi_{q_1}\varphi_{q_2}\varphi_{q_3}\varphi_{q_4}\delta_{q_1+q_2+q_3+q_4,0} \to 6\sum_{q,q'}\langle\varphi_{q'}\varphi_{-q'}\rangle_{\text{eff}}\varphi_q\varphi_{-q}. \tag{4.40}$$

The approximation introduced above is self-consistent if $\langle S - S_{\rm eff}\rangle_{\rm eff}/\langle S_{\rm eff}\rangle_{\rm eff}$ is small. Using eq. (4.39), this quantity can be estimated as

$$\left|\frac{\langle S - S_{\rm eff}\rangle_{\rm eff}}{\langle S_{\rm eff}\rangle_{\rm eff}}\right| \sim \frac{g}{D}\left[\frac{T}{N}\sum_{\boldsymbol{q}\omega_l} D(q)\right]^2 . \tag{4.41}$$

At the critical point, where the fluctuations develop with $\delta \to 0$, the right hand side of eq. (4.41) can become large. Here, we extract the δ dependence of $(T/N)\sum_{\boldsymbol{q}\omega_l} D(q)$ for small δ. The Matsubara summation can be transformed into an integration over an energy variable ϵ by a method of contour integration. By taking two blanch cuts of $\sqrt{(vq)^2 - z^2}$ on the real axis with $|\epsilon| > vq$, the summation becomes

$$\frac{T}{N}\sum_{\boldsymbol{q}\omega_l} D(q) = \frac{1}{A}\int_0^{\Lambda} \frac{a^d \mathrm{d}^d q}{(2\pi)^d}\int_{vq}^{D} \frac{\mathrm{d}\epsilon}{\pi}\coth\frac{\epsilon}{2T}\frac{\sqrt{\epsilon^2-(vq)^2}}{(\delta/A)^2+\epsilon^2-(vq)^2} \tag{4.42}$$

$$\begin{aligned} &= \frac{1}{A}\int_0^{\Lambda} \frac{a^d \mathrm{d}^d q}{(2\pi)^d}\int_{vq}^{D} \frac{\mathrm{d}\epsilon}{\pi}\coth\frac{\epsilon}{2T}\frac{1}{\sqrt{\epsilon^2-(vq)^2}} \\ &+\frac{1}{A}\int_0^{\Lambda} \frac{a^d \mathrm{d}^d q}{(2\pi)^d}\int_{vq}^{D} \frac{\mathrm{d}\epsilon}{\pi}\coth\frac{\epsilon}{2T}\frac{-(\delta/A)^2}{\sqrt{\epsilon^2-(vq)^2}\,[(\delta/A)^2+\epsilon^2-(vq)^2]}, \end{aligned} \tag{4.43}$$

where the δ dependent part is separated since we are interested in the singularity caused by $\delta \to 0$. By changing the integral variables as $\epsilon = (\delta/A)^z x$ $(z = 1)$ and $vq = (\delta/A)y$, the δ dependent part leads to

$$\frac{T}{N}\sum_{\boldsymbol{q}\omega_l} D(q) \sim -\frac{1}{A}\left(\frac{\delta}{A}\right)^{d+z-2}\int_0^{\infty}\frac{a^d \mathrm{d}^d y}{(2\pi v)^d}\int_y^{\infty}\frac{\mathrm{d}x}{\pi}\frac{2T}{x}\frac{1}{\sqrt{x^2-y^2}\,(1+x^2-y^2)}, \tag{4.44}$$

where the upper limits of integrals are extended to infinity since the integrals are convergent, and an approximation of $\cosh \delta x/2AT \simeq 2AT/\delta x$ is made. This shows that δ dependence for small δ is not singular when $d + z > 2$, and the present approximation is valid. This corresponds to the result obtained by the PRG analysis in §4.3.1.

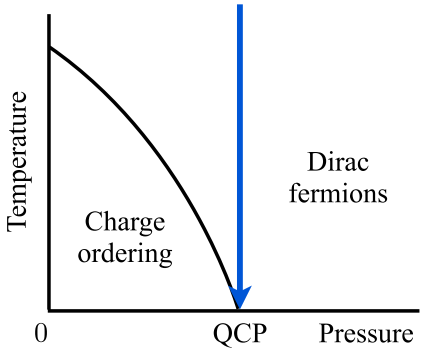

Figure 4.4: Schematic pressure-temperature phase diagram of α-(BEDT-TTF)$_2$I$_3$ based on ref. [43] and the path along which we calculate temperature dependence of physical quantities. The arrow above the QCP (quantum critical point) represents the path.

4.4 Effects of Charge Fluctuations on Physical Quantities

4.4.1 Solution of the Self-Consistent Equation

After the $\boldsymbol{q}$ integrations, the self-consistent equation (4.39) is expressed as

$$\eta = \eta_0 + u \int_0^1 \mathrm{d}x \coth \frac{x}{2t} \left(x - \eta \tan^{-1} \frac{x}{\eta} \right) \tag{4.45}$$

$$\begin{aligned} &= \eta_0 + u \int_0^1 \mathrm{d}x \frac{2}{\mathrm{e}^{x/t} - 1} \left(x - \eta \tan^{-1} \frac{x}{\eta} \right) \\ &\quad + u \left[\frac{1}{2} - \eta \tan^{-1} \frac{1}{\eta} + \frac{\eta^2}{2} \log \left(\frac{1}{\eta^2} + 1 \right) \right], \end{aligned} \tag{4.46}$$

where $\eta = \delta/AD$ and $\eta_0 = \delta_0/AD$ are dimensionless parameters, and $u = 3ga^2D/2\pi^2v^2A^2$ and $t = T/D$ are dimensionless mode-mode coupling and temperature, respectively. The second term in eq. (4.46) depends on the temperature through the Bose distribution function $1/\left(\mathrm{e}^{x/t} - 1\right)$, and hence represents the contribution from the thermal fluctuations. The third term represents that from the quantum fluctuations (or zero-point motions). The parameters η_0 and u depend on the unrenormalized Hamiltonian. In the following, we regard them as parameters determined in comparison with experiments.

We calculate the temperature dependence of parameter η near the quantum critical point, where the effects of charge fluctuations become most significant. The corresponding path in the pressure-temperature phase diagram is schematically shown in Fig. 4.4. The quantum critical point is specified by $\eta = 0$ at $t = 0$. At this point, eq. (4.46) becomes $0 = \eta_0(t = 0) + u/2$. Subtracting this from the both sides of eq. (4.46) at finite t, the

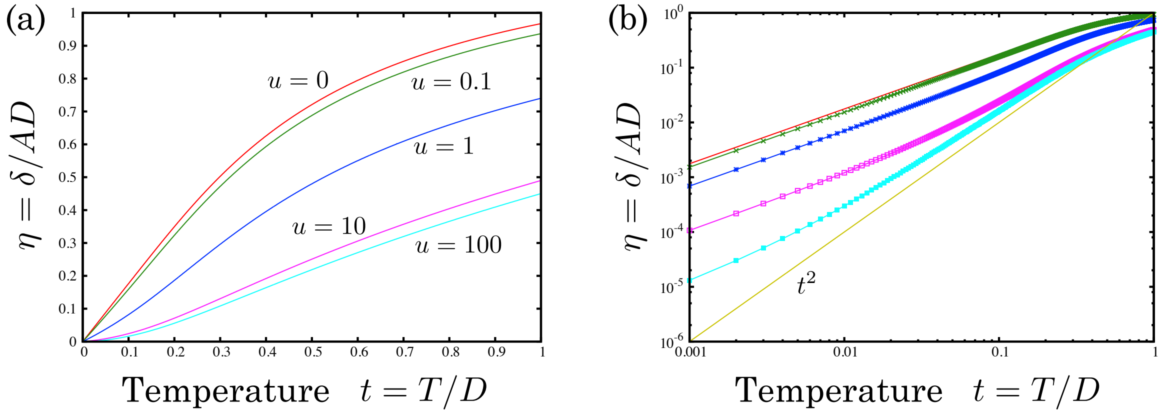

Figure 4.5: Temperature dependences of the parameter $\eta = \delta/AD$ near the quantum critical point for several values of mode-mode coupling parameter $u = 3ga^2D/2\pi^2v^2A^2$. (a) In the linear scale. (b) In the logarithmic scale for the same parameters. A line of t^2 dependence is also shown.

self-consistent equation is expressed as

$$\eta = \eta_0(t) - \eta_0(0) + u\int_0^1 \mathrm{d}x \frac{2}{\mathrm{e}^{x/t}-1}\left(x - \eta\tan^{-1}\frac{x}{\eta}\right)$$
$$+u\left[-\eta\tan^{-1}\frac{1}{\eta} + \frac{\eta^2}{2}\log\left(\frac{1}{\eta^2}+1\right)\right], \tag{4.47}$$

where from eq. (4.24) and (4.27)

$$\eta_0(t) - \eta_0(0) = \frac{8}{\pi}t\log\frac{2}{1+\mathrm{e}^{-1/t}}. \tag{4.48}$$

Figures 4.5 show the temperature dependences of η near the quantum critical point for several values of u, obtained by solving eq. (4.47) numerically. As shown in Fig. 4.5(a), η decreases as u increases. Since a small η corresponds to a sharp peak of $D(q)$ around $q = 0$, this result shows that the mode-mode coupling enhances the fluctuations. η converges for large values of u.

In Fig. 4.5(b), the same data are shown in the logarithmic scale. At the lowest temperatures, η is proportional to t. This is due to the temperature dependence of $\eta_0(t)-\eta_0(0) \propto t$ at the lowest temperatures. However, when u is large and the fluctuation term becomes important, the temperature dependence of η changes to t^2 in a certain range of t, and the range becomes wider as u becomes larger. The t^2 dependence of the fluctuation term in eq. (4.47) can be shown on a change of the integral variable. The temperature dependence of $\eta_0 \sim t$ is a feature of the charge fluctuations in Dirac fermions in two dimensions. It makes the mode-mode coupling term less effective compared with

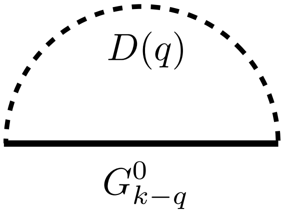

Figure 4.6: Feynman diagram which represents the electron self-energy due to the scattering by the charge fluctuations, approximated by the lowest order term. $D(q)$ and G^0_{k-q} are the propagator of the charge fluctuations and the Green's function of the electrons, respectively.

the case of conventional magnetic fluctuations in metals. In the latter case, η_0 behaves as $\eta_0 \sim t^2$, and its contribution is negligible when $t \to 0$ compared with that from the mode-mode coupling term.

4.4.2 Damping Rate of Electrons

In the SCR theory, the thermally exited bosons of fluctuations are assumed to scatter the electrons and to cause electric resistivity, as phonons do in solids. The electric resistivity is estimated from the self-energy of the electron Green's function due to the electron-boson interaction.

In the present model, eq. (4.5) is regarded as the interaction term between the bosons of charge fluctuations and the electrons. The propagator of the bosons is assumed to be the effective amplitudes of the fluctuations, $D(q)$ [eq. (4.38)] with δ determined by eq. (4.39). The electron Green's function is expanded in the interaction term by the method of many particle physics [135]. We approximate the self-energy by the lowest order term, which is expressed in the sublattice representation (s, $s' = A$, B) as

$$\Sigma_{\boldsymbol{k}ss}(i\omega_m) = -\tilde{v}^2(0)\frac{T}{N}\sum_{\boldsymbol{q}\omega_l} G^0_{\boldsymbol{k}-\boldsymbol{q}ss}(i\omega_m - i\omega_l)D(\boldsymbol{q}, i\omega_l), \tag{4.49}$$

$$\Sigma_{\boldsymbol{k}ss'}(i\omega_m) = \tilde{v}^2(0)\frac{T}{N}\sum_{\boldsymbol{q}\omega_l} G^0_{\boldsymbol{k}-\boldsymbol{q}ss'}(i\omega_m - i\omega_l)D(\boldsymbol{q}, i\omega_l) \quad (s \neq s'), \tag{4.50}$$

where $\tilde{v}(0)$ represents an effective interaction parameter between the electrons and the bosons. The corresponding Feynman diagram is shown in Fig. 4.6. Because of the phase factors in $G^0_{kss'}$ for $s \neq s'$, the off-diagonal terms of the self-energy are zero ($\Sigma_{kss'} = 0$) at the Dirac points $\boldsymbol{k} = \boldsymbol{K}$ and $\boldsymbol{K}'$. We neglect these off-diagonal terms in the following.

The Matsubara summation is transformed into an energy integral as

$$\Sigma_{\boldsymbol{k}ss}(i\omega_m) = -\tilde{v}^2(0)\frac{T}{2N}\sum_{\boldsymbol{q}\omega_l n} \frac{1}{i\omega_m - i\omega_l - \epsilon_{\boldsymbol{k}-\boldsymbol{q}n}} \frac{1}{\delta + A\sqrt{(vq)^2 + \omega_l^2}} \tag{4.51}$$

$$= \frac{\tilde{v}^2(0)}{AN} \sum_{\boldsymbol{q}n} \left(\int_{vq}^{D} - \int_{-D}^{-vq} \right) \frac{\mathrm{d}\epsilon}{2\pi} \frac{f(-\epsilon_{\boldsymbol{k}-\boldsymbol{q}n}) + n(\epsilon)}{i\omega_m - \epsilon_{\boldsymbol{k}-\boldsymbol{q}n} - \epsilon} \frac{\sqrt{\epsilon^2 - (vq)^2}}{(\delta/A)^2 + \epsilon^2 - (vq)^2}, \tag{4.52}$$

where $f(\epsilon)$ and $n(\epsilon)$ are the Fermi and Bose distribution functions, respectively. The imaginary part of the retarded self-energy is obtained as

$$\mathrm{Im}\Sigma^R_{\boldsymbol{k}ss}(\omega) = \mathrm{Im}\Sigma_{\boldsymbol{k}ss}(\omega + \mathrm{i}\eta) \tag{4.53}$$

$$= -\frac{\tilde{v}^2(0)}{2AN} \sum_{\boldsymbol{q}n} \left(\int_{vq}^{D} - \int_{-D}^{-vq} \right) \mathrm{d}\epsilon \left[f(\epsilon - \omega) + n(\epsilon) \right] \delta\left(\omega - \epsilon_{\boldsymbol{k}-\boldsymbol{q}n} - \epsilon \right) \times \frac{\sqrt{\epsilon^2 - (vq)^2}}{(\delta/A)^2 + \epsilon^2 - (vq)^2}, \tag{4.54}$$

The damping rate of electrons (or the inverse of electron lifetime) around the Dirac point $\boldsymbol{K}$ is related to the imaginary part of retarded self-energy by

$$\gamma_k = -\mathrm{Im}\Sigma^R_{\boldsymbol{K}+\boldsymbol{k}ss}(\omega = 0) \tag{4.55}$$

$$= \frac{\tilde{v}^2(0)}{AN} \sum_{\boldsymbol{q}} \int_{vq}^{D} \mathrm{d}\epsilon \frac{1}{\sinh \epsilon/T} \delta\left(\epsilon - v\left|\boldsymbol{k} - \boldsymbol{q}\right| \right) \frac{\sqrt{\epsilon^2 - (vq)^2}}{(\delta/A)^2 + \epsilon^2 - (vq)^2}, \tag{4.56}$$

where the band structure is approximated by the linear dispersion. This quantity is independent of the direction of $\boldsymbol{k}$. The two Dirac points contribute identically. γ_k depends on the temperature both explicitly and through δ. We calculate temperature dependence of γ_k near the quantum critical point, using δ obtained by solving the self-consistent equation (4.47). The path in the phase diagram is the same as in §4.4.1 (Fig. 4.4).

Figures 4.7 show $\gamma_k/\lambda D$ as a function of temperature near the quantum critical point for $u = 0, 1$, and 10, and for $vk/D = 0.1$, 10^{-2}, 10^{-3}, and 10^{-4}. $\lambda = a^2\tilde{v}^2(0)/2\pi^2 v^2 A$ is a dimensionless parameter of the coupling between the electrons and the bosons. Figures 4.7(a)-(d) all show enhancement of γ_k with increasing mode-mode coupling u. Although the enhancement itself is expected since the fluctuation amplitude $D(q)$ is enhanced by u, the temperature dependence of γ_k for small wave vectors vk/D is notable: We find that γ_k shows a peak as a function of temperature t for small vk/D as shown in Fig. 4.7(b)-(d). With decreasing vk/D, the position of the peak moves toward $t = 0$, and the shape of the peak becomes sharper. Although the absolute value decreases for smaller vk/D, the enhancement becomes stronger.

This non-monotonic temperature dependence of γ_k is caused by the temperature dependence of $\eta (= \delta/AD)$. When k is small, the denominator of the last factor in eq. (4.56) is roughly estimated as $\sim \eta^2 + v^2kq/D^2$. If $\eta^2 \gg vk/D$, the last factor behaves $\sim 1/\eta^2$. When η is suppressed by large u, this causes an increase in γ_k with decreasing temperature. We compare this increase with logarithmic and power-law dependences as shown in Fig. 4.8. γ_k can be fitted by $-\log t$ at lower temperatures near the peak ($0.1 \lesssim t \lesssim 0.3$),

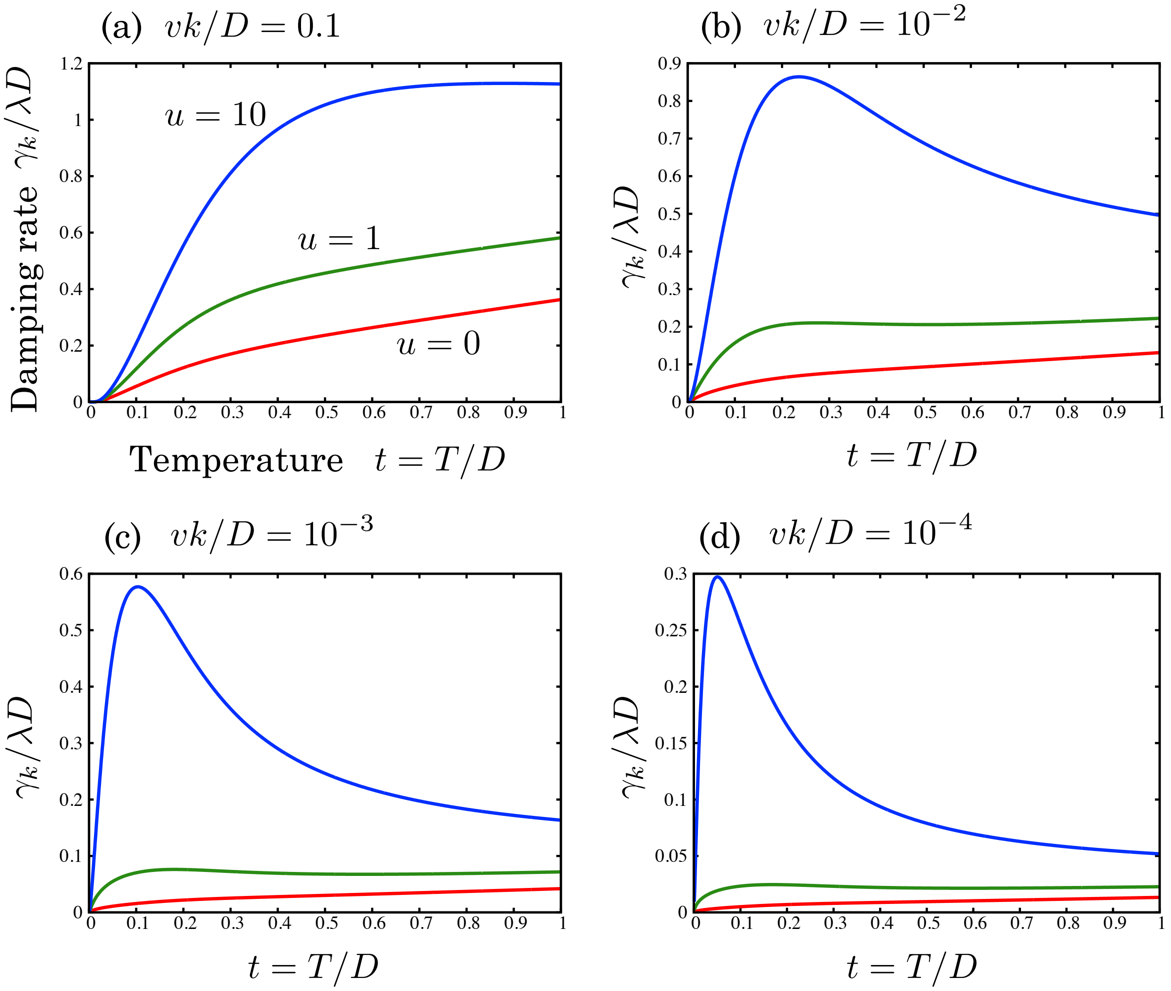

(a) $vk/D = 0.1$

(b) $vk/D = 10^{-2}$

(c) $vk/D = 10^{-3}$

(d) $vk/D = 10^{-4}$

Figure 4.7: Damping rates of electrons $\gamma_k/\lambda D$ as a function of temperature near the quantum critical point for mode-mode coupling parameters of $u = 0, 1$, and 10. $\lambda = a^2\tilde{v}^2(0)/2\pi^2 v^2 A$ is a dimensionless parameter of coupling between electrons and charge fluctuations. (a) $vk/D = 0.1$, (b) $vk/D = 10^{-2}$, (c) $vk/D = 10^{-3}$, and (d) $vk/D = 10^{-4}$.

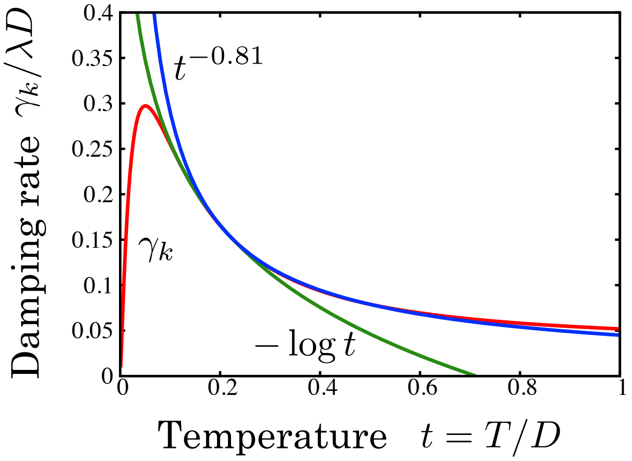

Figure 4.8: Comparison of $\gamma_k/\lambda D$ with $-\log t$ and $t^{-\alpha}$ dependences for $u = 10$, $vk/D = 10^{-4}$. Here, $\alpha = 0.81$.

while it can be fitted by $t^{-\alpha}$ at higher and wider temperatures ($0.2 \lesssim t \lesssim 0.8$) with $\alpha = 0.81$. When $\eta^2 \lesssim vk/D$, the last factor in eq. (4.56) becomes almost temperature independent, and the factor $1/\sinh(\epsilon/T)$ dominates the temperature dependence. Actually, the peak position is roughly given by the temperature where $\eta^2 \sim vk/D$. At the lowest temperature, γ_k goes to zero with power-law temperature dependence. This behavior is interpreted as absence of excited bosons at zero temperature. At $k = 0$, $\gamma_k = 0$ for all temperatures owning to the factor $\delta\left(\epsilon - vq\right)\sqrt{\epsilon^2 - (vq)^2}$ in eq. (4.56). However, if a finite damping constant is introduced in G^0 and the Dirac delta function in eq. (4.56) is replaced by a Lorentzian with the corresponding energy width, it is found that $\gamma_{k=0}$ shows similar non-monotonic temperature dependence.

The damping of electrons will lead to the electric resistivity. However, calculation of the resistivity at the Dirac points itself is subtle [18]. It has been known that the result depends on the theoretical methods and approximations involved. In this study, we do not pursue the detailed calculation of the resistivity. We expect that the non-monotonic temperature dependence of the damping of electrons can cause anomalies in the resistivity. In real solids, scattering of electrons by impurities causes non-zero resistivity at zero temperature (or residual resistivity). It has been argued that the residual resistivity is enhanced by critical fluctuations [136].

4.4.3 Specific Heat

The bosons of charge fluctuations contribute to specific heat. In the SCR theory, however, it has been known that the derivation of specific heat involves some complications, which originate from "temperature dependence of zero-point fluctuations" [137]. Its physical

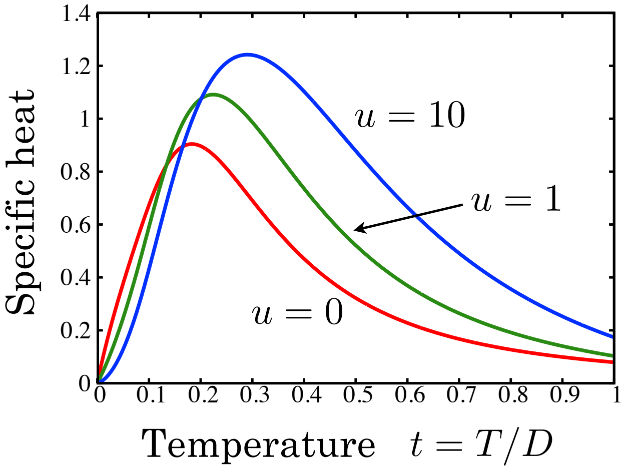

Figure 4.9: Specific heat of charge fluctuations $C/(a^2D^2/8\pi^2v^2)$ as a function of temperature near the quantum critical point for mode-mode coupling parameters of $u = 0$, 1 and 10.

meanings and practical treatments have been discussed, and it has been shown that reasonable results can be obtained if the SCR theory is formulated with the functional integral representation and all the terms are retained [137].

Here, we calculate the specific heat by numerically differentiating $\tilde{F} = F_{\text{eff}} + \Delta F$, using $\tilde{F}$ minimized with respect to δ. F_{eff} and $\Delta F = T\langle S - S_{\text{eff}}\rangle_{\text{eff}}$ are given in eq. (4.36) and (4.37). In this section, they represent the values per unit cell. Using $\partial F_{\text{eff}}/\partial\delta = (T/2N)\sum_{\boldsymbol{q}\omega_l} D(q)$, F_{eff} is represented as

$$F_{\text{eff}} = -\frac{1}{2N}\sum_{\boldsymbol{q}}\int_{vq}^{D}\frac{\mathrm{d}\epsilon}{\pi}\coth\frac{\epsilon}{2T}\tan^{-1}\frac{A\sqrt{\epsilon^2-(vq)^2}}{\delta}, \tag{4.57}$$

where the δ independent constant is determined by the value of F_{eff} calculated directly from eq. (4.36) at $\delta = 0$. After the $\boldsymbol{q}$ integration, F_{eff} can be expressed by the dimensionless parameters as

$$F_{\text{eff}}/\left(\frac{a^2D^3}{8\pi^2v^2}\right) = -\eta^2\int_0^1\mathrm{d}x\coth\frac{x}{2t}\left\{\left[1+\left(\frac{x}{\eta}\right)^2\right]\tan^{-1}\frac{x}{\eta}-\frac{x}{\eta}\right\}. \tag{4.58}$$

From eq. (4.37) and using the self-consistent equation (4.39), ΔF is expressed as $\Delta F = -\left(\delta-\delta_0\right)^2/12g$. On the path shown in Fig. 4.4, ΔF is given by

$$\Delta F/\left(\frac{a^2D^3}{8\pi^2v^2}\right) = -\frac{1}{u}\left[\eta+\frac{u}{2}-\frac{8}{\pi}t\log\frac{2}{1+\mathrm{e}^{-1/t}}\right]^2. \tag{4.59}$$

From the free energy, the specific heat is calculated as $C = -T\partial^2\tilde{F}/\partial T^2$.

Figure 4.9 shows the temperature dependence of $C/(a^2D^2/8\pi^2v^2)$ for the same parameters as the previous section. For every value of u, the specific heat has a broad peak. The decrease at higher temperature region originates from the temperature dependence of the Bose distribution function. This is understood since such a decrease appears even if a constant η is assumed. With increasing u, the position of the peak shifts toward high temperature, and the hight of the peak increases. This increase of the specific heat for $t \gtrsim 0.2$ with increasing u is regarded as the usual enhancement of specific heat near the critical point due to the mode-mode coupling. On the other hand, at low temperature ($t \lesssim 0.2$) the specific heat is suppressed by u. This behavior comes from the characteristic η dependence of the free energy in the present system, and the smaller η at low temperature causes the smaller specific heat. When $u = 0$, $C \sim t$ at low temperature. As u increases, this behavior changes to the behavior $C \sim t^2$ in a certain temperature range.

4.4.4 Self-Energy and Density of States

The interaction with the charge fluctuations causes the self-energy of the electrons, and hence modifies their single-particle properties. In this section, the self-energy is investigated mainly as a function of energy ω and its characteristic behaviors are revealed. Their effects on density of states (DOS) are evaluated.

To calculate the self-energy, we make the same approximation as in §4.4.2, that is, the self-energy is approximated by the lowest order term in the electron-boson interaction, and its off-diagonal elements are neglected. Under this approximation, the imaginary part, which is denoted by $\gamma_k(\omega)$, is given by

$$\gamma_k(\omega) = \mathrm{Im}\Sigma^R_{\boldsymbol{K}+\boldsymbol{k}ss}(\omega) \tag{4.60}$$

$$= -\frac{\tilde{v}^2(0)}{2AN}\sum_{\boldsymbol{q}n=\pm 1}\left(\int_{vq}^{D} - \int_{-D}^{-vq}\right)\mathrm{d}\epsilon\,[f(\epsilon-\omega)+n(\epsilon)]\,\delta\left(\omega - nv|\boldsymbol{k}-\boldsymbol{q}|-\epsilon\right)$$
$$\times\frac{\sqrt{\epsilon^2-(vq)^2}}{(\delta/A)^2+\epsilon^2-(vq)^2}, \tag{4.61}$$

where the band structure is approximated by the Dirac dispersion around the Dirac point $\boldsymbol{K}$. The both Dirac points contribute identically. The real part, which is denoted by $\alpha_k(\omega)$, is obtained from the imaginary part by the Kramers-Kronig relation as

$$\alpha_k(\omega) = \mathrm{Re}\Sigma^R_{\boldsymbol{K}+\boldsymbol{k}ss}(\omega) \tag{4.62}$$

$$= -\int_0^\infty \frac{\mathrm{d}\epsilon}{\pi}\mathrm{Im}\Sigma^R_{\boldsymbol{K}+\boldsymbol{k}ss}(\epsilon)\mathcal{P}\left(\frac{1}{\omega-\epsilon}+\frac{1}{\omega+\epsilon}\right), \tag{4.63}$$

where the relation $\mathrm{Im}\Sigma^R_{\boldsymbol{k}ss}(-\omega) = \mathrm{Im}\Sigma^R_{\boldsymbol{k}ss}(\omega)$ is used.

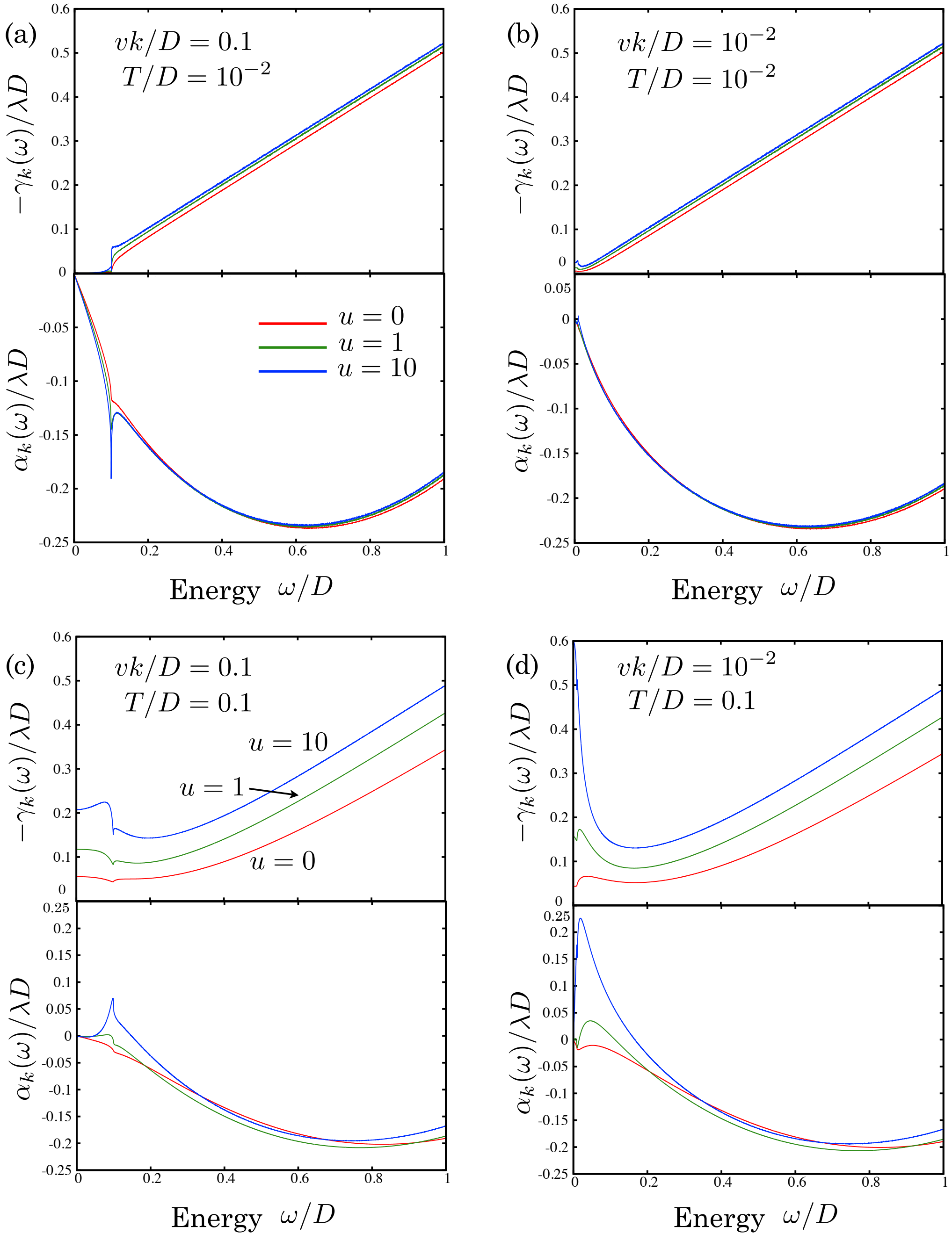

Figure 4.10: Self-energy of electrons as a function of energy ω/D for mode-mode coupling parameters of $u = 0$, 1, and 10, and for wave vectors and temperatures of (a) $vk/D = 0.1$ and $T/D = 10^{-2}$, (b) $vk/D = 10^{-2}$ and $T/D = 10^{-2}$, (c) $vk/D = 0.1$ and $T/D = 0.1$, and (d) $vk/D = 10^{-2}$ and $T/D = 0.1$. $-\gamma_k(\omega)/\lambda D = -\mathrm{Im}\Sigma^R_{\boldsymbol{K}+\boldsymbol{k}ss}(\omega)/\lambda D$ and $\alpha_k(\omega)/\lambda D = \mathrm{Re}\Sigma^R_{\boldsymbol{K}+\boldsymbol{k}ss}(\omega)/\lambda D$ are shown for $\omega > 0$. The values for $\omega < 0$ can be obtained from the relations $\gamma_k(-\omega) = \gamma_k(\omega)$ and $\alpha_k(-\omega) = -\alpha_k(\omega)$. λ is a dimensionless parameter of coupling between the electrons and the charge fluctuations.

Figures 4.10(a) and (b) show $\gamma_k(\omega)/\lambda D$ and $\alpha_k(\omega)/\lambda D$ as a function of ω/D for $u = 0$, 1, and 10, for $vk/D = 0.1$ and 10^{-2} at $T/D = 10^{-2} \ll 1$. The values for $\omega > 0$ are shown. Those of $\omega < 0$ are obtained from the relations of $\gamma_k(-\omega) = \gamma_k(\omega)$ and $\alpha_k(-\omega) = -\alpha_k(\omega)$. In these low-temperature case, the differences when u is varied are small. This is because δ is practically zero at this temperature for every values of u, compared with vk and ω.

As shown in Fig. 4.10(a), $\gamma_k(\omega) = 0$ for $\omega < vk$ when vk/D is finite. This corresponds to the absence of single-particle excitation in this region. For $\omega > vk$, $-\gamma_k(\omega)$ increases linearly with ω. As shown in the lower figure in Fig. 4.10(a), $\alpha_k(\omega) < 0$ for all ω and its slope is negative at $\omega = 0$. The cusp in $\alpha_k(\omega)$ at $\omega = vk$ corresponds to the step-like behavior in $\gamma_k(\omega)$. The cusp is sharper for larger u.

As shown in Fig. 4.10(b), when $vk/D = 0.01 \ll 1$, $-\gamma_k(\omega)$ is almost linear to ω, and the slope of $\alpha_k(\omega)$ at $\omega = 0$ is negatively large. In the present limit ($T = 0$ and $vk = 0$), the integrations in eq. (4.61) and (4.63) yield an explicit expression of the self-energy:

$$-\gamma_{k=0}(\omega) = \frac{\pi}{6}\lambda|\omega|\theta\left(2D - |\omega|\right), \tag{4.64}$$

$$\alpha_{k=0}(\omega) = -\frac{\lambda}{6}\omega \log\left|\frac{4D^2 - \omega^2}{\omega^2}\right| \tag{4.65}$$

$$\simeq -\frac{\lambda}{3}\omega \log\left|\frac{D}{\omega}\right| \quad (\omega/D \ll 1). \tag{4.66}$$

This logarithmic factor causes a divergence in the derivative of $\alpha_{k=0}(\omega)$ at $\omega = 0$.

At finite T/D, on the other hand, we find that $-\gamma_k(\omega)$ is enhanced appreciably by u as shown in Figs. 4.10(c) and (d). When vk/D is finite [Fig. 4.10(c)], $-\gamma_k(\omega)$ has a finite value for $\omega < vk$ in contrast to the case of $T/D \ll 1$. The enhancement by u is larger for this region than for $\omega > vk$. A cusp appears at $\omega = vk$. The negative slope of $-\gamma_k(\omega)$ around $\omega = vk$ corresponds to the positive value of $\alpha_k(\omega)$ around it as shown in the lower figure of Fig. 4.10(c). With large u, $\alpha_k(\omega)$ shows a positive peak at $\omega = vk$.

As shown in Fig. 4.10(d), $-\gamma_k(\omega)$ shows a peak around $\omega = 0$ for large u when $vk/D = 0.01 \ll 1$. This peak corresponds to a positive slope of $\alpha_k(\omega)$ around $\omega = 0$ as shown in the lower figure of Fig. 4.10(d).

These behaviors around $\omega = 0$ in Figs. 4.10(c) and (d) contrast with that of conventional interacting fermion systems, where $-\gamma_k(\omega)$ has a minimum at $\omega = 0$ and the slope of $\alpha_k(\omega)$ is negative. A peak of $-\gamma_k(\omega)$ at $\omega = 0$ and a corresponding positive slope of $\alpha_k(\omega)$ have been argued in studies of superconducting fluctuations [138, 139]. In the present system, since the dispersion of electrons modified by the interaction is determined by $E_{kn} = nvk + \alpha_k(E_{kn})$, the positive $\alpha_k(\omega)$ in $\omega > 0$ causes $E_{k+} > vk$. This is regarded as enhancement of the Fermi velocity v, and will lead to suppression of the density of states.

To clarify the effects of these characteristic behaviors of the self-energy on the physical quantities, we calculate the density of states. It is expressed by an electron Green's function as

$$\rho(\omega) = -\frac{1}{\pi}\frac{1}{2N}\mathrm{Im}\mathrm{Tr}G^R(\omega), \tag{4.67}$$

where the factor 1/2 is from the two sublattice degrees of freedom. The Green's function is related to a self-energy by

$$G^R = \left[\left(G^{0R}\right)^{-1} - \Sigma^R\right]^{-1}. \tag{4.68}$$

Within the approximations introduced above, the DOS is expressed as

$$\rho(\omega) = -\frac{1}{\pi N}\sum_{\boldsymbol{k}n=\pm 1}\frac{\gamma_k(\omega)}{\left[\omega - nvk - \alpha_k(\omega)\right]^2 + \gamma_k^2(\omega)}, \tag{4.69}$$

where the factor 2 comes from the degeneracy of the two Dirac points. In the non-interacting case, the DOS is obtained as $\rho(\omega) = (a^2/2\pi v^2)|\omega|\theta\left(D - |\omega|\right)$.

As shown in Fig. 4.10(a), $\gamma_k(\omega)$ becomes almost zero in the region of $vk > \omega$ when $T/D \ll 1$. This makes a direct numerical evaluation of eq. (4.69) difficult. Instead, we calculate the DOS at $T = 0$ using the following formulae for $\gamma_k(\omega)$ and $\alpha_k(\omega)$:

$$\gamma_k(\omega) = -\frac{\lambda}{2}|\omega|\theta(\omega - vk)\theta(2D - \omega), \tag{4.70}$$

$$\alpha_k(\omega) = -\frac{\lambda}{2\pi}\omega\log\left|\frac{4D^2 - \omega^2}{(vk)^2 - \omega^2}\right|. \tag{4.71}$$

These formulae well reproduce $\gamma_k(\omega)$ and $\alpha_k(\omega)$ calculated numerically from eqs. (4.61) and (4.63) at $T/D \ll 1$. In the region where $\gamma_k(\omega) = 0$, the integrant in the right-hand side of eq. (4.69) is replaced by a Dirac delta function $-\pi\delta\left(\omega - nvk - \alpha_k(\omega)\right)$. At $T = 0$, since $\delta = 0$ on the quantum critical point, $\rho(\omega)$ is independent of u.

Figures 4.11 show $\rho(\omega)/(a^2D/2\pi^2v^2)$ as a function of ω/D for $T/D = 0$ and 0.1, and for $u = 0$, 1, and 10 in the latter temperature. To see the tendency, we chose $\lambda = 1$, as $\rho(\omega)$ approaches the non-interacting value with decreasing λ. The non-interacting case of $\rho(\omega)$ is also shown. The values for $\omega < 0$ can be obtained by $\rho(-\omega) = \rho(\omega)$.

It is found that $\rho(\omega)$ is enhanced at $T = 0$ [Fig. 4.11(a)] and suppressed for most ω at finite temperatures [Fig. 4.11(b)], compared with the non-interacting values. Both behaviors are in accordance with those expected from the ω dependence of $\alpha_k(\omega)$ shown in Fig. 4.10. At finite temperature [Fig. 4.11(b)], the suppression is larger for larger values of u. Finite $\rho(\omega)$ appears for $\omega \lesssim T$ at the finite temperature. This is due to the finite $\gamma_k(\omega)$ in this region.

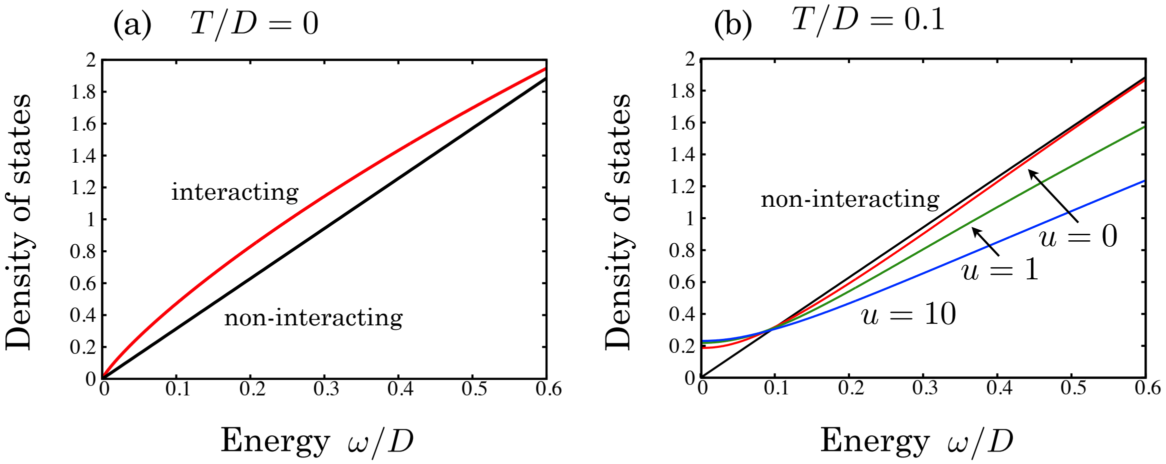

Figure 4.11: Density of states of electrons as a function of energy ω/D for the temperatures of (a) $T/D = 0$ and (b) $T/D = 0.1$, and for the mode-mode coupling parameters of $u = 0$, 1, and 10 in the latter. The non-interacting case is also shown. The unit of the density of states is $a^2D/2\pi^2v^2$. The values for $\omega < 0$ can be obtained by $\rho(-\omega) = \rho(\omega)$.

4.5 Summary and Discussions

We have investigated effects of charge fluctuations on Dirac fermions in the vicinity of the quantum critical point associated with a charge ordering transition by using a minimal model which describes Dirac fermions in two dimensions and their charge ordering. This model will be qualitatively valid as long as the magnetic ordering is far away. The Fermi energy has been fixed at the energy of the Dirac points. First, deriving a Landau-Ginzburg-Wilson functional from this model within the linear dispersion approximation, we have found that the charge fluctuations in Dirac fermions obey a characteristic dispersion which contains variables q and ω_l in a symmetric manner. Analyzing this functional with the perturbative renormalization group (PRG) method and the self-consistent renormalization (SCR) theory, we have shown that the effects of the mode-mode coupling between fluctuations tend to be less effective in Dirac fermions compared with the case of conventional magnetic fluctuations in metals.

Second, we have calculated physical quantities by using the SCR theory. The SCR theory can be used even when the mode-mode coupling is large. We have investigated the electron self-energy caused by the scattering with the charge fluctuations within the lowest order in the interaction between them. We have shown that the self-energy shows peaks as a function of temperature and energy ω when the mode-mode coupling is strong. These characteristic behaviors of the self-energy lead to an increase of the electron damping with decreasing temperature near the quantum critical point, and suppression of the density of states at finite temperatures. We have also calculated the specific heat of the charge fluctuations. At low temperatures, its temperature dependence is varied by the strength of the mode-mode coupling.

Here, we discuss relevance of these results to the experimental facts on α-(BEDT-TTF)$_2$I$_3$, expecting that the introduced minimal model captures the essential features of the Dirac fermions and their charge ordering in this material. The energy scale D is estimated as about 40 K [43].

The increase of the electron damping with decreasing temperature near the quantum critical point (QCP) will explain the increase of resistivity observed experimentally [92] (Fig. 3.1). However, note that the relation between the damping and the resistivity is not so simple in Dirac fermions, and that the impurity scattering may play important roles at the lowest temperatures. Another unclear point is the relation between the distance from the QCP, δ, and the applied pressure. Although the experiments are usually performed at higher pressures than the critical pressure, the present results will be relevant if the experimental systems remain near the QCP even at the higher pressures.

The measurement of the specific heat has been reported in the temperature range of $T \lesssim 10$ K, and it behaves like $\sim T^{1.8}$ [40] (Fig. 4.3). In the present calculation within this temperature range, the specific heat of charge fluctuations shows nearly T^2 dependence when the mode-mode coupling is strong, which is compatible with the experiment.

From the NMR measurements [43], characteristic temperature dependence of the spin susceptibility has been reported, namely, the suppression at low temperatures ($\lesssim 30$ K) and the enhancement at higher temperatures, compared with non-interacting values. Since the spin susceptibility is proportional to the density of states, the suppression is the same tendency as the present calculation at finite temperatures. Although the density of states is enhanced at the quantum critical point in the present calculation, we expect that the suppression occurs at zero temperature if the system is not at the quantum critical point and if effects of impurity scattering (or finite electron damping) are taken into account. To explain the enhancement at higher temperatures, other band structures such as a van Hove singularity must be included.

Chapter 5

Summary and Outlook

5.1 Summary

In this thesis, we have theoretically studied effects of electron-electron interaction on Dirac fermions in solids in relation to experimental facts on graphene and on an organic conductor α-(BEDT-TTF)$_2$I$_3$. In chapter 2, local electron correlation, or the Kondo effect, has been studied in graphene with defects. In chapter 4, effects of electron-electron interaction in the bulk have been studied in the Dirac fermion phase of α-(BEDT-TTF)$_2$I$_3$ which is located next to charge-ordered phase. As a topic related to both chapter 2 and 4, electronic states near single defect in α-(BEDT-TTF)$_2$I$_3$ have been studied in chapter 3. These studies have shown that the electron-electron interaction can appear in the Dirac fermions and can affect their electronic properties.

In chapter 2, the Kondo effect due to point defects in graphene has been investigated. We have described that local electron states consisting of dangling sp^2 orbitals at the defect can have a localized magnetic moment, where the electron-electron interaction in the sp^2 orbital is essential. This localized magnetic moment can interacts with the π conduction electrons under certain conditions, and cause the Kondo effect. We have developed an effective model for this Kondo effect, where characteristic features of the Dirac conduction electrons are included through the local density of states (LDOS) at the defect. One of the characteristic features of Dirac fermions in graphene is the appearance of a localized state at the defect. We have analyzed low-energy behaviors of the resulting model by the numerical renormalization group (NRG) method. First, assuming low density of the defects, we have investigated the model without the localized state of π electrons. When the hybridization between the sp^2 and π orbital is large, the Kondo temperature shows a nonzero minimum value at the zero chemical potential and almost symmetric dependence for the positive and negative chemical potentials. This can qualitatively explain the gate-voltage dependence observed experimentally. However, the critical hybridization $V_c \simeq 0.6D$ is rather large compared with the band width. Second, assuming a finite density of the defects, we have studied the effect of the localized state of π electrons. We have shown that this localized state assists the Kondo screening when the chemical potential is near the Dirac points. The critical hybridization can be one tenth smaller than the value above, which is considered to be more realistic. In relation to this behavior, we have studied the effect of the orbital motion of the π electrons in magnetic field, and found that the orbital motion reduces the LDOS of π electrons at the defect. This will suppress the Kondo screening, and hence will qualitatively explain the experimentally observed behavior in magnetic field.

As is mentioned in chapter 2, a localized state appears at the defect in graphene. In chapter 3, we have investigated whether such a state appears in α-(BEDT-TTF)$_2$I$_3$ with a single defect. By solving a realistic tight-binding Hamiltonian, we have found that a localized state at the energy of the Dirac points is induced by the defect at certain sites (A or A'). Using the Green's function method, we have evaluated the wave function of the localized state in the $\boldsymbol{k}$ space, and found that this localized state consists of the electrons and the holes around the Dirac points. This localized state shows anisotropy around the Dirac points, which reflects the tilting of the Dirac cones in α-(BEDT-TTF)$_2$I$_3$. This anisotropy in the $\boldsymbol{k}$ space leads to that in the real space. This means that the tilting of the Dirac cones in this material can be detected experimentally by measuring the localized state with microscopic probes such as STM.

In chapter 4, motivated by the Dirac fermions near charge ordering realized in α-(BEDT-TTF)$_2$I$_3$, we have investigated effects of critical charge fluctuations on Dirac fermions. We have introduced a simplified model which captures essential features of the Dirac fermions and the charge ordering in this material. First, deriving a Landau-Ginzburg-Wilson functional from this model, we have found that the charge fluctuations in Dirac fermions obey a characteristic dispersion which contains variables q and ω_l in a symmetric manner. Analyzing this functional with the perturbative renormalization group (PRG) method and the self-consistent renormalization (SCR) theory, we have shown that the effects of the mode-mode coupling between fluctuations tend to be less effective in Dirac fermions compared with the case of conventional magnetic fluctuations in metals. Second, physical quantities have been calculated with the SCR theory. It has been shown that the interaction between the electrons and the charge fluctuations causes peaks of the electron self-energy as a function of temperature and energy ω when the mode-mode coupling is strong. These characteristic behaviors of the self-energy can lead to an increase of the electron damping with decreasing temperature near the quantum critical point, and suppression of the density of states. We have also calculated the specific heat of the charge fluctuations. These results obtained with large mode-mode coupling are compatible with experimental results on α-(BEDT-TTF)$_2$I$_3$ such as resistivity, specific heat, and spin susceptibility.

5.2 Outlook

Here, we list future problems related to the studies in this thesis.

Kondo Effect in Graphene with Defects

1. Since the orbital effect of magnetic field is larger in graphene than in ordinary metals, it must be important in understanding the behavior of Kondo effect in graphene in magnetic field. Especially, the effect of Landau quantization on the Kondo effect is an interesting problem.

2. We have considered only the most stable Jahn-Teller distorted structure of the defect, i.e. $h \neq h'$. However, the threefold symmetric structure may be realized under certain conditions. In such a case, there is a degeneracy of the molecular orbitals at the defect site. It can cause a more exotic Kondo effect such as the three-impurity Kondo effect [140].

3. Dynamical effects of the lattice degrees of freedom at the defect site have been neglected. Actually, the dynamical switching of the covalent bond (dynamical Jahn-Teller effect) in the point defect has been discussed [66, 141]. We speculate that this effect enhances the electron scattering at the defect and hence enhances the Kondo effect [142, 143].

Localized State in α-(BEDT-TTF)$_2$I$_3$ Induced by Single Defect

1. Electron-electron interaction has been ignored in this chapter. However, large LDOS at the Fermi energy induced by defect combined with the electron-electron interaction can cause instabilities toward locally-ordered states such as local ferromagnetism. The magnetic instability has been discussed in graphene as a possible origin of localized magnetic moments [57, 71]. Such a scenario is also possible in α-(BEDT-TTF)$_2$I$_3$.

Effects of Charge Fluctuations on Dirac Fermions in α-(BEDT-TTF)$_2$I$_3$

1. Since experiments are usually performed at higher pressures than the critical pressure, theoretical investigation of the parameter region far from the quantum critical point is necessary to compare the theory and the experiments.

2. To estimate the resistivity at the lowest temperature, effects of impurity scattering must be included. We expect that entanglement of scattering by impurities and that by charge fluctuations will enhance residual resistivity near the quantum critical point [136].

3. To investigate properties of α-(BEDT-TTF)$_2$I$_3$ at higher temperatures, other band structures such as a van Hove singularity must be included. In order to include more realistic band structure, other formalisms such as the fluctuation-exchange (FLEX) approximation are suitable.

4. In the NMR measurements, a weak increase of the nuclear spin-lattice relaxation rate (divided by the temperature) with decreasing temperature at several K has been reported [43]. This indicates that spin fluctuations exist and they are enhanced when the temperature is lowered. We expect that the spin fluctuations are weekly coupled with the charge fluctuations, and the enhanced charge fluctuations cause small enhancement of the spin fluctuations. Such enhancement of spin fluctuations will be described by retaining the spin fluctuation term in the present formalism.

Acknowledgements

I would like to express my sincere gratitude to Prof. Masao Ogata for his continuous encouragement and invaluable suggestions during the course of my study. I also wish to express my sincere thanks to Dr. Hiroyasu Matsuura for his helpful discussions and kind instructions. I would like to acknowledge Prof. Hideo Aoki, Prof. Hiroshi Fukuyama, Prof. Kazushi Kanoda, Prof. Takeo Kato, and Prof. Toshihito Osada for constructive comments and careful reading of this thesis.

I am grateful to Prof. Kazumasa Miyake for stimulating conversations and discussions on the Kondo effect and quantum critical phenomena, and Prof. Yoshikazu Suzumura for helpful suggestions on the studies of α-(BEDT-TTF)$_2$I$_3$. I should like to acknowledge gratefully the discussions with Prof. Yoichi Yanase on the Kondo effect, Dr. Jian-Hao Chen on the experiments of the Kondo effect in graphene with defect, Prof. Naoya Tajima, Dr. Kazuya Miyagawa, and Dr. Michihiro Hirata on the experiments of α-(BEDT-TTF)$_2$I$_3$, and Dr. Yasuhiro Tanaka on the theory of electron correlation in this material. I also note that this work has been supported by a Grant-in-Aid for Scientific Research A on “Dirac Electrons in Solids” (No. 24244053), from the Japan Society for the Promotion of Science.

I would like to heartily thank Prof. Yuki Fuseya, Dr. Hiroshi Watanabe, Dr. Ryo Igarashi and Dr. Toshikaze Kariyado for kind instructions and encouragement, and all the colleagues of Ogata laboratory, Dr. Igor Proskurin, Akihiro Igarashi, Naoya Arakawa, Taichi Hinokihara, Tomonari Mizoguchi, Remo Morii, and Nobuyuki Okuma for everyday conversations and discussions.

Finally, I gratefully acknowledge my family and my friends for their encouragement for years.

References

[1] J. M. Ziman: *Principles of the Theory of Solids* (Cambridge University Press, Cambridge, 1972) 2nd ed.

[2] P. A. M. Dirac: Proc. R. Soc. London, Ser. A **117** (1928) 610.

[3] P. R. Wallace: Phys. Rev. **71** (1947) 622.

[4] P. A. Wolff: J. Phys. Chem. Solids **25** (1964) 1057.

[5] S. Katayama, A. Kobayashi, and Y. Suzumura: J. Phys. Soc. Jpn. **75** (2006) 054705.

[6] S. Ishibashi, K. Terakura, and H. Hosono: J. Phys. Soc. Jpn. **77** (2008) 053709.

[7] H. Fukuyama: JPSJ Online–News and Comments [May 12, 2008].

[8] M. Z. Hasan and C. L. Kane: Rev. Mod. Phys. **82** (2010) 3045.

[9] T. Kariyado and M. Ogata: J. Phys. Soc. Jpn. **80** (2011) 083704.

[10] A. H. Castro Neto, F. Guinea, N. M. R. Peres, K. S. Novoselov, and A. K. Geim: Rev. Mod. Phys. **81** (2009) 109.

[11] D. S. L. Abergel, V. Apalkov, J. Berashevich, K. Ziegler, and T. Chakraborty: Adv. Phys. **59** (2010) 261.

[12] K. S. Novoselov, A. K. Geim, S. V. Morozov, D. Jiang, Y. Zhang, S. V. Dubonos, I. V. Grigorieva, and A. A. Firsov: Science **306** (2004) 666.

[13] K. S. Novoselov, A. K. Geim, S. V. Morozov, D. Jiang, M. I. Katsnelson, I. V. Grigorieva, S. V. Dubonos, and A. A. Firsov: Nature **438** (2005) 197.

[14] Y. Zhang, Y.-W. Tan, H. L. Stormer, and P. Kim: Nature **438** (2005) 201.

[15] G. S. Painter and D. E. Ellis: Phys. Rev. B **1** (1970) 4747.

[16] R. Saito, G. Dresselhaus, and M. S. Dresselhaus: *Physical Properties of Carbon Nanotubes* (Imperial College Press, London, 1998).

[17] T. Ando: J. Phys. Soc. Jpn. **74** (2005) 777.

[18] S. Das Sarma, S. Adam, E. H. Hwang, and E. Rossi: Rev. Mod. Phys. **83** (2011) 407.

[19] T. Ishiguro, K. Yamaji, and G. Saito: *Organic Superconductors* (Springer Verlag, Berlin, 1998) 2nd ed.

[20] H. Fukuyama: J. Phys. Soc. Jpn. **75** (2006) 051001.

[21] A. Kobayashi, Y. Okano, and H. Kobayashi: J. Phys. Soc. Jpn. **75** (2006) 051002.

[22] H. Mori: J. Phys. Soc. Jpn. **75** (2006) 051003.

[23] J. Ferraris, D. O. Cowan, V. V. Walatka, and J. H. Perlstein: J. Am. Chem. Soc. **95** (1973) 948

[24] G. Saito, T. Enoki, K. Toriumi, and H. Inokuchi: Solid State Commun. **42** (1982) 557.

[25] M. Mizuno, A. F. Garito, and M. P. Cava: J. Chem. Soc., Chem. Commun. (1978) 18.

[26] K. Bender, I. Hennig, D. Schweitzer, K. Dietz, H. Endres, and H. J. Keller: Mol. Cryst. Liq. Cryst. **108** (1984) 359.

[27] Y. Takano, K. Hiraki, H. M. Yamamoto, T. Nakamura, and T. Takahashi: J. Phys. Chem. Solids **62** (2001) 393.

[28] R. Wojciechowski, K. Yamamoto, K. Yakushi, M. Inokuchi, and A. Kawamoto: Phys. Rev. B **67** (2003) 224105.

[29] H. Schwenk, F. Gross, C.-P. Heidmann, K. Andres, D. Schweitzer, and H. Keller: Mol. Cryst. Liq. Cryst. **119** (1985) 329.

[30] M. V. Kartsovnik, P. A. Kononvich, V. N. Laukhin, A. G. Khomenko, and I. F. Shchegolev: Sov. Phys. JETP **61** (1985) 866.

[31] T. Mishima, K. Kajita, Y. Nishio, and Y. Iye: Mater. Sci. Eng. B **25** (1994) L1.

[32] N. Tajima, M. Tamura, Y. Nishio, K. Kajita, and Y. Iye: J. Phys. Soc. Jpn. **69** (2000) 543.

[33] R. Kondo, S. Kagoshima, and J. Harada: Rev. Sci. Instrum. **76** (2005) 093902.

[34] H. Kino and T. Miyazaki: J. Phys. Soc. Jpn. **75** (2006) 034704.

[35] S. Ishibashi, T. Tamura, M. Kohyama, and K. Terakura: J. Phys. Soc. Jpn. **75** (2006) 015005.

[36] N. Tajima, S. Sugawara, M. Tamura, Y. Nishio, and K. Kajita: J. Phys. Soc. Jpn. **75** (2006) 051010.

[37] Y. Takano, K. Hiraki, Y. Takada, H. M. Yamamoto, and T. Takahashi: J. Phys. Soc. Jpn. **79** (2010) 104704.

[38] S. Hirose and A. Kawamoto: Phys. Rev. B **82** (2010) 115114.

[39] M. Hirata, K. Ishikawa, K. Miyagawa, K. Kanoda, and M. Tamura: Phys. Rev. B **84** (2011) 125133.

[40] T. Konoike, K. Uchida, and T. Osada: J. Phys. Soc. Jpn. **81** (2012) 043601.

[41] T. Konoike, M. Sato, K. Uchida, and T. Osada: J. Phys. Soc. Jpn. **82** (2013) 073601.

[42] I. Proskurin and M. Ogata: J. Phys. Soc. Jpn. **82** (2013) 063712.

[43] M. Hirata: Dr. Thesis, Department of Applied Physics, Graduate School of Engineering, The University of Tokyo, Tokyo (2012).

[44] N. Tajima, T. Yamauchi, T. Yamaguchi, M. Suda, Y. Kawasugi, H. M. Yamamoto, R. Kato, Y. Nishio, and K. Kajita: Phys. Rev. B **88** (2013) 075315.

[45] D. Pines and P. Nozières: *The Theory of Quantum Liquids* (Perseus, Cambridge, 1999).

[46] V. N. Kotov, B. Uchoa, V. M. Pereira, F. Guinea, and A. H. Castro Neto: Rev. Mod. Phys. **84** (2012) 1067.

[47] D. C. Elias, R. V. Gorbachev, A. S. Mayorov, S. V. Morozov, A. A. Zhukov, P. Blake, L. A. Ponomarenko, I. V. Grigorieva, K. S. Novoselov, F. Guinea, and A. K. Geim: Nat. Phys. **7** (2011) 701.

[48] A. C. Hewson: *The Kondo Problem to Heavy Fermions* (Cambridge University Press, Cambridge, 1993).

[49] D. L. Cox and A. Zawadowski: Adv. Phys. **47** (1998) 599.

[50] K. G. Wilson: Rev. Mod. Phys. **47** (1975) 773.

[51] J. Kondo: Prog. Theor. Phys. **32** (1964) 37.

[52] T. A. Costi, L. Bergqvist, A. Weichselbaum, J. von Delft, T. Micklitz, A. Rosch, P. Mavropoulos, P. H. Dederichs, F. Mallet, L. Saminadayar, and C. Bäuerle: Phys. Rev. Lett. **102** (2009) 056802.

[53] L. Fritz and M. Vojta: Rep. Prog. Phys. **76** (2013) 032501.

[54] K. Sengupta and G. Baskaran: Phys. Rev. B **77** (2008) 045417.

[55] M. Vojta, L. Fritz, and R. Bulla: Europhys. Lett. **90** (2010) 27006.

[56] Z.-G. Zhu, K.-H. Ding, and J. Berakdar: Europhys. Lett. **90** (2010) 67001.

[57] P. Haase, S. Fuchs, T. Pruschke, H. Ochoa, and F. Guinea: Phys. Rev. B **83** (2011) 241408.

[58] V. W. Brar, R. Decker, H.-M. Solowan, Y. Wang, L. Maserati, K. T. Chan, H. Lee, C. O. Girit, A. Zettl, S. G. Louie, M. L. Cohen, and M. F. Crommie: Nat. Phys. **7** (2011) 43.

[59] J.-H. Chen, L. Li, W. G. Cullen, E. D. Williams, and M. S. Fuhrer: Nat. Phys. **7** (2011) 535.

[60] O. V. Yazyev: Rep. Prog. Phys. **73** (2010) 056501.

[61] P. Esquinazi, D. Spemann, R. Höhne, A. Setzer, K.-H. Han, and T. Butz: Phys. Rev. Lett. **91** (2003) 227201.

[62] R. R. Nair, M. Sepioni, I-L. Tsai, O. Lehtinen, J. Keinonen, A. V. Krasheninnikov, T. Thomson, A. K. Geim, and I. V. Grigorieva: Nat. Phys. **8** (2012) 199.

[63] M. M. Ugeda, I. Brihuega, F. Guinea, and J. M. Gómez-Rodríguez: Phys. Rev. Lett. **104** (2010) 096804.

[64] T. Kondo, Y. Honma, J. Oh, T. Machida, and J. Nakamura: Phys. Rev. B **82** (2010) 153414.

[65] J. C. Meyer, C. Kisielowski, R. Erni, M. D. Rossell, M. F. Crommie, and A. Zettl: Nano Lett. **8** (2008) 3582.

[66] A. A. El-Barbary, R. H. Telling, C. P. Ewels, M. I. Heggie, and P. R. Briddon: Phys. Rev. B **68** (2003) 144107.

[67] P. O. Lehtinen, A. S. Foster, Y. Ma, A. V. Krasheninnikov, and R. M. Nieminen: Phys. Rev. Lett. **93** (2004) 187202.

[68] O. V. Yazyev and L. Helm: Phys. Rev. B **75** (2007) 125408.

[69] K. Wakabayashi: J. Phys. Soc. Jpn. **71** (2002) 2500.

[70] V. M. Pereira, F. Guinea, J. M. B. Lopes dos Santos, N. M. R. Peres, and A. H. Castro Neto: Phys. Rev. Lett. **96** (2006) 036801.

[71] H. Kumazaki and D. S. Hirashima: J. Phys. Soc. Jpn. **76** (2007) 034707.

[72] A. Toyoda and T. Ando: J. Phys. Soc. Jpn. **79** (2010) 094708.

[73] T. Kanao, H. Matsuura, and M. Ogata: J. Phys. Soc. Jpn. **81** (2012) 063709.

[74] M. A. Cazalilla, A. Iucci, F. Guinea, and A. H. Castro Neto: arXiv:1207.3135v1.

[75] A. K. Mitchell and L. Fritz: Phys. Rev. B **88** (2013) 075104.

[76] S. A. Jafari and T. Tohyama: arXiv:1308.4173v1.

[77] M. Kharitonov and G. Kotliar: Phys. Rev. B **88** (2013) 201103.

[78] T. Kanao, H. Matsuura, and M. Ogata: J. Phys.: Conf. Ser. **456** (2013) 012018.

[79] J. Jobst and H. B. Weber: Nat. Phys. **8** (2012) 352.

[80] J.-H. Chen, L. Li, W. G. Cullen, E. D. Williams, and M. S. Fuhrer: Nat. Phys. **8** (2012) 353.

[81] B. A. Jones and C. M. Varma: Phys. Rev. Lett. **58** (1987) 843.

[82] O. Sakai and Y. Shimizu: J. Phys. Soc. Jpn. **61** (1992) 2333.

[83] I. Affleck, A. W. W. Ludwig, and B. A. Jones: Phys. Rev. B **52** (1995) 9528.

[84] R. Bulla, T. Pruschke, and A. C. Hewson: J. Phys.: Condens. Matter **9** (1997) 10463.

[85] R. Bulla, T. A. Costi, and T. Pruschke: Rev. Mod. Phys. **80** (2008) 395.

[86] C. Gonzalez-Buxton and K. Ingersent: Phys. Rev. B **57** (1998) 14254.

[87] N. M. R. Peres, F. Guinea, and A. H. Castro Neto: Phys. Rev. B **73** (2006) 125411.

[88] V. M. Pereira, J. M. B. Lopes dos Santos, and A. H. Castro Neto: Phys. Rev. B **77** (2008) 115109.

[89] W. Hofstetter and S. Kehrein: Phys. Rev. B **59** (1999) R12732.

[90] Y. Hatsugai, K. Ishibashi, and Y. Morita: Phys. Rev. Lett. **83** (1999) 2246.

[91] L. Fritz and M. Vojta: Phys. Rev. B **70** (2004) 214427.

[92] N. Tajima, R. Kato, S. Sugawara, Y. Nishio, and K. Kajita: Phys. Rev. B **85** (2012) 033401.

[93] M. Monteverde, M. O. Goerbig, P. Auban-Senzier, F. Navarin, H. Henck, C. R. Pasquier, C.Mézière, and P. Batail: Phys. Rev. B **87** (2013) 245110.

[94] T. Kawarabayashi, Y. Hatsugai, T. Morimoto, and H. Aoki: Phys. Rev. B **83** (2011) 153414.

[95] A. Kobayashi, S. Komaba, S. Katayama, and Y. Suzumura: J. Phys.: Conf. Ser. **132** (2008) 012002.

[96] Y. Hasegawa and K. Kishigi: J. Phys. Soc. Jpn. **80** (2011) 054707.

[97] H. Kino and T. Miyazaki: J. Phys. Soc. Jpn. **78** (2009) 105001.

[98] T. Kariyado and M. Ogata: J. Phys. Soc. Jpn. **79** (2010) 083704.

[99] E. N. Economou: *Green's Functions in Quantum Physics* (Springer, Berlin, 2006) 3rd ed.

[100] S. Katayama, A. Kobayashi, and Y. Suzumura: Eur. Phys. J. B **67** (2009) 139.

[101] K. Ishida, Y. Kitaoka, T. Yoshitomi, N. Ogata, T. Kamino, and K. Asayama: Physica C **179** (1991) 29.

[102] Y. Takano, K. Hiraki, H. M. Yamamoto, T. Nakamura, and T. Takahashi: Synth. Met. **120** (2001) 1081.

[103] T. Kakiuchi, Y. Wakabayashi, H. Sawa, T. Takahashi, and T. Nakamura: J. Phys. Soc. Jpn. **76** (2007) 113702.

[104] H. Seo, C. Hotta, and H. Fukuyama: Chem. Rev. **104** (2004) 5005.

[105] H. Seo, J. Merino, H. Yoshioka, and M. Ogata: J. Phys. Soc. Jpn **75** (2006) 051009.

[106] H. Seo: J. Phys. Soc. Jpn. **69** (2000) 805.

[107] B. Rothaemel, L. Forró, J. R. Cooper, J. S. Schilling, M. Weger, P. Bele, H. Brunner, D. Schweitzer, and H. J. Keller: Phys. Rev. B **34** (1986) 704.

[108] Y. Tanaka: Abstr. Meet. Physical Society of Japan (68th Annu. Meet. 2013), Part 4, p. 929, 27aXN-13 [in Japanese].

[109] Y. Tanaka: Abstr. Meet. Physical Society of Japan (Autumn Meet. 2013), Part 4, p. 743, 25pDJ-6 [in Japanese].

[110] N. A. Fortune, K. Murata, M. Ishibashi, M. Tokumoto, N. Kinoshita, and H. Anzai: Solid State Commun. **77** (1991) 265.

[111] Y. Tanaka and K. Yonemitsu: J. Phys. Soc. Jpn. **77** (2008) 034708.

[112] H. Isobe and N. Nagaosa: J. Phys. Soc. Jpn. **81** (2012) 113704.

[113] N. Goldenfeld: *Lectures on Phase Transitions and the Renormalization Group* (Westview Press, Boulder, 1992).

[114] J. Cardy: *Scaling and Renormalization in Statistical Physics* (Cambridge University Press, Cambridge, 1996).

[115] J. A. Hertz: Phys. Rev. B **14** (1976) 1165.

[116] A. J. Millis: Phys. Rev. B **48** (1993) 7183.

[117] T. Moriya: *Spin Fluctuations in Itinerant Electron Magnetism* (Springer-Verlag, Berlin, 1985).

[118] T. Moriya and K. Ueda: Adv. Phys. **49** (2000) 555.

[119] S. Watanabe and K. Miyake: Phys. Rev. Lett. **105** (2010) 186403.

[120] M. Dressel: J. Phys.: Condens. Matter **23** (2011) 293201.

[121] J. Merino, H. Seo, and M. Ogata: Phys. Rev. B **71** (2005) 125111.

[122] H. Watanabe and M. Ogata: J. Phys. Soc. Jpn. **75** (2006) 063702.

[123] J. Merino and R. H. McKenzie: Phys. Rev. Lett. **87** (2001) 237002.

[124] Y. Tanaka, Y. Yanase, and M. Ogata: J. Phys. Soc. Jpn. **73** (2004) 2053.

[125] J. Merino, A. Greco, N. Drichko, and M. Dressel: Phys. Rev. Lett. **96** (2006) 216402.

[126] L. Cano-Cortés, J. Merino, and S. Fratini: Phys. Rev. Lett. **105** (2010) 036405.

[127] K. Yoshimi, T. Kato, and H. Maebashi: J. Phys. Soc. Jpn. **78** (2009) 104002.

[128] K. Yoshimi, T. Kato, and H. Maebashi: J. Phys. Soc. Jpn. **80** (2011) 123707.

[129] K. Yoshimi and H. Maebashi: J. Phys. Soc. Jpn. **81** (2012) 063003.

[130] I. F. Herbut: Phys. Rev. Lett. **97** (2006) 146401.

[131] Y. Araki and G. W. Semenoff: Phys. Rev. B **86** (2012) 121402.

[132] N. Nagaosa: *Quantum Field Theory in Strongly Correlated Electronic Systems* (Springer-Verlag, Berlin, 1999).

[133] A. Altland and B. Simons: *Condensed Matter Field Theory* (Cambridge University Press, Cambridge, 2010) 2nd ed.

[134] K. W.-K. Shung: Phys. Rev. B **34** (1986) 979.

[135] A. L. Fetter and J. D. Walecka: *Quantum Theory of Many-Particle Systems* (Dover Publications, New York, 2003).

[136] K. Miyake and O. Narikiyo: J. Phys. Soc. Jpn. **71** (2002) 867.

[137] A. Ishigaki and T. Moriya: J. Phys. Soc. Jpn. **68** (1999) 3673.

[138] Y. Yanase and K. Yamada: J. Phys. Soc. Jpn. **68** (1999) 2999.

[139] Y. Yanase, T. Jujo, T. Nomura, H. Ikeda, T. Hotta, and K. Yamada: Phys. Rep. **387** (2003) 1.

[140] K. Ingersent, A. W. W. Ludwig, and I. Affleck: Phys. Rev. Lett. **95** (2005) 257204.

[141] H. Amara, S. Latil, V. Meunier, P. Lambin, and J.-C. Charlier: Phys. Rev. B **76** (2007) 115423.

[142] T. Hotta: Phys. Rev. Lett. **96** (2006) 197201.

[143] T. Hotta: J. Phys. Soc. Jpn. **76** (2007) 084702.